Development and Optimisation of Efficient Spray-Coated Perovskite Solar Cells

James Edward Bishop

Department of Physics and Astronomy

The University of Sheffield

The University Of Sheffield.

Thesis submitted for the degree of Doctor of Philosophy
(Alternative Format)

July 2019

Acknowledgements

I've been lucky to have pursued my PhD in a very supportive environment. I am very grateful that my supervisor David Lidzey gave me the opportunity to do a PhD and the guidance to see it to completion. I will always appreciate his assistance in writing papers, which has always led to an improvement in the clarity of writing. Working within the EPMM group has been a great experience due to the friendly and collaborative nature of all its members. I've made several close friends through this group and that is something I will always cherish.

I'd like to acknowledge David Mohamad, Michael Wong-Stringer, Tom Routledge, Joel Smith, and Onkar Game without whose support I doubt I would have been able to publish my work. Their assistance in the lab has been invaluable.

I'd like to thank all my friends in Sheffield for making living here such a joy, but I want to give a special mention to my best friend Tom, without whom it just wouldn't be the same.

Finally, I want to thank my parents and my sisters Grace and Victoria. I couldn't ask for a more supportive and loving family. I particularly appreciate my dad's advice to "finish your PhD." Well dad, it's taken me longer than you but I finally completed it.

Note on Alternative Format

This thesis is submitted in an alternative format with the approval of the University of Sheffield Research Services.

Chapters 3, 5 and 6 of this thesis are comprised of published papers which have already been independently peer reviewed. To preserve continuity within this thesis these papers have been typeset in word although their contents are unaltered. The DOI of these papers is provided should the reader wish to view the published version of the work. Chapter 7 presents work which has not yet been published but is intended for submission and as such is presented in the format of a scientific paper. Brief sections before and after these chapters are provided to give further context to the work and improve continuity between chapters.

This thesis is comprised of published papers and work intended for publication that have a number of collaborating authors. In each case the experimental work, analysis of the data, and writing of the manuscript was primarily completed by the author (James E. Bishop), and the co-authors listed below have been contacted and agree to this.

Dr David K. Mohamad
Dr Michael Wong-Stringer
Alex Smith
Prof David G. Lidzey
Dr Thomas J. Routledge
Joel A. Smith
Claire Greenland
Dr Vikas Kumar
Dr Naoum Vaenas
Dr Onkar S. Game
Dr Cornelia Rodenburg

Abstract

In recent years lead halide perovskites have emerged as a promising photovoltaic material with over 20% power conversion efficiency (PCE) demonstrated. Typically, these devices are fabricated on small areas (less than 1 cm^2) utilising spin coating, a technique which is not industrially compatible. Here we demonstrate techniques that can produce efficient perovskite solar cells (PSCs) utilising ultrasonic spray-coating. Spray-coating is a method widely used in industry for coating large areas at speed.

A method to sequentially deposit all solution processed layers in a normal architecture PSC is developed. Here compact-TiO_2, mesoporous-TiO_2, $CH_3NH_3PbI_{(3-x)}Cl_x$ perovskite and doped spiro-OMeTAD layers are deposited in ambient conditions utilising an ultrasonic spray-coater, achieving a peak PCE of 10.2% on small area devices. The average PCE of the spray-cast devices (9.2%) compares favourably with spin coated references (11.4%). This process is then applied to larger substrates to create a 6.6% efficient device with an active-area of 1.5 cm^2. This PCE value was independently verified at the Centre for Renewable Energy Systems Technology (CREST).

Higher efficiency spray-cast PSCs are fabricated by utilising a glovebox mounted spray-coater and vacuum assisted solution processing (VASP). In addition, a higher performance "triple-cation" perovskite formulation with the composition $Cs_{0.05}FA_{0.81}MA_{0.14}PbI_{2.55}Br_{0.45}$ is utilised. By exposing the wet precursor film to a low vacuum immediately after deposition the solvent is rapidly extracted from the film enhancing nucleation. This results in smoother and more uniform perovskite layers compared to films that are simply annealed after spray-deposition. When incorporated into a PSC these VASP treated thin films enable devices with a peak PCE of 17.8%.

This vacuum assisted spray method is then combined with ambient ultrasonic spray-coating of tin oxide nanoparticles and spiro-OMeTAD. The use of spray-deposition allows the rapid coating of 25 x 75 mm substrates which can then be utilised to form a series of 15.4 mm^2 PSCs with an average PCE of 12.2% and a peak efficiency of 15.1%. This demonstrates the flexibility of spray-deposition and is an important proof of concept for potential industrial development of spray-coated PSCs.

Publications

As Chapter (3)

1. **James E. Bishop,** Thomas J. Routledge, David G. Lidzey, *Advances in Spray-Cast Perovskite Solar Cells*, Journal of Physical Chemical Letters, **2018**, 9, 8, 1977 DOI: 10.1021/acs.jpclett.8b00311

As Chapter (5)

2. **James E. Bishop,** David K. Mohamad, Michael Wong-Stringer, Alex Smith, David G. Lidzey, *Spray-cast multilayer perovskite solar cells with an active-area of 1.5 cm²*, Scientific reports, **2017**, 7, 1, 7962 DOI: 10.1038/s41598-017-08642-2

As Chapter (6)

3. **James E. Bishop**, Joel A. Smith, Claire Greenland, Vikas Kumar, Naoum Vaenas, Onkar S. Game, Thomas J. Routledge, Michael Wong-Stringer, Cornelia Rodenburg, and David G. Lidzey, *High Efficiency Spray-Coated Perovskite Solar Cells Utilising Vacuum Assisted Solution Processing*, ACS Applied Materials and Interfaces, **2018**, *10*, 46, 39428 DOI: 10.1021/acsami.8b14859

As Chapter (7)

4. **James E. Bishop**, Joel A. Smith, Thomas J. Routledge, David G. Lidzey, *Fully Spray-Coated Perovskite Solar Cells*, preparing to submit.

5. Michael Wong-Stringer, **James E. Bishop**, Joel A. Smith, David K. Mohamad, Andrew J. Parnell, Vikas Kumar, Cornelia Rodenburg and David G. Lidzey, *Efficient perovskite photovoltaic devices using chemically doped PCDTBT as a hole-transport material*, J. Mater. Chem. A, **2017**, 5, 30, 15714 DOI: 10.1039/c7ta03103c

6. Mejd Alsari, Oier Bikondoa, **James E. Bishop**, Mojtaba Abdi-Jalebi, Lutfiye Y Ozer, Mark Hampton, Paul Thompson, Maximilian T. Horantner, Suhas Mahesh, Claire Greenland, J Emyr Macdonald, Giovanni Palmisano, Henry J. Snaith, David G. Lidzey, Samuel D. Stranks, Richard H. Friend, Samuele Lilliu, *In situ simultaneous photovoltaic and structural evolution of perovskite solar cells during film formation*, Energy and Environmental Science, **2018**, 11, 2, 382 DOI: 10.1039/c7ee03013d

7. Thomas J. Routledge**,** Michael Wong-Stringer, Onkar S. Game, Joel A. Smith, **James E. Bishop**, Naoum Vaenas, Benjamin G. Freestone, David M. Coles, Trevor McArdle, Alastair R. Buckley, and David G. Lidzey, *Low-temperature, high-speed reactive deposition of metal oxides for perovskite solar cells*, Journal of Materials Chemistry A, **2019**, 7, 5, 2283, DOI: 10.1039/c8ta10827g

8. Michael Wong-Stringer, Thomas J. Routledge**,** Trevor McArdle, Christopher Wood, Onkar S. Game, Joel A. Smith, **James E. Bishop**, Naoum Vaenas, David M. Coles, Alastair R. Buckley, and David G. Lidzey, *A flexible back-contact perovskite solar micro-module,* Energy and Environmental Science, **2019**, 12, 1928 DOI: 10.1039/c8ee03517b

Conference Presentations

Oral presentation

James E. Bishop, Michael Wong-Stringer, Alex Smith, David G. Lidzey, *Spray-cast multilayer perovskite solar cells with an active-area of 1.5 cm²*, Centre for Doctoral Training - Photovoltaic (CDT-PV) Showcase University of Liverpool, **November 2016**

Oral presentation

James E. Bishop, Michael Wong-Stringer, Alex Smith, David G. Lidzey, *Spray-cast multilayer perovskite solar cells with an active-area of 1.5 cm²*, Photovoltaics Science Applications and Technology Bangor (PV-SAT 13), **April 2017**

Poster presentation

James E. Bishop, Michael Wong-Stringer, Alex Smith, David G. Lidzey, *Spray-cast multilayer perovskite solar cells with an active-area of 1.5 cm²,* Innovations in large area electronics (innoLAE) Cambridge, **February 2017**

Table of Contents

Chapter 1

Introduction

In October 2018 the Intergovernmental Panel on Climate Change (IPCC) published a seminal report on the effects of global warming of 1.5 °C above preindustrial levels.[1] The findings were sobering. If humanity does not act quickly to reduce emissions of greenhouse gases, particularly carbon dioxide (CO_2) released through the burning of fossil fuels, we face devastating consequences. The report predicts high risk of habitat losses, coastal flooding, and disruption of food supplies. Currently we are on track to reach 1.5 °C of warming by 2040 and only a concerted global effort to reduce CO_2 emissions to net zero by 2055 at the latest will give humanity a fighting chance of averting disaster. At the time of writing it is unclear if the political will exists to effectively rise to this challenge.

Approximately 65% of global electricity production in 2016 came from fossil fuels (coal, oil and natural gas).[2] Reducing our dependence on these energy sources by moving to renewable ones such as wind and solar will enable a sizable reduction in carbon emissions. Solar power is an incredibly promising source of energy. Every day the sun delivers more energy to Earth than humanity uses in a year.[3] In fact many energy sources can be traced back to energy delivered through solar irradiance. Sunlight represents an abundant and near limitless supply of energy that is capable of matching the world's growing demand for electricity. Solar panels rely on the photovoltaic effect where light incident upon certain materials induces electrical current and voltage. This was first observed in 1839 by Edmond Becquerel but it took over one hundred years for the first generation of solar cells based upon silicon to be developed at Bell Laboratories in 1954.[4] It is this technology that has become the market leader for commercial solar panels.[5]

Since then a variety of other materials have been explored for photovoltaic (PV) applications with the general aim to develop solar cells that are efficient, cheap to produce, and stable under operational conditions. The power conversion efficiency (PCE) of a PV device is a measure of the percentage of light incident upon it that is

converted into usable electricity. In order to directly compare between different devices, laboratories testing solar cells do so under a standardised light intensity and spectrum. The National Renewable Energy Laboratory (NREL) in Boulder Colorado produces a chart that tracks the efficiency of all photovoltaic technologies against time.[6]

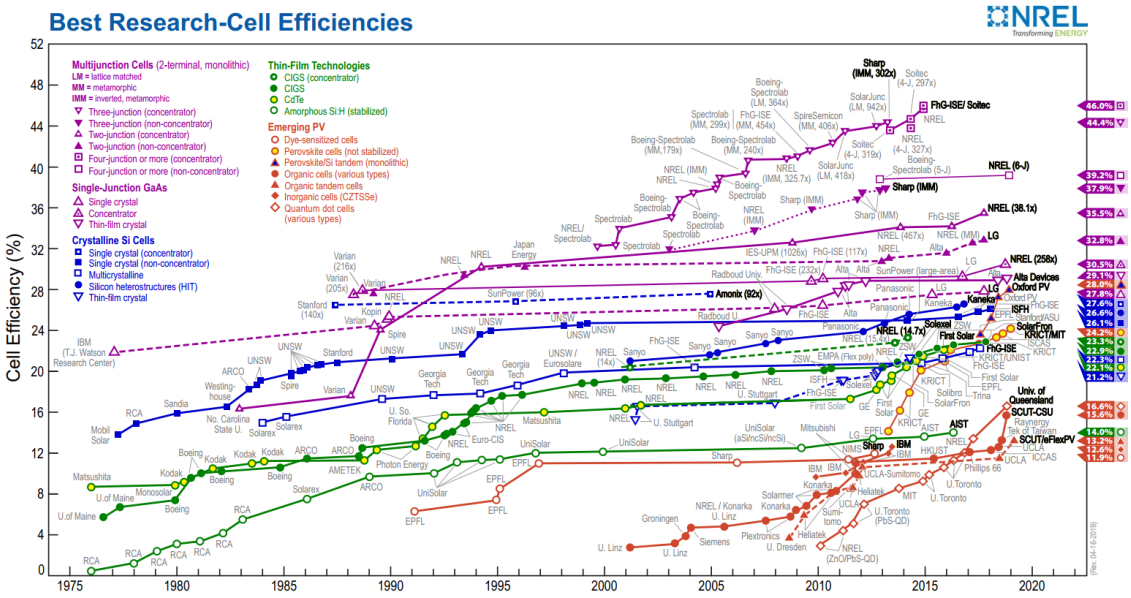

***Figure 1**: NREL best research-cell efficiency chart.*

Silicon based photovoltaics have steadily increased in efficiency to a peak of just over 26% since the 1970s and you can purchase commercial panels that are rated 20% efficient for 25 years. Ironically silicon is actually not a particularly good light absorber and thus devices based upon silicon have to be relatively thick in order to absorb sufficient light to operate at high PCE (hundreds of microns).[7] As a result of this a variety of thin film technologies have been developed based upon semiconductors with higher absorption coefficients such as Cadmium Telluride.[4] So called "second generation" thin film photovoltaics have the potential to reduce the cost of fabricating solar panels dramatically through a reduction in material usage and simpler fabrication techniques.

Silicon wafers for solar applications have to been grown at high temperatures to reach the purity required for high performance.[7] Not only did this initially make silicon solar cells expensive, it also caused them to have relatively long energy payback times. The energy payback time of a PV device is defined as the time it will take under operational conditions to generate the same amount of energy that was

used in its manufacture. Obviously this time will vary depending on where the device is deployed, but it is generally accepted that silicon solar cells have an energy payback time in the order of years.[8] Thin film technologies with simpler processing techniques requiring lower temperatures are expected to have shorter energy payback times.

Unfortunately despite decades of research, no thin film technology has managed to displace silicon as the market leading technology. Currently all thin film technologies combined have only a 5% market share.[5] The reason for this has been the remarkable reduction in the cost of silicon modules over recent years from around $70 per Watt in 1979 to well below 50 cents per Watt today.[5,9] The reason for this is that of the economics of scale. In addition to solar applications, high grade silicon is essential in the consumer electronics industry for computer processing units. As this industry has grown over the last three decades, efficiency savings have driven down the cost of producing silicon enormously.[9] As a result of this, Chinese photovoltaic companies have come to dominate the market with further cost reductions expected.[5] This will mean the healthy growth in the solar energy deployment worldwide is likely to continue.

Around the turn of the millennium there was enormous growth in research into organic electronics which utilise polymers and small molecules as semiconductors. Much of the excitement behind these materials was the fact that they could be processed from a solution quickly and cheaply. The hope was to apply the revolution that came with the development of plastics to the field of electronics deploying flexible, lightweight and cheap devices.[10] As such a third generation of photovoltaics emerged in the form of organic solar cells and dye sensitised solar cells (DSCs). Whilst the PCE of these technologies has increased, they are still significantly lower than the 20% benchmark set by silicon solar cells.[6] This is not expected to be a problem for third generation PV as the expected reduction in processing costs and energy payback time could offset a lower PCE. Unfortunately organic materials suffer from intrinsic stability issues that cause them to degrade under operational conditions.[11] Whilst a few companies are currently developing organic solar modules, these have not yet successfully emerged into the commercial market.

In 2009 a Japanese research group reported on a DSC in which the light absorbing dye molecule had been replaced with a material called perovskite.[12] Perovskites are a class of materials with a specific crystal structure ABX_3. Whilst these materials had been investigated for their optoelectronic properties as early as the 1990s, no one had yet thought to utilise them within a photovoltaic device.[13] Whilst the efficiency of these perovskite solar cells (PSCs) was initially low, they rapidly increased, quickly exceeding all other third generation technologies and reaching 20% within 5 years of research.[6] This unprecedented rise in PCE attracted enormous interest from the third generation PV community. Here was a technology that preserved the advantages of third generation photovoltaics (ease of fabrication from solution) whilst dramatically increasing performance to match that of silicon.

Despite the impressive efficiency gains demonstrated by PSCs they did not solve all of the problems faced by many third generation PV technologies. Researchers quickly identified that whilst the some perovskite materials were excellent light absorbing semiconductors, they were also intrinsically unstable, particularly when exposed to ambient conditions.[14–16] Furthermore the best performing perovskite compositions contain lead which raises public health concerns if such materials were widely deployed in PV installations. This issue may be manageable as the quantity of lead in a PSC is small due to the low thickness of the perovskite layer. However for perovskites to transfer out of the lab into a commercially available product, devices with long term stability must be demonstrated.

There is also significant interest in developing industrially compatible deposition techniques capable of fabricating large area PSCs at speed.[17] Roll to roll production has long been the dream of the third generation PV community, where a flexible substrate is fed through the coating system before being rolled up onto a drum for transportation. Such a process would take advantage of the low temperatures required for solution processing of PSCs to fabricate efficient, lightweight, flexible, and cheap solar cells with a short energy payback time.[8]

There are open questions as to whether PSCs will actually be able to succeed in a market dominated by the mature silicon industry. The cost of silicon solar modules is expected to continue to drop to the point where the largest barrier to deploying

the device is not the cost of the device itself, but the electronics required to manage the power it produces (the so called balance of systems).[5,9,18] As a result of this, many researchers see perovskites true potential as forming part of a tandem device with silicon.[19,20] Essentially the two materials are brought together to form a hybrid device that can more efficiently capture solar energy. Such perovskite-silicon tandem devices have already been demonstrated with 28% PCE and may well represent the future of perovskite PV.[6]

1.1: Thesis Motivation

For PSCs to become commercialised researchers must demonstrate that efficient devices can be fabricated using a scalable deposition technique which can easily be adapted to an industrial production line. There are several potentially suitable deposition techniques however this thesis is focused on developing efficient PSCs using spray deposition. This introduces a series of challenges as spraying the solution increases the parameter space for device optimisation. This thesis outlines techniques to increase the performance of spray-cast PSCs, as well as attempts to fabricate "fully-sprayed" devices where all solution processed layers within a PSC are deposited by spray-coating.

1.2: Thesis Overview

Chapter 2 covers the background physics of solar cell operation including the properties of semiconductors. The history of perovskite PV is discussed as well as the optoelectronic properties that make lead halide perovskites so exciting. An overview of solution processing is presented together with a discussion of the formation mechanism of a perovskite thin film. A range of scalable solution processing techniques are illustrated along with their application to PSCs.

Chapter 3 expands upon Chapter 2, detailing the development of spray-coated PSCs. A discussion of the mechanics of the spray deposition process is included which gives further context to the optimisation in Chapters 5-7.

Chapter 4 summaries the techniques used to fabricate and test PSCs in order to give further context to Chapters 5-7. The individual spray-coaters utilised in this thesis

are outlined along with their advantages and disadvantages. Characterisation techniques commonly employed within this thesis such as laser-beam-induced current mapping (LBIC) are discussed.

Chapter 5 discusses the development of a device where all solution processed layers are deposited by spray-coating in ambient conditions. A series of spin and spray-cast devices are made in order to compare performance between the two deposition techniques. Laser-beam-induced current mapping and surface profilometry is used to characterise the morphology of the devices fabricated highlighting the loss in uniformity caused by spray-coating. Finally a large-area device with an active area of 1.5 cm^2 is fabricated using the techniques developed above.

Chapter 6 outlines the development of a new technique to spray-coat perovskite thin films with higher uniformity than those produced in Chapter 5. This is achieved primarily through the use of a vacuum post treatment step to control crystallisation of the perovskite. A glovebox spray-coater is also used in conjunction with a higher performance perovskite formulation. This allows the fabrication of devices which match the current state of the art for a spray-cast PSC. The morphology of the perovskite thin films fabricated with and without vacuum exposure is characterised using a range of techniques, demonstrating the positive effect of vacuum treatment.

Chapter 7 combines the learning from Chapters 5 and 6 to fabricate "fully-sprayed" PSCs with high efficiency. Here the vacuum treated perovskite is combined with charge transport layers deposited by ambient spray-coating. In a manner similar to Chapter 5 the morphology of these layers is compared to spin coated references using LBIC and surface profilometry. Finally this deposition method is used to fabricate larger area devices which maintain high performance.

Chapter 8 summarises the results of the thesis along with challenges that must still be overcome for spray-coated PSCs to transition out of the lab and into the commercial market.

1.3: References

[1] Intergovernmental Panel on Climate Change, *Special Report: Global Warming of 1.5°C*, **2018.**

[2] International Energy Agency, *Key World Energy Statistics*, **2016**.

[3] J. Tsao, N. Lewis, G. Crabtree, *Solar FAQs*, *US Dep. Energy,* **2006**.

[4] A. Shah, P. Torres, R. Tscharner, N. Wyrsch, H. Keppner, *Science.* **1999**, *285*, 692.

[5] Fraunhofer ISE, *Photovoltaics Report*, **2019**.

[6] NREL. Best Research-Cell Efficiencies. https://www.nrel.gov/ pv/assets/images/efficiency-chart-20180716.jpg (accessed June 2019)

[7] J Nelson, *The Physics of Solar Cells*, Imperial College Press, **2003**.

[8] J. Gong, S. B. Darling, F. You, *Energy Environ. Sci.* **2015**, *8*, 1953.

[9] R. . Swanson, *Prog. Photovoltaics* **2006**, *14*, 443.

[10] D. De Leeuw, *Phys. World* **1999**, *12*, 31.

[11] P. Cheng, X. Zhan, *Chem. Soc. Rev.* **2016**, *45*, 2544.

[12] A. Kojima, K. Teshima, Y. Shirai, T. Miyasaka, *J. Am. Chem. Soc.* **2009**, *131*, 6050.

[13] D. B. Mitzi, S. Wang, C. A. Feild, C. A. Chess, A. M. Guloy, *Science.* **1995**, *267*, 1473.

[14] B. Conings, J. Drijkoningen, N. Gauquelin, A. Babayigit, J. D'Haen, L. D'Olieslaeger, A. Ethirajan, J. Verbeeck, J. Manca, E. Mosconi, F. De Angelis, H. G. Boyen, *Adv. Energy Mater.* **2015**, *5*, 1500477.

[15] M. A. Green, A. Ho-baillie, H. J. Snaith, *Nat. Photonics* **2014**, *8*, 506.

[16] H. J. Snaith, *J. Phys. Chem. Lett* **2013**, *4*, 3623.

[17] I. A. Howard, T. Abzieher, I. M. Hossain, H. Eggers, F. Schackmar, S. Ternes, B. S. Richards, U. Lemmer, U. W. Paetzold, *Adv. Mater.* **2019**, *1806702*, 1806702.

[18] Z. Zhou, M. Carbajales-Dale, *Energy Environ. Sci.* **2018**, *11*, 603.

[19] K. A. Bush, A. F. Palmstrom, Z. J. Yu, M. Boccard, R. Cheacharoen, J. P. Mailoa, D. P. McMeekin, R. L. Z. Hoye, C. D. Bailie, T. Leijtens, I. M. Peters, M. C. Minichetti, N. Rolston, R. Prasanna, S. Sofia, D. Harwood, W. Ma, F. Moghadam, H. J. Snaith, T. Buonassisi, Z. C. Holman, S. F. Bent, M. D. McGehee, *Nat. Energy* **2017**, *2*, 17009.

[20] T. Duong, Y. L. Wu, H. Shen, J. Peng, X. Fu, D. Jacobs, E. C. Wang, T. C. Kho, K. C. Fong, M. Stocks,

E. Franklin, A. Blakers, N. Zin, K. McIntosh, W. Li, Y. B. Cheng, T. P. White, K. Weber, K. Catchpole, *Adv. Energy Mater.* **2017**, *7*, 1700228.

Chapter 2

Background Theory

2.1: The Physics of Solar Cells

Solar cells or photovoltaic devices directly convert light into electrical energy via the photovoltaic effect. This phenomenon relies upon the absorption of photons of light by a material to generate electrons and holes which are then spatially separated by an inherent asymmetry built into the device. This induces both an electrical current and potential difference which allows the device to deliver power to an external circuit. This phenomenon is similar to the photoelectric effect where a metal illuminated with light can produce free electrons as long as the energy of incident photons is greater than the work function of the metal in question.[1]

2.1.1: Band Structure of Solids

Modern photovoltaics would not exist without an understanding of the physics of semiconductors, the lynchpin of which is the band theory of solids. As a consequence of quantum mechanics, electrons within atoms exist in orbitals defined by four quantum numbers which satisfy the Schrödinger equation, with each orbital having a well-defined energy. The Pauli Exclusion Principle states that no two electrons can share all four quantum numbers and therefore electrons fill these orbitals from lowest to highest energy. The occupancy and shape of such orbitals in turn determines how atoms interact with one another. Due to the Heisenberg Uncertainty Principle the electron orbitals are described as probability density clouds defined by wave functions rather than particles with a known position and momentum.

When two atoms are brought together to form a molecule the individual atomic orbitals combine to form molecular orbitals. If the wave functions comprising the molecular orbital are in phase then they form a bonding orbital with slightly less energy than the original atomic orbitals. Conversely if the wave functions are out of

phase then an antibonding orbital is formed with energy higher than the energy of the original atomic orbital.[2] In essence by bringing two atoms together to form a molecule, a number of new molecular orbitals are created equal to the original number of atomic orbitals. When a large group of atoms are brought together to form a solid then a large number of new energy levels are formed, so many in fact that they form a continuum of energy states known as a bands.[1] These bands are occupied with electrons from lowest to highest energy with the highest occupied band known as the valence band. Conversely the lowest unoccupied band is known as the conduction band.

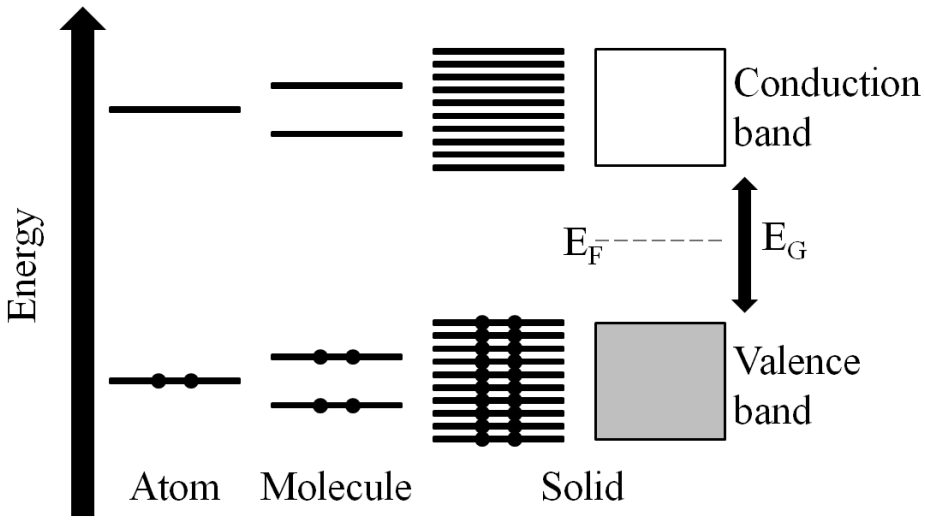

***Figure 1**: Formation of bands in a semiconductor. As multiple atoms are brought together in solid their energy levels split eventually forming continuums of energy states known as bands.*

The occupation of bands and their resultant structure is dependent on the orbitals that form them and is of key importance when understanding the behaviour of solid materials. If the valence band is partially full or it overlaps in energy with another empty band, then the solid is a metal. Electrons are easily able to be excited to other states and these electrons are essentially free to conduct heat or electricity. If the valence band is filled and separated by an energy gap, known as the band gap (E_G) from the conduction band, the material is said to be either an insulator or a semiconductor. Here it is difficult for electrons to be excited to unoccupied states due to the band gap and the material has a significantly lower conductivity than that of a metal.

Here it is important to note the concept of the Fermi level (E_F) of a solid. The occupancy of the energy levels within a band follows the Fermi-Dirac distribution function

$$f(E) = \frac{1}{\exp\left(\frac{(E - E_F)}{k_B T}\right) + 1} \quad (1)$$

where E is the energy of the state, k_B is the Boltzmann constant and T is the temperature.[3] The Fermi Level is defined as the energy level at thermodynamic equilibrium where the chance of the state being occupied is 50%. This is sometimes referred to as the chemical potential of the solid. In a metal, the Fermi level lies within a band, whereas within a semiconductor/insulator the Fermi level lies within the band gap.

Theoretical solid state physics can describe the formation of bands by solving the Schrödinger equation for a periodic potential through the use of Bloch functions.[3] This allows for the creation of detailed band diagrams plotted in terms of electron energy and crystal momentum (k vector). The point where the gap between the conduction band minima and valence band maxima is smallest is known as the band gap. If this gap is aligned in k space then the semiconductor is said to have a direct band gap, whereas if the gap is offset in k space then the semiconductor is has an indirect band gap (see Figure 2a).

The size of the band gap determines the value of the conductivity of the solid. The smaller the band gap the easier it is for electrons to be excited into the conduction band, and the higher the material's conductivity. Solids with a band gap between 0.5 to 3 eV are classed as semiconductors whereas solids with a band gap >3 eV are classed as insulators. Due to their narrower band gaps, electrons in semiconductors can be excited into the conduction band through absorption of photons of visible light. As long as the photon has energy greater than the band gap, there is a probability that an electron in the valence band will be absorbed and excited into the conduction band leaving an electron vacancy (hole) in the valence band. The probability of this occurring is much higher in direct band gap semiconductors as there is no need for a transfer of crystal momentum via phonon interaction. Electrons in the conduction band with energy higher than the conduction band

minima will undergo a process over time-scales of fs called thermalisation, where they lose energy via thermal interactions down to the band edge (see Figure 2b). It is then possible for the electron and hole to recombine emitting a photon with energy equal to the band gap. Fortunately this process occurs over much longer timescales than thermalisation (microseconds) which allows for the excited electron to be extracted by a photovoltaic device to an external circuit to provide electrical power.[1]

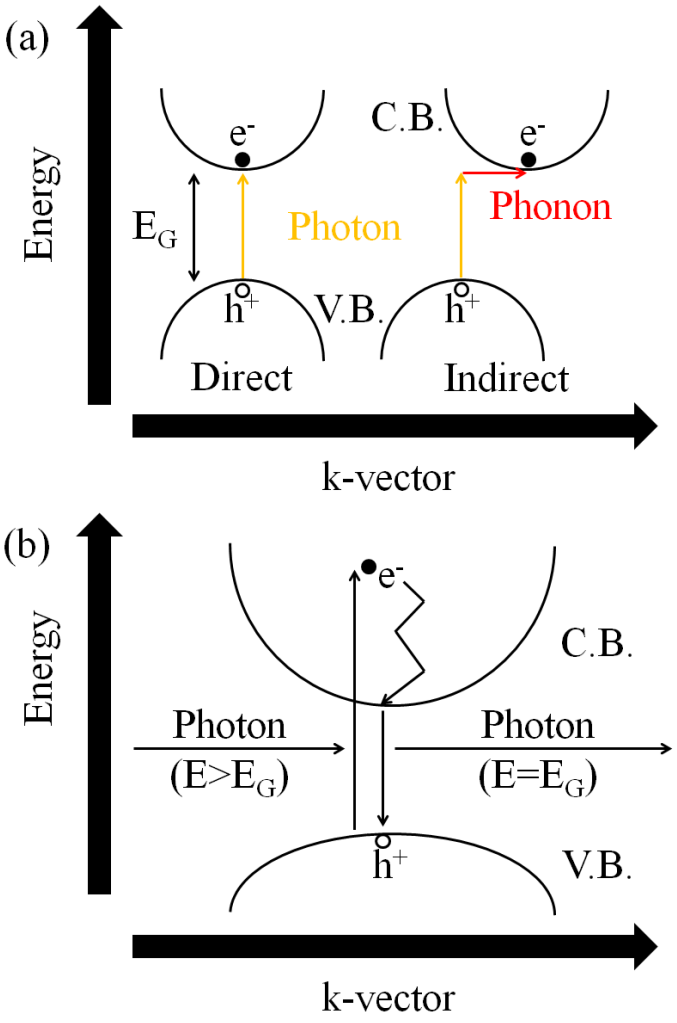

***Figure 2**: (a) Absorption of a photon in a direct and indirect band gap semiconductor. (b) Thermalisation in a direct band gap semiconductor. As the incident photon has greater energy than the band gap, the electron is excited into a free state in the conduction band. The electron then rapidly losses energy through thermalisation to the conduction band minima. Eventually the electron can recombine with the hole in the valence band emitting a photon with energy equal to the band gap.*

2.1.2: P-N Junctions

The conductivity of semiconductors can be enhanced by adding impurities to the semiconductor crystal. By adding a dopant with one more valence electron than the bulk (donor) then this electron must occupy a state in the conduction band as all valence band states must, by the nature of a semiconductor, already be filled. Essentially this electron acts as a free electron enhancing conductivity and the semiconductor is said to be n-type on account of the increased quantity of negative charge. Conversely p-type semiconductors are created by adding a dopant (acceptor) with one less electron than the bulk, creating holes in the valance band. Due to the changing number of carriers in doped semiconductors the Fermi level shifts up for n-type, and down for p-type semiconductors.

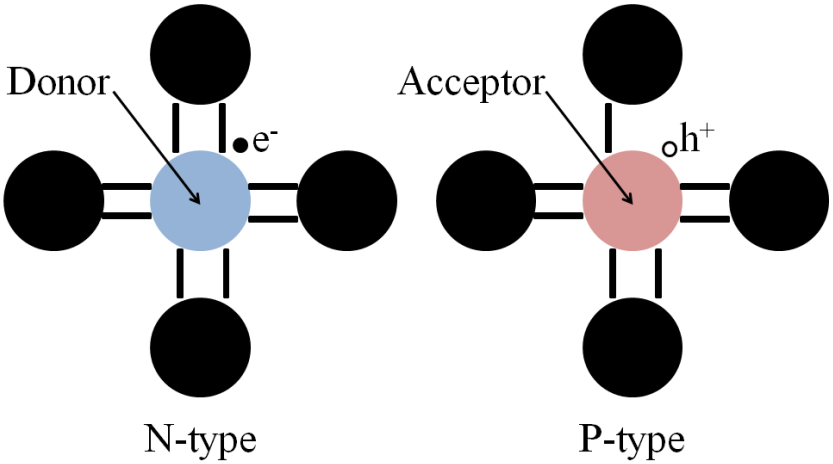

***Figure 3**: Diagram showing the effect of adding dopant atoms to a semiconductor crystal. If the dopant atom has one more valence electron than the bulk semiconductor (donor) then that electron will act as a free charge carrier. Conversely if the dopant has one less electron than the bulk then an electron vacancy or hole is formed that can move around the crystal freely.*

When n-type and p-type semiconductors are brought into contact the excess carriers diffuse across the interface before recombining. This creates a depletion region in the area between the two semiconductors where no free carriers exist. As the now ionised dopant atoms are held in place within the crystal structure, an electric field forms between the positively charged donors and negatively charged acceptors. This creates a built in electric field at the interface which causes the bands of the semiconductors to bend and the Fermi levels to equalise. The built in field now

acts to drive minority carriers across the junction which is known as the drift current. At equilibrium this drift current is balanced by diffusion current of majority carriers with sufficient thermal energy to cross the built in electric field.

A p-n junction can act as a simple model for the operation of a solar cell. If the junction is illuminated with visible light minority carriers are generated in both n and p-type regions. These carriers can then drift across the depletion region to become majority carriers. For example an electron generated in the p-type region can drift across into the n-type region. The effect of this increase in majority carrier density is to split the Fermi levels across the junction placing it into forward bias which in turn reduces the built in field (V_{bi}). This splitting of the Fermi levels accounts for the photovoltage developed by a solar cell and is limited by the band gap. By extracting excited carriers, a photocurrent is provided to the external circuit. There will always be some degree of recombination before charge carriers can be extracted by the device and this will act to limit performance.

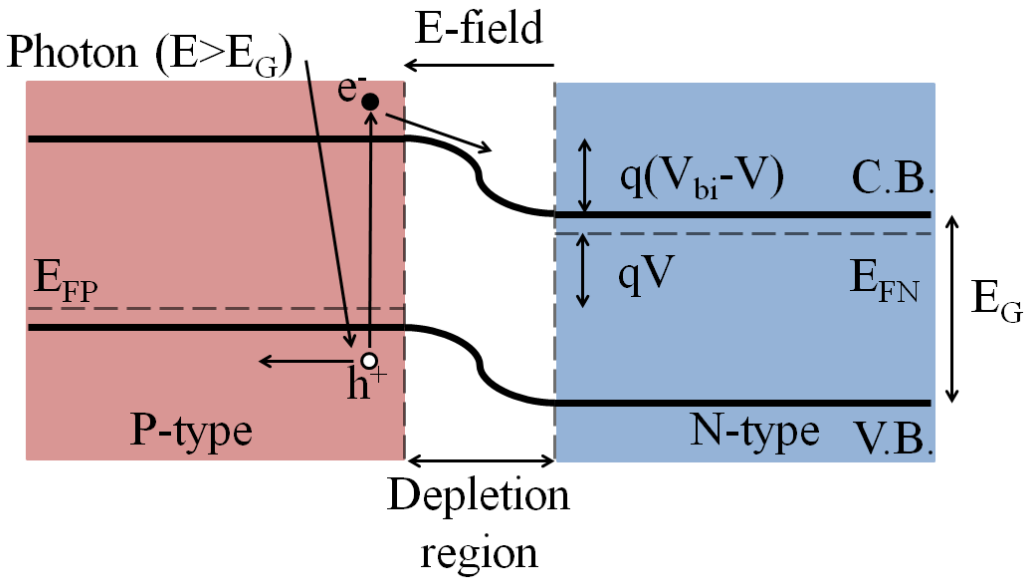

***Figure 4**: Illustration of a p-n junction under illumination. Photons with energy greater than the band gap are absorbed generating electrons in the conduction band and holes in the valence band. These charges are separated by the built in potential of the junction and can be extracted to provide electrical power to an external circuit.*

2.1.3: The Equivalent Circuit

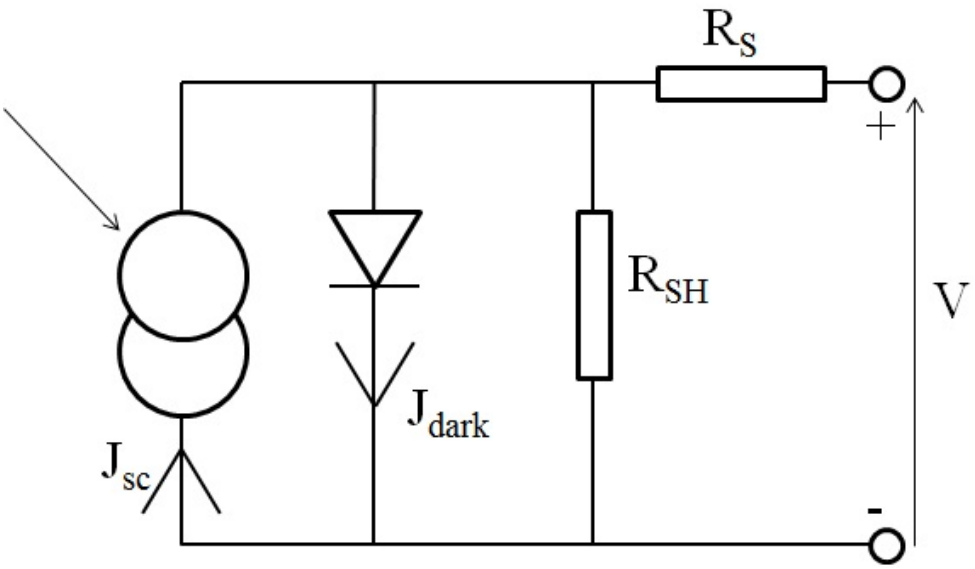

Figure 5*: The equivalent circuit model for a solar cell.*

The current and voltage characteristics of a p-n junction are those of a diode as the built in field acts to prevent the flow of current across the junction without an applied voltage. As a result we can model a solar cell as a diode in parallel with a current generating element.[1] This photocurrent density (J_{SC}) is divided between the diode (J_{dark}) and the external circuit the device is powering (often referred to as the load). The more resistive the load the more current flows through the diode resulting in a larger potential difference between the terminals. Conversely the less resistive the load the more current flows through the external circuit at the cost of voltage. As the power delivered to the external circuit is the product of the current and the voltage maximising the efficiency of the cell requires careful management of the resistive load across the terminals.

There are also parasitic losses within the device that reduce performance. The first is the series resistance (R_S) which accounts for the intrinsic resistance of the materials within the cell that reduce current. The shunt resistance (R_{SH}) is caused by current leakage through the device as a consequence of a poor rectification across the junction. The following equation allows us to model the current voltage characteristics of a solar cell

$$J = J_{SC} - J_0\left(exp\frac{q(V + JAR_s)}{nk_BT} - 1\right) - \frac{V + JAR_S}{R_{SH}} \qquad (2)$$

where J is the current density provided by the cell, J_0 is a constant, V is the voltage across the device, q is the elementary charge, and A is the area of the cell. For an ideal diode the factor n is 1 which corresponds to no charge recombination across the junction. For a real device this value will be between 1 and 2.[1] In order to maximise the current delivered to the external circuit parasitic losses must be minimised. Ideally this means a series resistance of zero and a shunt resistance of infinity.

2.1.4: Testing Solar Cells

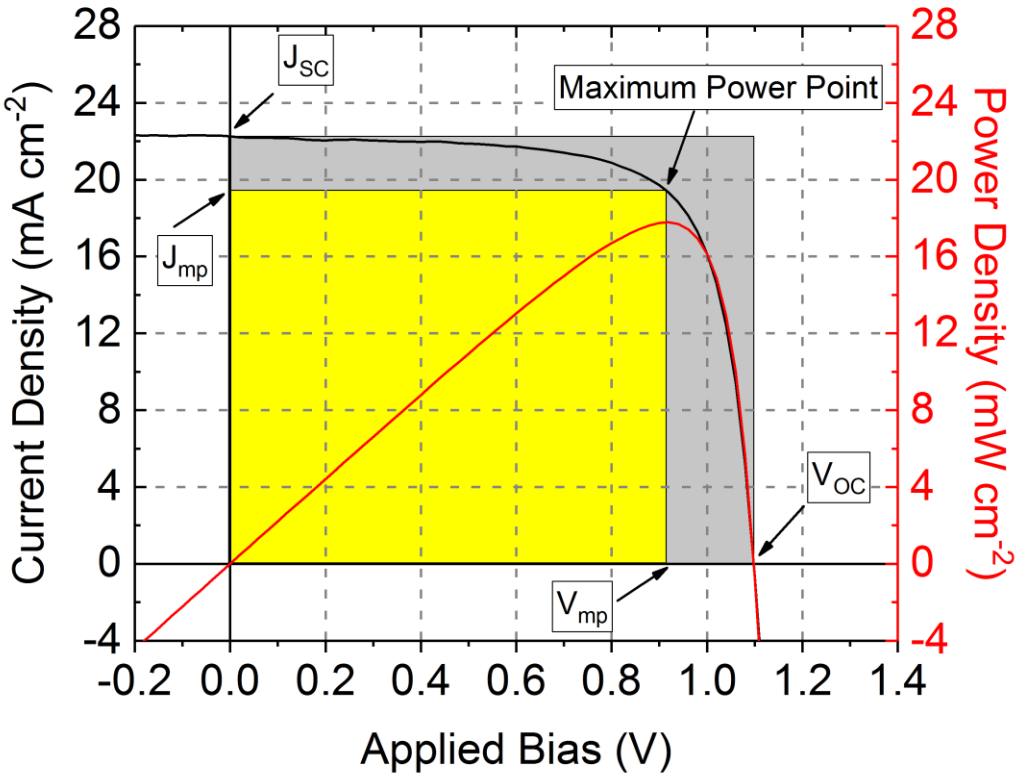

***Figure 6**: Current Voltage characteristics of a solar cell.*

Solar irradiance across the globe varies due to time of year, atmospheric conditions, and the position of the sun in the sky. In order to standardise the testing of solar cells, devices are illuminated with Air Mass 1.5 (AM 1.5) spectrum which corresponds to the sun at a zenith angle of 48.2° at an intensity of 1000 W m^{-2}.[1] By varying the voltage across the device whilst measuring the current produced, the performance can be extracted. Common practice is to report current density in order to compare between devices of separate absolute size.

The black line in Figure 6 shows the current density of a solar cell measured under AM 1.5 illumination, which shows the standard diode response predicted by equation 2. At zero applied bias the device is said to be at short circuit and produces its maximum current. This is known as the short circuit current or photocurrent (J_{SC}). The current produced by the device decreases until it reaches zero at the open circuit voltage (V_{OC}), so called because it corresponds to the device under illumination but without the cell being connected to an external circuit.

By multiplying the current and the voltage at each point together the output power of the device can be calculated. The red line in Figure 6 shows the power density for the solar cell. Here it is clear that the power increases to a peak known as the maximum power point. From this the power conversion efficiency (η) of the device can be easily calculated using the following equation

$$\eta = \frac{J_{mp}V_{mp}}{P_s} \tag{3}$$

where P_s is the incoming power density of light (1000 W m^{-2}), and J_{mp} and V_{mp} are the current and voltage values at the maximum power point. Furthermore the maximum power point can related to the J_{SC} and V_{OC} by a quantity called the fill factor (FF).

$$FF = \frac{J_{mp}V_{mp}}{J_{SC}V_{OC}} \tag{4}$$

The fill factor quantifies the "squareness" of the JV curve which is illustrated in Figure 6 as the ratio between the yellow and grey boxes. An ideal device without any parasitic losses would have a fill factor close to 100%. However due to presence of both series and shunt resistance this is not possible in a real device. As the series resistance of a solar cell increases, the gradient of the curve at open circuit will decrease. This in turn will reduce the maximum power point of the device and the fill factor. If the shunt resistance of the device decreases then the gradient of the curve at short circuit will become increasingly negative, again reducing the fill factor. By combining equations 3 and 4 we can create a new expression linking together the four key metrics used to quantify device performance.

$$\eta = \frac{J_{SC} V_{OC} FF}{P_s} \quad (5)$$

Therefore to achieve the highest possible performance we need to optimise devices to maximise short circuit current, open circuit voltage, and fill factor.

Another important measurement for characterising solar cells is the external quantum efficiency (EQE). This simply quantifies the percentage of photons incident on the device converted into usable electrons per unit wavelength. Unlike the internal quantum efficiency which only accounts for the number of absorbed photons converted into usable electrons, the EQE takes into account photons incident on the device that are not absorbed due to parasitic absorption and reflectance by other materials within the device. By combining the EQE and the AM 1.5 spectrum and integrating the resultant electron flux, a theoretical J_{SC} can be calculated which is a useful check for current voltage measurements.

2.1.5: The Shockley-Quiesser Limit

The maximum theoretical efficiency of a single junction solar cell is limited by fundamental physical constraints. This efficiency limit is known as the Shockley-Quiesser limit after the two physicists who initially calculated it in 1961.[1,4,5] There are four fundamental sources of losses that act to reduce the amount of energy a solar cell can convert into usable electricity.

The dominant sources of lost energy are so called spectrum losses. Any photons with energy less than the band gap of the chosen semiconductor will not be absorbed and thus all that flux of solar energy is lost. However if a semiconductor with a smaller band gap is chosen, whilst more photons will be absorbed, any photons with energy greater than the band gap will lose that excess energy via thermalisation to the band edge. Figure 7a shows the AM 1.5 solar spectrum with these loses (42% in total) highlighted for an ideal silicon solar cell with a band gap of 1.1 eV.[6]

There are also fundamental thermodynamic considerations that limit the usable power generated by the cell. Any object above zero Kelvin must radiate energy in the form of blackbody radiation which increases with the temperature of the object.

As a result of this a percentage of the solar flux on the device must be lost as heat. This lost energy will increase the higher the solar cells operating temperature.

Energy is also lost via recombination of excited electrons and holes through spontaneous emission. This process is unavoidable and will increase as the excited carrier population within the semiconductor rises through absorption of visible light. As a result not all absorbed photons will contribute to usable electricity.

Finally as we have already discussed a solar cell cannot simultaneously deliver maximum current and voltage. Instead it will generate maximum power at a point somewhere between J_{SC} and V_{OC} determined by the fill factor. By combining these limiting factor together Shockley and Quiesser were able to determine the best theoretical power conversion efficiency for a given band gap. The results of this are shown in Figure 7b.

A real solar cell will never be able to achieve the Shockley-Quiesser limit due to the assumptions made in its calculation. For example a real solar cell will lose energy via radiative and non-radiative recombination and will not have perfect absorption. However there are ways to exceed the limit, particularly when employing two or more junctions with semiconductors of different band gaps to harvest separate parts of the solar spectrum simultaneously. This is a potential use for perovskite absorbers in tandem with silicon.[7]

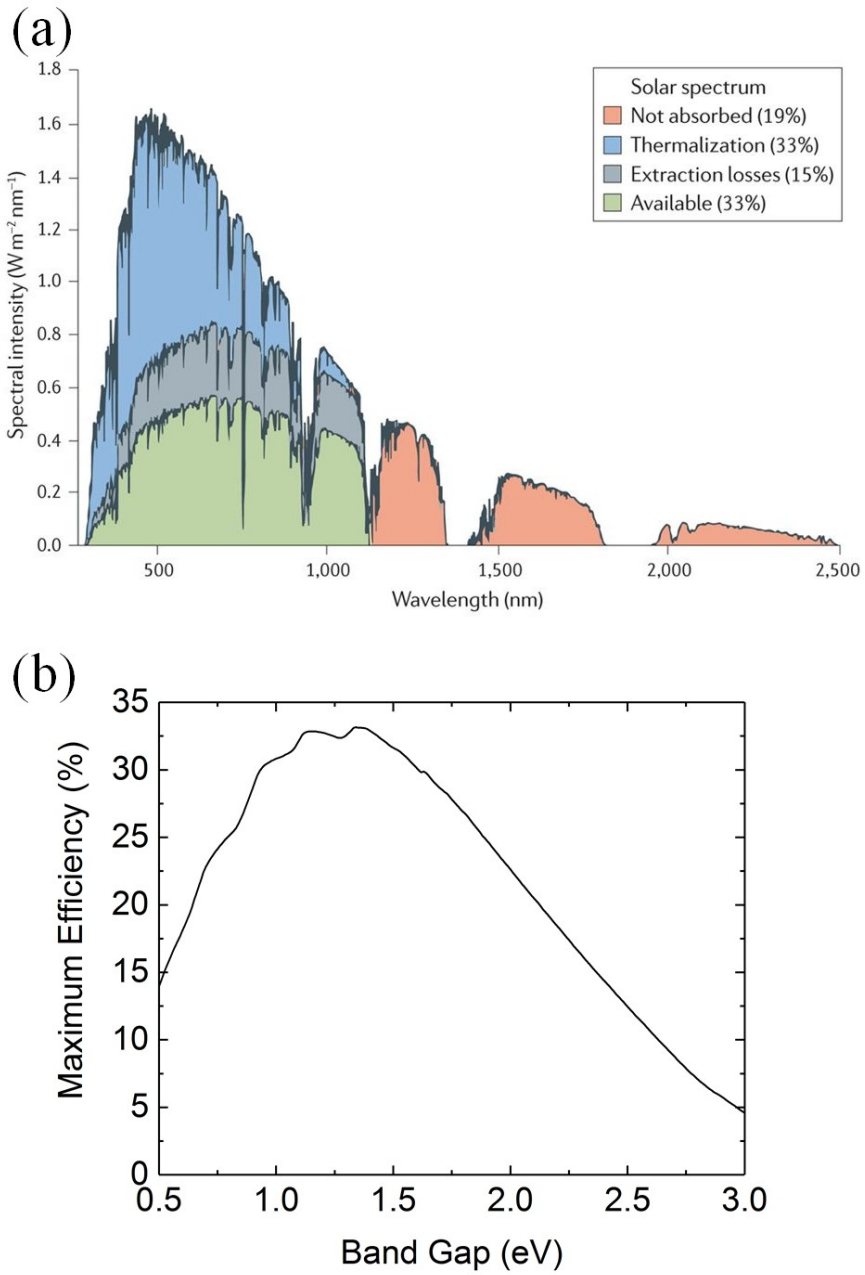

Figure 7*: (a) AM 1.5 solar spectrum with various losses highlighted for an ideal silicon solar cell with a band gap of 1.1 eV. Reproduced from ref. 6 with permission from Nature Publishing Group. (b) Shockley-Quiesser efficiency limit with data taken from ref. 5.*

2.2: The Emergence of Perovskite Solar Cells

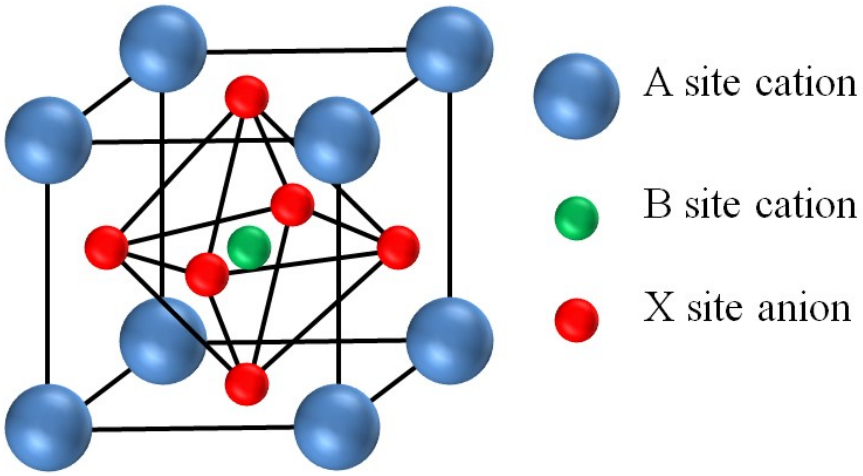

***Figure 8**: Perovskite crystal structure.*

A perovskite is a generic name for any material that forms into an ionic crystal structure ABX_3. A wide range of cations and anions can be incorporated into this structure allowing a large degree of flexibility when designing materials. Perovskites first came into prominence in the field of photovoltaics in 2009 when Kojima *et al.* incorporated a perovskite with the chemical structure $CH_3NH_3PbI_3$ (Methylammonium Lead Triiodide or $MAPbI_3$) into a dye-sensitised solar cell to act as the light absorber.[8]

Dye-sensitised solar cells (DSCs) rely on a mesoporous scaffold of titanium oxide (an n-type transparent conductive oxide) which is infiltrated with a light absorbing dye. This scaffold is then separated from a counter electrode by a separator film and a liquid electrolyte is added to undergo redox with the dye. Kojima *et al.* were able to achieve 3.8% power conversion efficiency using this architecture, although the devices fabricated showed poor stability due to the corrosive action of the electrolyte on the perovskite.

At that time, DSCs were moving towards solid state devices by removing the electrolyte in favour of an organic hole transport material such as spiro-OMeTAD.[9] This was eventually incorporated into a perovskite solar cell (PSC) utilising a mesoporous titanium oxide layer and $MAPbI_3$ with devices reaching 9.7% PCE in 2012.[10] This signified the divergence of perovskite solar cells away from dye-sensitised solar cells and towards an entirely new field of research with ever increasing efficiencies.

2.2.1: Design and Operation of Perovskite Solar Cells

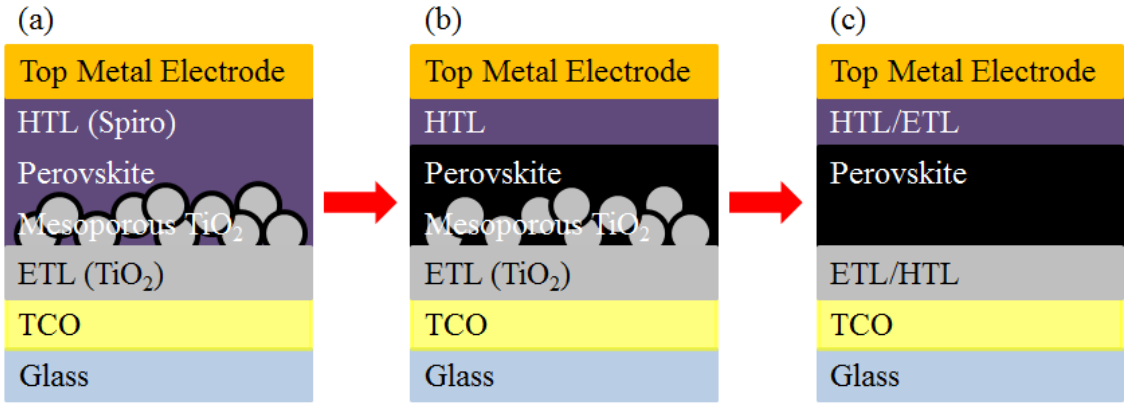

Figure 9: *Evolution of PSC device architecture. (a) Perovskite material replaces the light absorbing dye in a DSC coating the mesoporous TiO_2. (b) Due to its good conductivity the perovskite layer can be thickened to include a capping layer on top of the mesoporous layer. (c) The mesoporous layer is removed to create a planar device with the perovskite sandwiched between hole and electron transport layers.*

When light is absorbed in a semiconductor the resultant electron and hole can be bound together in a quasi-particle known as an exciton. The strength of this attraction is dependent on the degree of coulombic shielding provided by the material; a quantity characterised by the dielectric constant.[3] Dye-sensitised solar cells are said to be excitonic in nature as the dielectric constant of the organic dyes is relatively low. This causes the formation of tightly bound Frenkel excitons that are highly localised within the material. These excitons have a relatively short diffusion length and will recombine if they are not separated by an electric field. As a result of this, dye-sensitised solar cells and organic solar cells require that the photoactive layer of the solar cell contain distributed interfaces to separate the excitons in order to harvest energy. In dye-sensitised solar cells, the solution is to utilise a mesoporous scaffold of titanium oxide coated in with the dye.[11] In organic solar cells the solution is to blend together donor and acceptor molecules in a bulk heterojunction.[12]

Early perovskite devices were based upon the dye-sensitised solar cell device architecture utilising mesoporous titanium dioxide.[8,10] However many soon began to suspect that lead halide perovskites may not actually be excitonic. The first evidence of this was a 2012 report by Lee *et al.* where the n-type titanium oxide

mesoporous scaffold was replaced by insulating mesoporous aluminium oxide with devices reaching 10.9% PCE.[13] Here the alumina was deposited upon a thin (<50 nm) layer of titanium oxide commonly employed in DSCs to block holes from reaching the anode. This result suggested that the charge transfer in a perovskite solar cell was occurring within the perovskite layer itself, not (as was initially expected) the titanium oxide. Another innovation was to move to a mixed halide perovskite of the form $CH_3NH_3PbI_{3-x}Cl_x$ created by mixing Methylammonium Iodide and Lead Chloride in a 3:1 ratio. This material showed similar optical properties to Methylammonium Lead Triiodide but had better stability in ambient conditions.

Building upon this work Stranks *et al.* quantified the electron hole diffusion lengths for $CH_3NH_3PbI_3$ and $CH_3NH_3PbI_{3-x}Cl_x$ perovskite layers reporting 100 nm and >1 μm respectively.[14] The following year D'Innocenzo *et al.* calculated the exciton binding energy of $CH_3NH_3PbI_{3-x}Cl_x$ to be ≈50 meV which is sufficiently low to allow the entire excitonic population too spontaneously dissociate into free carriers at room temperature.[15] By this point a 15% efficient perovskite solar cell had been demonstrated where the mesoporous layer had been removed in favour of simple planar cell architecture.[16] As the field grew, electron and hole transport layers that were utilised in organic photovoltaics (OPVs) were then incorporated into devices in what has been termed the "inverted" PSC architecture.[17]

The exact operational principle of PSCs is still a matter of debate. Charge carriers generated within the perovskite layer spontaneously dissociate due to ionic screening which accounts for the high dielectric constants reported for perovskite solar cells. However unlike a traditional inorganic crystalline silicon solar cell, a perovskite cannot be thought of as a p-n junction. It is well known that PSCs contain a large quantity of mobile ions that can drift to screen electric fields.[18,19] Instead, charges generated within the perovskite layer simply diffuse until they reach a charge selective contact and are extracted by the device. Thus the key to an efficient PSC is to utilise electron and hole transport layers that have energy levels that align well with the quasi Fermi levels within the perovskite layer, whilst at the same time blocking the opposite charge. Chapter 4 contains a brief discussion of the transport layers used in this thesis with their energy level values.

The high power conversion efficiency of PSCs has been attributed to a range of effects including efficient light absorption, high charge carrier mobility, and low non-radiative recombination. Perovskites are predominantly direct band gap semiconductors which accounts for their high absorption coefficient.[20] However there is some evidence that due to the rotation of methylammonium cations, some perovskites can demonstrate a slightly indirect band gap through Rashba Splitting.[20,21] This is anticipated to enhance charge carrier lifetimes by supressing radiative recombination. Values for the carrier mobility of perovskites have been demonstrated to be as high as 17.8 $cm^2V^{-1}s^{-1}$[22,23] with impressive diffusion lengths that can exceed 100 microns in single crystals.[24] Perovskite films are expected to contain a large quantity of vacancy and interstitial defects in the crystal structure.[25] Fortunately many of these defects states reside outside the band gap which prevents them from acting as centres of non-radiative recombination.[26] This accounts for the relatively low voltage losses observed in PSCs with the best devices reporting open circuit voltages only ≈400 mV lower than the band gap.[27,28] These properties allow polycrystalline films that are hundreds of nanometres thick to efficiently absorb photons and transfer charge.

2.2.2: Current Voltage Hysteresis

One of the most unusual properties of PSCs is current voltage hysteresis. Depending of the recent history of the cell, the efficiency measurements can vary. Standard practice when performing current voltage measurements on PSCs is to scan the device from reverse to forward bias and then back to reverse bias. Typically the forward scan will produce a JV curve of lower efficiency than the reverse scan; an effect which can be modulated through changes to the materials used in the cell and the scan rate. PSCs often benefit from a degree of light soaking where the cell is exposed to illumination prior to testing resulting in a higher efficiency.

As a result of hysteresis the best way to quantify the efficiency of a PSC is via maximum power point tracking where software dynamically adjusts the voltage across the cell to achieve the highest output current. This exactly simulates device performance under operating conditions and is thus a reliable way to measure efficiency. Unfortunately many research groups do not have the capacity to perform

maximum power point tracking and instead use a similar measurement where the device is held at a fixed voltage close to the maximum power point. This is known as a stabilised measurement and has become a standard measurement required when reporting on PSC performance.

The exact origin of hysteresis is still an ongoing area of research but the common consensus is that ion migration within the perovskite film is the main cause of hysteresis.[18,19,29,30] Under operation, ions within the perovskite drift under the influence of an applied bias screening the electric field. These ions can build up at the interfaces with electron and hole transport layers and reduce recombination. As the ionic mobility within the perovskite is somewhat lower than electrons and holes, the rate at which the device is tested will affect the degree of screening provided by these ions. The slower the device is scanned the more time these ions are given to "settle" thus reducing the observed hysteresis.

Material selection has an effect on the observed hysteresis; an effect that became apparent when organic selective contacts developed initially for OPV applications were applied to PSCs. Here devices often displayed negligible hysteresis despite utilising the same perovskite layers as those used in "normal" architecture devices with a titanium oxide electron transport layer.[31] The explanation for this behaviour was tied to the efficiency with which the respective layers could extract and transfer electrons and holes. For example titanium oxide does not have as high conductivity as PCBM thus it was anticipated that the unbalanced flux of electrons and holes was, in part, causing the hysteresis in normal architecture devices. This limitation of titanium oxide led researchers to investigate other alternative ETLs with tin oxide emerging as a promising candidate.[32–34] Due to its higher conductivity and better band alignment to perovskite absorbers, devices utilising tin oxide transport layers are capable of displaying minimal hysteresis.

2.2.3: Perovskite Composition and Stability

Despite the excellent photovoltaic performance of PSCs based on $MAPbI_3$, researchers quickly identified that the material was unstable under ambient conditions.[35] Moisture absorption in particular was identified as a key degradation pathway causing the perovskite to break apart into aqueous ammonia and lead

iodide.[36] This degradation is easy to spot as the perovskite film transitions from black to yellow after prolonged exposure to water. Furthermore $MAPbI_3$ is also thermally unstable and will break down at 85 °C even in an inert environment.[37] This would prohibit PSCs based on this material passing standard commercial solar cell stress testing.

As a result of this, researchers began to look towards alternative perovskite compositions with better photovoltaic performance and stability. A promising alternative perovskite was formamidinium lead triiodide ($HC(NH_2)_2PbI_3$ or $FAPbI_3$) which has a slightly narrower band gap than $MAPbI_3$ (1.49 to 1.59 eV).[35,38,39] This allows it to absorb more of the solar spectrum and thus produce a higher photocurrent. Furthermore $FAPbI_3$ had better thermal stability than $MAPbI_3$, withstanding temperatures as high as 150 °C.[39] Unfortunately $FAPbI_3$ was shown to phase instable forming a yellow photoinactive δ phase at room temperature.[40,41]

The phase stability of a perovskite film can be predicted by calculating the Goldschmidt tolerance factor

$$t = \frac{R_A + R_X}{\sqrt{2}(R_B + R_X)} \tag{6}$$

where $R_{A\text{-}X}$ are the ionic radii of the A, B, and X ions. For an ideal cubic perovskite to form, this factor must be between 0.9-1.0. However a perovskite will still form in the range 0.81-1.11 although the structure will be distorted into other phases due to tilting of the lead iodide octohedra (e.g. orthorhombic).[35,42] Due to the larger ionic radius of formamidinium the tolerance factor increases from 0.91 to 0.99 for $MAPbI_3$ and $FAPbI_3$ respectively. By blending 40% $FAPbI_3$ with 60% $MAPbI_3$ Pellet *et al.* were able to stabilise the perovskite phase whilst maintaining high photocurrent.[38] Jeon *et al.* built upon this work by blending together 85% $FAPbI_3$ and 15% $MAPbBr_3$ which allowed them to fabricate 19% efficient PSCs.[40] The use of the wider band gap $MAPbBr_3$ allowed a greater percentage of the final composition to be $FAPbI_3$ whilst maintaining phase stability.

In 2016 Saliba *et al.* incorporated caesium into a similar mixed-cation mixed-halide perovskite composition which further reduced the tolerance factor of the structure.[27,35] This allowed the fabrication of devices over 20% efficient which

maintained performance over 250 hours of continuous illumination at room temperature (albeit under a nitrogen atmosphere). This “triple-cation” perovskite has been adopted by many groups allowing the fabrication of reproducible, highly efficient, and relatively stable PSCs.

More recently, many groups have turned their attention to the addition of 2D perovskite additives to their absorber layers to enhance stability. Broadly a 2D perovskite contains cations that are too large to occupy the A site within the perovskite crystal structure.[43,44] These additional cations act as spacer layers that separate the regular perovskite crystal structure, creating 2D potential wells that confine charge. By increasing the quantity of the spacer cation, the width of these wells can be reduced which in turn will increase the size of the effective band gap of the perovskite. Furthermore the addition of a spacer acts to protect the perovskite material by preventing moisture ingress, although this reduces charge transfer lowering PCE.[43,45] To alleviate this problem several groups have begun to blend small quantities of 2D material into 3D perovskites which has been shown to extend operational stability whilst maintaining high PCE.[46,47]

2.3: Solution Processing of Perovskite Solar Cells

Much of the research interest in PSCs is due to the ease with which they can processed from solution. Creating a perovskite film is relatively straightforward, the challenge comes from controlling the wetting and subsequent crystallisation of the solution such that the resultant layer is as uniform as possible.

2.3.1: Wetting

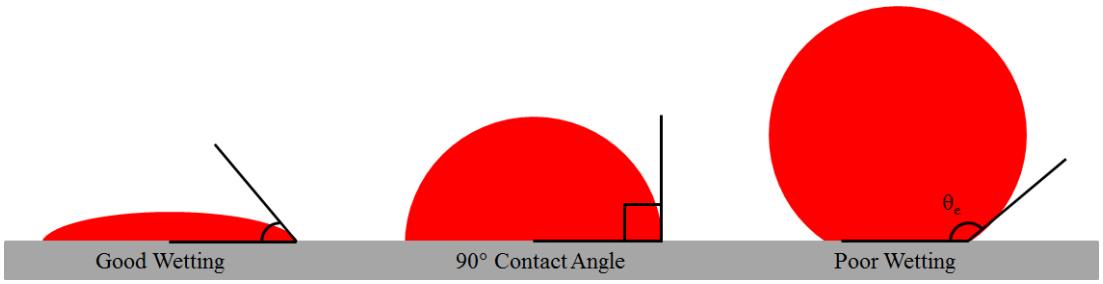

***Figure 10**: Diagram illustrating the wetting of three droplets of liquid on a substrate with increasing contact angle.*

Wetting describes the process of a liquid coming into contact with a solid surface. The ease with which this can occur is of key importance for all solution processing methods as without good wetting a uniform coating of the surface is impossible. A key parameter that quantifies wetting is the contact angle (θ_e) which is formed between the liquid and the solid surface. The contact angle can be calculated using the following expression,

$$cos(\theta_e) = \frac{\gamma_{SA} - \gamma_{SL}}{\gamma_{LA}} \quad (7)$$

where γ_{SA}, γ_{SL}, and γ_{LA} are the interfacial energies between the solid, air and the liquid.[48] Figure 8 shows the effect of increasing contact angle on the wetting of a droplet of liquid on a surface. The smaller the contact angle the better the solution will wet. This can be enhanced by using a solution with a low surface tension (γ_{LA}) and by utilising a substrate with a high surface energy (γ_{SA}).

2.3.2: Spin Coating

Spin coating is a reliable way to fabricate thin films over small areas and is widely used to fabricate highly efficient PSCs. In a typical deposition process a small quantity of solution is loaded onto the substrate before being accelerated up to

several thousand revolutions per minute (rpm). The shear forces induced by the rotation of the substrate cause the fluid to spread across the surface with the majority of it being thrown off and wasted. The remaining fluid dries due to the air flow across the sample during the spin cycle leaving behind a thin layer of solute. Any trapped solvent can then be extracted by heating the substrate after deposition.[49] The thickness of the resultant film can be approximated by the following relation

$$t \propto \frac{1}{\sqrt{\omega}} \tag{8}$$

where t is the thickness of the resultant film and ω is the spin speed.

2.3.2: Controlling the Crystallisation of Perovskite Thin Films

Perovskite thin films can be formed relatively simply, however the challenge comes from ensuring the morphology of the film is as uniform as possible. Over the years a variety of processing techniques have been developed to fabricate high quality perovskite layers to improve the efficiency of PSCs. Early $MAPbI_3$ films were deposited by spin coating a precursor solution and heating the resultant film to crystallise the perovskite layer.[8,10,13] In 2013 Burschka *et al.* developed a two-step method to deposit the perovskite layer. By first spin coating and drying a film of lead iodide prior to dipping the film in a solution of Methlyammonium Iodide, devices with a peak PCE of 15% were realised.[50] Other groups have subsequently adapted this method to use spin coating[51] and vapour exposure[52] to incorporate the organic component of the perovskite structure.

Anti-solvent quenching is a common method employed to rapidly crystallise the perovskite layer by exposing the precursor solution to a solvent in which the perovskite is not soluble. Jeon *et al.* demonstrated that dimethylsufoxide (DMSO) will form a crystalline intermediary phase with lead iodide when the perovskite solution was exposed to a drip of anti-solvent (in this case toluene) during spin coating.[53] Subsequent annealing of the DMSO intermediary phase drives the remaining solvent from the film, resulting in a highly uniform and smooth perovskite layer.[27] Anti-solvents can also be delivered via dipping the precursor film in bath of the solvent just after spin coating.[54] Whilst such processes are

undoubtedly effective there are questions as to how scalable they are as the use and recovery of large amounts of often toxic solvent is a challenge in an industrial setting. As such it has been shown that the anti-solvent method can be mimicked through exposure of the precursor film to a coarse vacuum. This drives out the primary solvent of the perovskite film (often Dimethylformamide) leaving the DMSO remaining in the film to form the intermediary phase.[55]

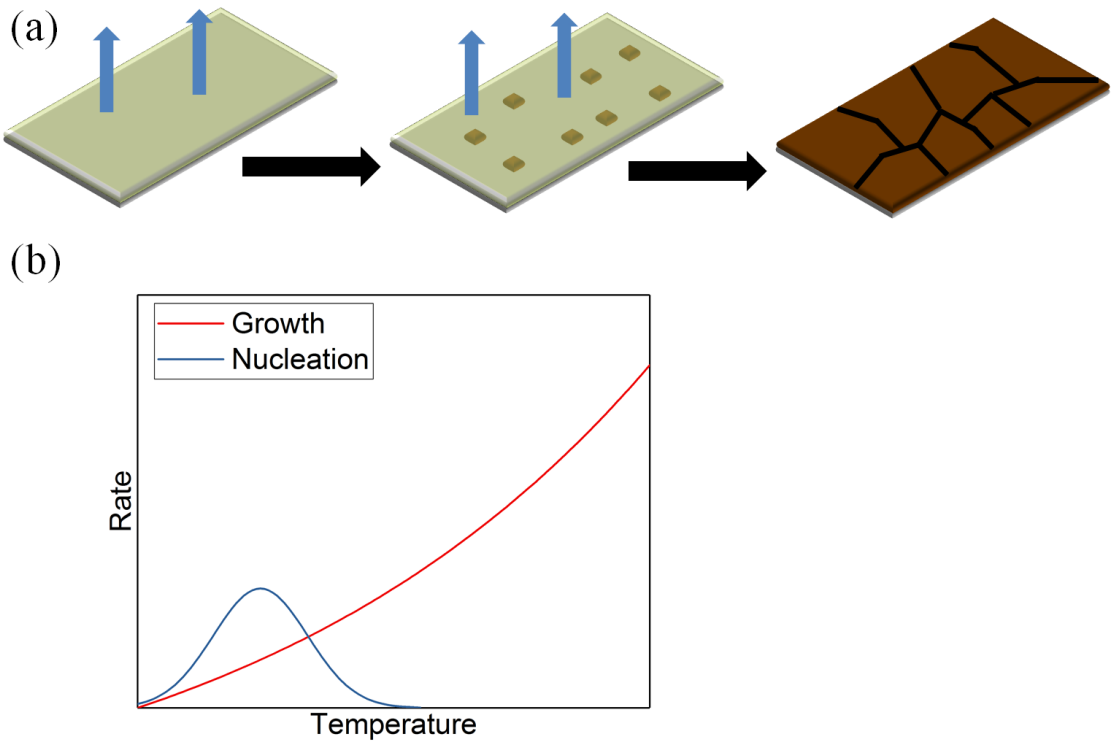

Figure 11: *(a) Diagram showing the nucleation and growth of a perovskite thin film. As the solvent is removed from the film nuclei will begin to form on the substrate. The density of nucleation sites will determine the size of the resultant crystals as they grow. Ideally the resultant film will be comprised of a number of grains hundreds of nanometres in size. (b) Graph displaying how the rates of crystal growth and nucleation vary with temperature. Adapted from ref. 56.*

The goal of all of the techniques outlined above is control the nucleation and subsequent growth of perovskite films (see Figure 11a). When the precursor solution is deposited upon a substrate, the perovskite components can spontaneously form nuclei from which further growth can occur. Due to the presence of the substrate, nuclei will preferentially form there due to the effective reduction in the interfacial energy. This nucleation process is highly dependent on

both the temperature and the saturation level of the solution. As the temperature increases, the available thermal energy also increases allowing more nuclei to form[56]. However the growth rate of nuclei also increases with temperature which prevents new nuclei from forming by depriving them of raw material needed to form new seed crystals. As a result of this the rate of nucleation has a peak whereas the rate of crystal growth increases exponentially with temperature (see Figure 11b).

Rapidly driving out solvent from the precursor film via anti-solvent/vacuum exposure causes the film to become supersaturated at room temperature. This favours the generation of a large number of nucleation sites across the substrate that can then grow into a uniform perovskite film characterised by crystal grains hundreds of nanometres in size. Simply heating the perovskite precursor film will supress nucleation leading to the formation of large, non-uniform perovskite crystals (see Chapters 5 and 6).

2.3.3: Scalable Deposition of Perovskite Solar Cells

Currently the most efficient PSCs reported in literature utilise spin coating to deposit perovskite thin films. However spin coating is poorly suited to coating large areas primarily due to the high degree of wasted material and thus alternative deposition techniques must be explored. One of the long term goals of all solution processed photovoltaic technologies is the development of a roll to roll (R2R) production process for fabricating large, flexible, and cheap solar cells.[57] In a R2R process, a flexible substrate is unrolled and fed through a coating system to deposit the various constituent layers of the device before being rolled up again. In many ways this process is analogous to newspaper printing and thus opens up the possibility of reducing the cost and energy payback time of solar technology. This section summarises a range of scalable deposition techniques that have been applied to PSCs.[58] An in depth discussion of developments in spray-coated PSCs is presented in Chapter 3.

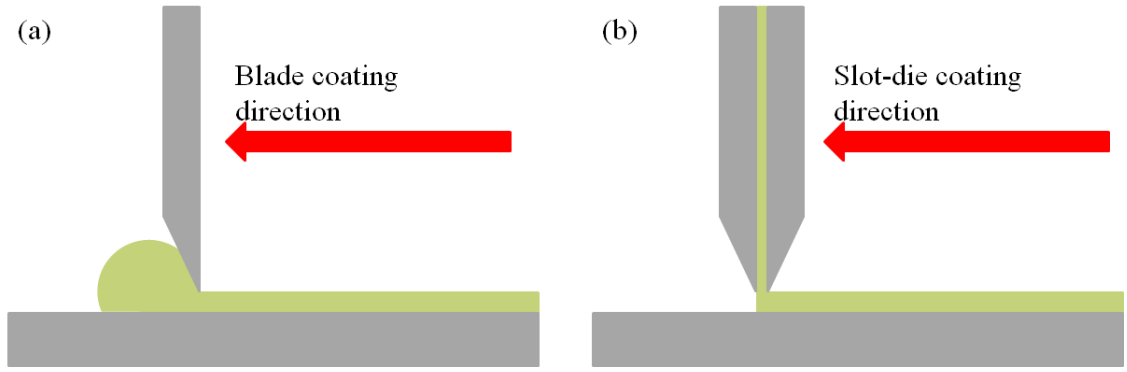

***Figure 12**: Schematic illustrations of blade (a) and slot-die (b) coating techniques.*

Blade coating is an extremely simple and effective deposition technique that has been successfully applied to PSCs.[59–61] Here solution is deposited onto a substrate and a blade is then swept across the substrate coating it in a thin film. The thickness of the resultant layer can be tuned by varying the concentration of the solution and the meniscus formed between the solution and the blade. This meniscus will depend on a range of factors including the surface tension/viscosity of the solution, surface energy of the substrate, geometry of the blade, and the speed with which it moves over the substrate.[62] Blade coated PSCs have reached an efficiency of over 20% on small area devices (<1 cm^2).[61] Air blading is a similar process in which a jet of high velocity gas is directed and scanned across the substrate. This coats and dries the solution simultaneously and has been shown to produce high efficiency (>20%) PSCs where all solution processed layers (ETL, perovskite, HTL) have been deposited in this manner.[60] Slot-die coating is a similar technique to blade coating where the solution is fed through a silt in a specially designed head which moves across the substrate depositing the solution.[58,63,64] Slot-die coating allows the deposited layers to be patterned into strips of various sizes by masking part of the slit. As such it is a popular method that can produce devices with over 18% PCE.[64]

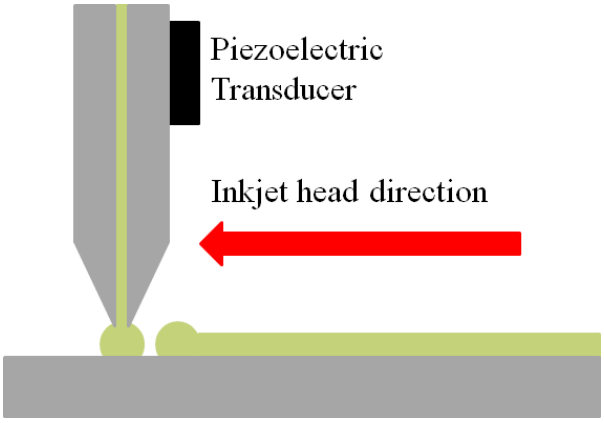

***Figure 13**: Schematic illustration of inkjet printing.*

Inkjet printing is a radically different technique that is widely used for office printing due to the high degree of control afforded. This enables detailed patterning of the deposited layers.[58] A solution is continuously delivered to the head and deposited through a nozzle as individual droplets created by a piezoelectric transducer. The head is motorised and moves across the surface depositing droplets with a uniform spacing. Careful engineering of the solution is required to ensure that the droplets wet and dry evenly across the surface. There have been a range of studies on inkjet printed PSCs with over 20% PCE demonstrated.[65–67]

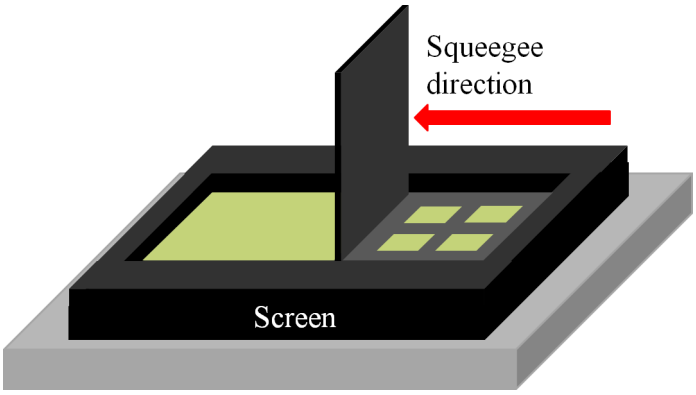

***Figure 14**: Schematic illustration of screen printing.*

Screen printing is simple and effective technique which utilises a patterned mesh that is overlaid onto the substrate. Ink is then deposited onto the mesh and coated onto the substrate by a squeegee which is scanned across the screen, forcing fluid through the pores in the mesh.[58] By varying the thickness of the mesh the quantity of solution deposited can be controlled. Gravure and relief printing are similar but R2R compatible processes where a coating drum with a pattern engraved onto it is used to deposit the fluid onto the substrate.[58] In 2014 Mei *et al.* utilised screen

printing to fabricate a novel PSC architecture comprising of three mesoporous layers.[68] This "triple mesoscopic stack" consisted of screen printed TiO_2, ZrO_2 and carbon black layers that were infiltrated with $MAPbI_3$ perovskite precursor. Here the TiO_2 and carbon black act as selective contacts separated by the electrically inert ZrO_2. These fully printed cells were capable of reaching 12.8% PCE with >1000 hours ambient stability under solar illumination. The remarkable stability of these devices was likely enhanced by the addition of a 5-Aminovaleric acid (5-AVA) which acts as a spacer to form a quasi 2D material.[46] More recent optimisation of this architecture has led to devices with 15.6% PCE.[69]

Whilst progress in scalable deposition of PSCs has been made the efficiencies still lag behind those of the best devices fabricated by spin coating. Furthermore the best reported efficiencies are for devices that are still smaller than 1 cm^2.[60,61,64,69] For these printing techniques to truly demonstrate viability in industrial setting devices with active areas of 1 m^2 must be fabricated with good PCE.

2.4: References

[1] J Nelson, *The Physics of Solar Cells*, Imperial College Press, **2003**.

[2] M. Fox, *Optical Properties of Solids*, 2nd Edition, Oxford University Press, **2010**.

[3] C. Kiittel, *Introduction to Solid State Physics*, 8th Edition, Wiley, **2004**.

[4] W. Shockley, H. J. Queisser, *J. Appl. Phys.* **1961**, *32*, 510.

[5] S. Rühle, *Sol. Energy* **2016**, *130*, 139.

[6] A. Rao, R. H. Friend, *Nat. Rev. Mater.* **2017**, *2*, 17063.

[7] K. A. Bush, A. F. Palmstrom, Z. J. Yu, M. Boccard, R. Cheacharoen, J. P. Mailoa, D. P. McMeekin, R. L. Z. Hoye, C. D. Bailie, T. Leijtens, I. M. Peters, M. C. Minichetti, N. Rolston, R. Prasanna, S. Sofia, D. Harwood, W. Ma, F. Moghadam, H. J. Snaith, T. Buonassisi, Z. C. Holman, S. F. Bent, M. D. McGehee, *Nat. Energy* **2017**, *2*, 17009.

[8] A. Kojima, K. Teshima, Y. Shirai, T. Miyasaka, *J. Am. Chem. Soc.* **2009**, *131*, 6050.

[9] S. R. Jang, K. Zhu, M. J. Ko, K. Kim, C. Kim, N. G. Park, A. J. Frank, *ACS Nano* **2011**, *5*, 8267.

[10] H.-S. Kim, C.-R. Lee, J.-H. Im, K.-B. Lee, T. Moehl, A. Marchioro, S.-J. Moon, R. Humphry-Baker, J.-H. Yum, J. E. Moser, M. Grätzel, N.-G. Park, *Sci. Rep.* **2012**, *2*, 591.

[11] B. O'Regan, M. Gratzel, *Nature* **1991**, *353*, 737.

[12] G. Yu, J. Gao, J. C. Hummelen, F. Wudl, A. J. Heeger, *Science.* **1995**, *270*, 1789.

[13] M. M. Lee, J. Teuscher, T. Miyasaka, T. N. Murakami, H. J. Snaith, **2012**, *338*, 643.

[14] S. D. Stranks, G. E. Eperon, G. Grancini, C. Menelaou, M. J. P. Alcocer, T. Leijtens, L. M. Herz, A. Petrozza, H. J. Snaith, *Science.* **2013**, *342*, 341.

[15] V. D'Innocenzo, G. Grancini, M. J. P. Alcocer, A. R. S. Kandada, S. D. Stranks, M. M. Lee, G. Lanzani, H. J. Snaith, A. Petrozza, *Nat. Commun.* **2014**, *5*, 3586.

[16] M. Liu, M. B. Johnston, H. J. Snaith, *Nature* **2013**, *501*, 395.

[17] Y. J. Jeon, S. Lee, R. Kang, J. E. Kim, J. S. Yeo, S. H. Lee, S. S. Kim, J. M. Yun, D. Y. Kim, *Sci. Rep.* **2014**, *4*, 26.

[18] D. Moia, I. Gelmetti, P. Calado, W. Fisher, M. Stringer, O. Game, Y. Hu, P. Docampo, D. Lidzey, E. Palomares, J. Nelson, P. R. F. Barnes, *Energy Environ. Sci.* **2019**, *12*, 1296.

[19] O. S. Game, G. J. Buchsbaum, Y. Zhou, N. P. Padture, A. I. Kingon, *Adv. Funct. Mater.* **2017**, *27*, 1606584.

[20] C. Motta, F. El-Mellouhi, S. Kais, N. Tabet, F. Alharbi, S. Sanvito, *Nat. Commun.* **2015**, *6*, 7026.

[21] T. Etienne, E. Mosconi, F. De Angelis, *J. Phys. Chem. Lett.* **2016**, *7*, 1638.

[22] N. K. Noel, B. Wenger, S. N. Habisreutinger, J. B. Patel, T. Crothers, Z. Wang, R. J. Nicholas, M. B. Johnston, L. M. Herz, H. J. Snaith, *ACS Energy Lett.* **2018**, *3*, 1233.

[23] T. J. Savenije, C. S. Ponseca, L. Kunneman, M. Abdellah, K. Zheng, Y. Tian, Q. Zhu, S. E. Canton, I. G. Scheblykin, T. Pullerits, A. Yartsev, V. Sundström, *J. Phys. Chem. Lett.* **2014**, *5*, 2189.

[24] Q. Dong, Y. Fang, Y. Shao, P. Mulligan, J. Qiu, L. Cao, J. Huang, *Science.* **2015**, *347*, 967.

[25] J. M. Ball, A. Petrozza, *Nat. Energy* **2016**, *1*, 16149.

[26] K. X. Steirer, P. Schulz, G. Teeter, V. Stevanovic, M. Yang, K. Zhu, J. J. Berry, *ACS Energy Lett.* **2016**, *1*, 360.

[27] M. Saliba, T. Matsui, J.-Y. Seo, K. Domanski, J.-P. Correa-Baena, N. Mohammad K., S. M. Zakeeruddin, W. Tress, A. Abate, A. Hagfeldt, M. Gratzel, *Energy Environ. Sci.* **2016**, *9*, 1989.

[28] W. S. Yang, B.-W. Park, E. H. Jung, N. J. Jeon, Y. C. Kim, D. U. Lee, S. S. Shin, J. Seo, E. K. Kim, J. H. Noh, S. Il Seok, *Science.* **2017**, *356*, 1376.

[29] W. Tress, N. Marinova, T. Moehl, S. M. Zakeeruddin, M. K. Nazeeruddin, M. Grätzel, *Energy Environ. Sci.* **2015**, *8*, 995.

[30] S. Van Reenen, M. Kemerink, H. J. Snaith, *J. Phys. Chem. Lett.* **2015**, *6*, 3808.

[31] J. H. Heo, H. J. Han, D. Kim, T. K. Ahn, S. H. Im, *Energy Environ. Sci.* **2015**, *8*, 1602.

[32] W. Ke, G. Fang, Q. Liu, L. Xiong, P. Qin, H. Tao, J. Wang, H. Lei, B. Li, J. Wan, G. Yang, Y. Yan, *J. Am. Chem. Soc.* **2015**, *137*, 6730.

[33] J. P. Correa Baena, L. Steier, W. Tress, M. Saliba, S. Neutzner, T. Matsui, F. Giordano, T. J. Jacobsson, A. R. Srimath Kandada, S. M. Zakeeruddin, A. Petrozza, A. Abate, M. K. Nazeeruddin, M. Grätzel, A. Hagfeldt, *Energy Environ. Sci.* **2015**, *8*, 2928.

[34] Q. Jiang, L. Zhang, H. Wang, X. Yang, J. Meng, H. Liu, Z. Yin, J. Wu, X. Zhang, J. You, *Nat. Energy* **2016**, *2*, 16177.

[35] Q. Fu, X. Tang, B. Huang, T. Hu, L. Tan, L. Chen, Y. Chen, *Adv. Sci.* **2018**, *5*, 1700387.

[36] A. M. A. Leguy, Y. Hu, M. Campoy-Quiles, M. I. Alonso, O. J. Weber, P. Azarhoosh, M. Van Schilfgaarde, M. T. Weller, T. Bein, J. Nelson, P. Docampo, P. R. F. Barnes, *Chem. Mater.* **2015**, *27*, 3397.

[37] B. Conings, J. Drijkoningen, N. Gauquelin, A. Babayigit, J. D'Haen, L. D'Olieslaeger, A. Ethirajan,

J. Verbeeck, J. Manca, E. Mosconi, F. De Angelis, H. G. Boyen, *Adv. Energy Mater.* **2015**, *5*, 1500477.

[38] N. Pellet, P. Gao, G. Gregori, T. Y. Yang, M. K. Nazeeruddin, J. Maier, M. Grätzel, *Angew. Chemie - Int. Ed.* **2014**, *53*, 3151.

[39] G. E. Eperon, S. D. Stranks, C. Menelaou, M. B. Johnston, L. M. Herz, H. J. Snaith, *Energy Environ. Sci.* **2014**, *7*, 982.

[40] N. J. Jeon, J. H. Noh, W. S. Yang, Y. C. Kim, S. Ryu, J. Seo, S. Il Seok, *Nature* **2015**, *517*, 476.

[41] C. C. Stoumpos, C. D. Malliakas, M. G. Kanatzidis, *Inorg. Chem.* **2013**, *52*, 9019.

[42] G. Kieslich, S. Sun, A. K. Cheetham, *Chem. Sci.* **2015**, *6*, 3430.

[43] D. H. Cao, C. C. Stoumpos, O. K. Farha, J. T. Hupp, M. G. Kanatzidis, **2015**, *137*, 7843.

[44] C. C. Stoumpos, D. H. Cao, D. J. Clark, J. Young, J. M. Rondinelli, J. I. Jang, J. T. Hupp, M. G. Kanatzidis, *Chem. Mater.* **2016**, *28*, 2852.

[45] H. Tsai, W. Nie, J. Blancon, C. C. Stoumpos, R. Asadpour, B. Harutyunyan, A. J. Neukirch, R. Verduzco, J. J. Crochet, S. Tretiak, L. Pedesseau, J. Even, M. A. Alam, G. Gupta, J. Lou, P. M. Ajayan, M. J. Bedzyk, M. G. Kanatzidis, A. D. Mohite, *Nat. Publ. Gr.* **2016**, *536*, 312.

[46] G. Grancini, C. Roldan-Carmona, I. Zimmermann, E. Mosconi, X. Lee, D. Martineau, S. Narbey, F. Oswald, F. De Angelis, M. Graẗzel, M. K. Nazeeruddin, *Nat. Commun.* **2017**, *8*, 15684.

[47] Z. Wang, Q. Lin, F. P. Chmiel, N. Sakai, L. M. Herz, H. J. Snaith, *Nat. Energy* **2017**, *2*, 17135.

[48] P. . de Gennes, .*Rev. Mod. Phys* **1985**, *57*, 827.

[49] Ossila, "Spin Coating: A Guide to Theory and Techniques," https://www.ossila.com/pages/spin-coating

[50] J. Burschka, N. Pellet, S.-J. Moon, R. Humphry-Baker, P. Gao, M. K. Nazeeruddin, M. Grätzel, *Nature* **2013**, *499*, 316.

[51] C.-H. Chiang, Z.-L. Tseng, C.-G. Wu, *J. Mater. Chem. A* **2014**, *2*, 15897.

[52] Q. Chen, H. Zhou, Z. Hong, S. Luo, H. S. Duan, H. H. Wang, Y. Liu, G. Li, Y. Yang, *J. Am. Chem. Soc.* **2014**, *136*, 622.

[53] N. J. Jeon, J. H. Noh, Y. C. Kim, W. S. Yang, S. Ryu, S. Il Seok, *Nat. Mater.* **2014**, *13*, 897.

[54] Y. Zhou, M. Yang, O. S. Game, W. Wu, J. Kwun, M. A. Strauss, Y. Yan, J. Huang, K. Zhu, N. P. Padture, *ACS Appl. Mater. Interfaces* **2016**, *8*, 2232.

[55] X. Li, D. Bi, C. Yi, J.-D. Décoppet, J. Luo, S. M. Zakeeruddin, A. Hagfeldt, M. Grätzel, *Science.* **2016**, *353*, 58.

[56] Y. Zhou, O. S. Game, S. Pang, N. P. Padture, *J. Phys. Chem. Lett.* **2015**, *6*, 4827.

[57] J. E. Carlé, M. Helgesen, O. Hagemann, M. Hösel, I. M. Heckler, E. Bundgaard, S. A. Gevorgyan, R. R. Søndergaard, M. Jørgensen, R. García-Valverde, S. Chaouki-Almagro, J. A. Villarejo, F. C. Krebs, *Joule* **2017**, *1*, 274.

[58] I. A. Howard, T. Abzieher, I. M. Hossain, H. Eggers, F. Schackmar, S. Ternes, B. S. Richards, U. Lemmer, U. W. Paetzold, *Adv. Mater.* **2019**, *1806702*, 1806702.

[59] Y. Deng, E. Peng, Y. Shao, Z. Xiao, Q. Dong, J. Huang, *Energy Environ. Sci.* **2015**, *8*, 1544.

[60] J. Ding, Q. Han, Q.-Q. Ge, D.-J. Xue, J.-Y. Ma, B.-Y. Zhao, Y.-X. Chen, J. Liu, D. B. Mitzi, J.-S. Hu, *Joule* **2019**, *3*, 402.

[61] W. Q. Wu, Q. Wang, Y. Fang, Y. Shao, S. Tang, Y. Deng, H. Lu, Y. Liu, T. Li, Z. Yang, A. Gruverman, J. Huang, *Nat. Commun.* **2018**, *9*, 1625.

[62] F. C. Krebs, *Sol. Energy Mater. Sol. Cells* **2009**, *93*, 394.

[63] D. Burkitt, J. Searle, D. A.Worsley, T. Watson, *Materials (Basel).* **2018**, *11*, 2106.

[64] J. B. Whitaker, D. H. Kim, B. W. Larson, F. Zhang, J. J. Berry, M. F. A. M. Van Hest, K. Zhu, *Sustain. Energy Fuels* **2018**, *2*, 2442.

[65] P. Li, C. Liang, B. Bao, Y. Li, X. Hu, Y. Wang, Y. Zhang, F. Li, G. Shao, Y. Song, *Nano Energy* **2018**, *46*, 203.

[66] S. G. Li, K. J. Jiang, M. J. Su, X. P. Cui, J. H. Huang, Q. Q. Zhang, X. Q. Zhou, L. M. Yang, Y. L. Song, *J. Mater. Chem. A* **2015**, *3*, 9092.

[67] F. Mathies, H. Eggers, B. S. Richards, G. Hernandez-Sosa, U. Lemmer, U. W. Paetzold, *ACS Appl. Energy Mater.* **2018**, *1*, 1834.

[68] A. Mei, X. Li, L. Liu, Z. Ku, T. Liu, Y. Rong, M. Xu, M. Hu, J. Chen, Y. Yang, M. Gra̍tzel, H. Han, *Science.* **2014**, *345*, 295.

[69] Y. Hu, Z. Zhang, A. Mei, Y. Jiang, X. Hou, Q. Wang, K. Du, Y. Rong, Y. Zhou, G. Xu, H. Han, *Adv. Mater.* **2018**, *30*, 1705786.

Chapter 3

Volume 9, Issue 8

2018/04/02

1977

THE JOURNAL OF PHYSICAL CHEMISTRY Letters

Advances in Spray-Cast Perovskite Solar Cells

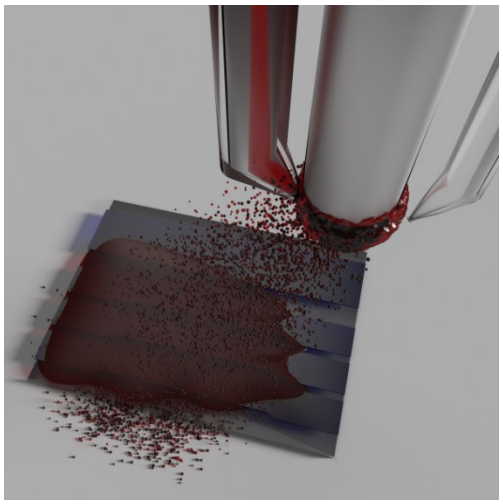

For the journals PDF:

DOI: 10.1021/acs.jpclett.8b00311

3.1: Publication Forward

In late 2017 the group was invited to write a perspective on spray-coating of perovskite solar cells by The Journal of Physical Chemical Letters. The subsequent article was split into four sections: firstly the background behind spray-coating is discussed focussing on four stages of deposition, secondly early work in spray-cast Organic Solar Cells is summarised, thirdly several papers in the field which are identified as significant are discussed, finally future challenges that the field needs to overcome are addressed. This paper serves as a good summary of the field and illustrates the challenges associated with spray-deposition of perovskites in particular. As a result this paper has been included within this thesis to supplement Chapter 2. Please note that the following publication discusses some results that will be further elaborated on in Chapter 5. As of the time of writing this paper has been cited 18 times.

3.2: Publication Main Body

Advances in Spray-Cast Perovskite Solar Cells

James E. Bishop, Thomas J. Routledge, David G. Lidzey*

Department of Physics & Astronomy, University of Sheffield, Hicks Building, Hounsfield Road, Sheffield, S3 7RH, U.K.

*Corresponding author, email d.g.lidzey@sheffield.ac.uk

Abstract

Spray-coating is deposition technique that is widely used in industry, and could in principle be used to fabricate perovskite photovoltaic (PV) devices at low cost and at high volume. As with any deposition technique, the fabrication of thin-films requires the optimisation of a range of parameter space in order to control film uniformity and homogeneity. This is particularly important in PV fabrication, as the quality of the thin film has an important effect on device efficiency. This perspective summarises the developments in spray-cast perovskite solar cells made over the past few years, with particular attention paid to strategies employed to control the crystallisation of the perovskite. Steady progress has now been made with spray-cast perovskite PV devices recently demonstrated having a power conversion efficiency of 18.3%. We highlight trends within the research field, and discuss challenges that will be necessary to drive such techniques towards practical application.

Publication Main Text

Over the past 8 years, perovskites have emerged as a promising third generation photovoltaic (PV) technology with power conversion efficiency (PCE) rising from an initial 3.8%[1] to 22.1%.[2] Perovskites are particularly interesting materials as they combine the properties of inorganic semiconductors (efficient light absorption, tunable bandgap, high charge-carrier mobility and low recombination rates) with the ease of processing from solution - a property that is typically associated with organic semiconductors.[3–5]

The ability to process such materials from solution opens the possibility of manufacturing extremely low-cost PV devices at high volume. Indeed, it has been predicted that PV modules fabricated in this manner would have an energy payback time of less than half a year; a value that compares very favourably with silicon based modules that have energy payback times of up to two and a half years dependent on their location.[6] However in order perovskite PV devices to be produced at high volume, it will be necessary to develop scalable deposition methods that can be used to produce high efficiency devices.

Currently most perovskite devices explored at lab-scale are fabricated by depositing a perovskite light absorber via spin-coating. Whilst this method is capable of producing devices having high performance, spin-coating is generally wasteful and not scalable for large scale (roll-to-roll) manufacturing. To address this issue, attention is now turning towards processing perovskite PV devices using scalable techniques such as slot-die coating,[7] blade coating,[8] ink-jet printing[9] and spray-coating,[10] with a general aim being to produce devices having an efficiency comparable to those prepared via spin coating.

In this perspective, we discuss the application of spray-deposition to fabricate perovskite PV. The attractiveness of this process comes from the fact that it is already used in industry such as automotive painting, and combines the advantages of fast throughput and high material utilisation. Importantly, spray-coating is compatible with non-planar surfaces; a feature that may lend it particular advantages as we discuss in the concluding sections. However the use of spray-coating is not without its challenges; in general, the fabrication of thin films by spray-coating generally relies on the use of "inks" that are formulated at relatively low solution concentrations, with the drying of the ink via solvent evaporation producing a film of the desired thickness. This is in contrast to inks formulated for spin-coating in which a much higher concentration is required to maintain high viscosity during the shear-based coating process. As a result of the low ink concentrations required in spray-deposition, solutions can often de-wet, and thus the coating process and ink formulation must be optimised to minimise "pooling" and dewetting during film drying. Here, a range of parameters can be optimised, including the nature and composition of the solvent, the solution concentration, fluid flow rate, spray-head height/speed and substrate temperature.[11] The optimisation of such a wide parameter space can be challenging, with process recipes often not being directly transferable between different research groups.

In the following sections, we summarise progress made in the field of spray-cast perovskite solar cells as well as addressing future research challenges. However we also include a short summary of progress made in the development of spray-cast organic (polymer-based) solar cells to place work on perovskite-based PV

devices into context. Note that this article presents a flavour of the most important progress in the field from the perspective of the authors, rather than being a full review of all work published on this topic. We direct any readers who wish to obtain a full description of the development of spray-cast thin-film and organic photovoltaic devices to a number of recent reviews.[12,13]

Most spray-coating processes can be broken down into four stages, namely (i) the generation of the ink-droplets, (ii) the transport of the droplets to the substrate, (iii) the coalescence of the droplets into a wet film, and (iv) thin-film drying.

The first stage in the spray-deposition process involves the break-up of an ink into a mist of micron sized droplets. One simple way to achieve this is to flow the ink through a nozzle that includes an orifice, with the ink being sheared as it is passes through the orifice. Whilst this "air-brush" type process is often used to coat conventional materials, the size of the droplets produced can vary; a limitation that has consequences for the uniformity of the resultant film.[14,15] As PV devices require close control over layer thickness, many researchers now use ultrasonic spray-coaters in which a piezoelectric crystal is used to resonate a tip at 10s of kHz. This vibration shears the ink into a mist of micron sized droplets characterised by an increased uniformity of droplet sizes as compared to an air brush.[10,14,15] Generally the mean diameter of droplets ($D_{0.5}$) produced can be approximated using the following empirical relation

$$D_{0.5} = 0.34\left(\frac{8\pi\sigma}{\rho f^2}\right)^{\frac{1}{3}} \quad (1)$$

where σ is the surface tension of the ink, ρ is its density and f is the frequency of the resonating tip.[15]

After the droplets have been generated they are then directed to the substrate of interest using a gas jet. In an ideal deposition, the droplets will then wet the surface, however this process is dependent on ink-density, droplet velocity, diameter, viscosity, nature of the substrate and the ink surface tension.[12] Arguably the most important of these parameters is the ink surface tension as this will affect the contact angle that the droplets make with the surface. If the contact

angle is too large, the droplets will not merge together into a wet film, but will instead dewet.[16]

A commonly employed strategy to improve surface-wetting is to heat the substrate during spray-deposition; this reduces the surface tension of the fluid and thus reduces its contact angle.[17] Indeed, the choice of substrate temperature is of key importance when optimising a spray-deposition process; if the temperature is too high the solvent will evaporate before the ink is able to spread and merge, resulting in a non-uniform film.[10,12] We note that this process is inevitable during spray-pyrolysis as the temperature of the substrate far exceeds the solvent boiling point. This problem is generally addressed by employing a multiple pass approach in which voids in the film are filled by subsequent passes of the spray-head. However films produced by this method are often very uneven, with one step deposition processes being generally preferred.[10–12,18–20]

One straight-forward way to reduce solvent contact angle is to use a solvent having a reduced surface tension, although this is often not possible as such solvents may not be able to properly dissolve the solute. A solution to this is to mix a secondary solvent into the ink that has a lower boiling point and reduced surface tension than the primary carrier solvent, with both primary and secondary solvents being mutually miscible (e.g. IPA and water). This approach can be used to enhance droplet spreading and merger into a wet film due to the solutal Marangoni effect.[16,21] On evaporation of the secondary solvent, the ink is able to flow over uncovered areas of the substrate via localised surface tension gradients. The Marangoni flow velocity (v_c) is given by

$$v_c^2 = \frac{1}{2\eta(x)}\frac{d\sigma}{dx}x(1-x)(-A_l\alpha_l + A_h\alpha_h) \quad (2)$$

in which η is the viscosity of the ink, σ is its surface tension, x is the volume fraction of the lower surface tension solvent, A_l and A_h are the evaporation rates of the low and high surface tension solvents respectively, and α_l and α_h are activity coefficients for the two solvents.[16]

Once a continuous wet film has been created over a substrate, the carrier solvent(s) ideally evaporate and leave a uniform film. However if a high boiling

point solvent is used, the prolonged drying times that result can lead to shrinkage or dewetting, creating a film that is characterised by large-area thickness variations. This effect can be avoided by accelerating the drying time by increasing the substrate temperature, however it is necessary to take into account the effect this will have on initial droplet wetting as too high a temperature may vaporise the solvent on contact.

Before the advent of perovskite solar cells, most PV spray-coating work focused on the development of organic photovoltaic solar-cells (OPVs). The first example of the use of spray-coated to produce an OPV was in 2007, where Vak *et al.* were able to fabricate the active layer of a P3HT:PCBM based device by spray-coating, with the device created having a PCE of 2.83%.[22] Clearly, a practical PV manufacture process based on spray-coating would ideally use similar spray-based techniques to deposit all layers in a PV device (i.e. active layer and charge extraction layers). The first example of a "multilayer" spray-cast OPV was demonstrated in 2009 when Hoth *et al.* spray-cast the hole transporting polymer PEDOT:PSS and a blend of P3HT:PCBM, achieving a PCE of 2.7%.[23] Importantly, this study highlighted the impact of the choice of solvent on the topography of spray-cast layers.

In 2010 Girotto *et al.* built upon this work and used a mixed solvent system to enhance the surface coverage of the films, with the efficiency of the resultant devices increasing to 3.75%.[16] The use of mixed solvent systems has subsequently become fairly common technique within the field.[11,16,24–26]

Further work addressed the development of multilayer spray-cast OPV, where both electron and hole-transporting layers (zinc oxide and PEDOT:PSS) were deposited by spray-coating in addition to the P3HT-PCBM active layer.[27] Here, device scale-up was also explored, with efficiencies of 3.17% and 1.33% achieved for devices having an active area of 0.36 cm^2 and 15.25 cm^2 respectively.

Further gains in efficiency were demonstrated in 2013, when Wang *et al.* fabricated a 5% efficient OPV device incorporating a spray-cast active layer.[28] Here, devices were based on the carbazole co-polymer PCDTBT rather than P3HT. Further efficiency gains were made in 2015 when multilayer OPVs were fabricated using PEDOT:PSS hole transport layer and an PFFBT4T-2OD:PC71BM active layer

blend, with devices fabricated having a PCE of 8.06%.[26] Figure 1 shows the peak efficiency of spray-cast OPV and perovskite devices discussed in this article against time.

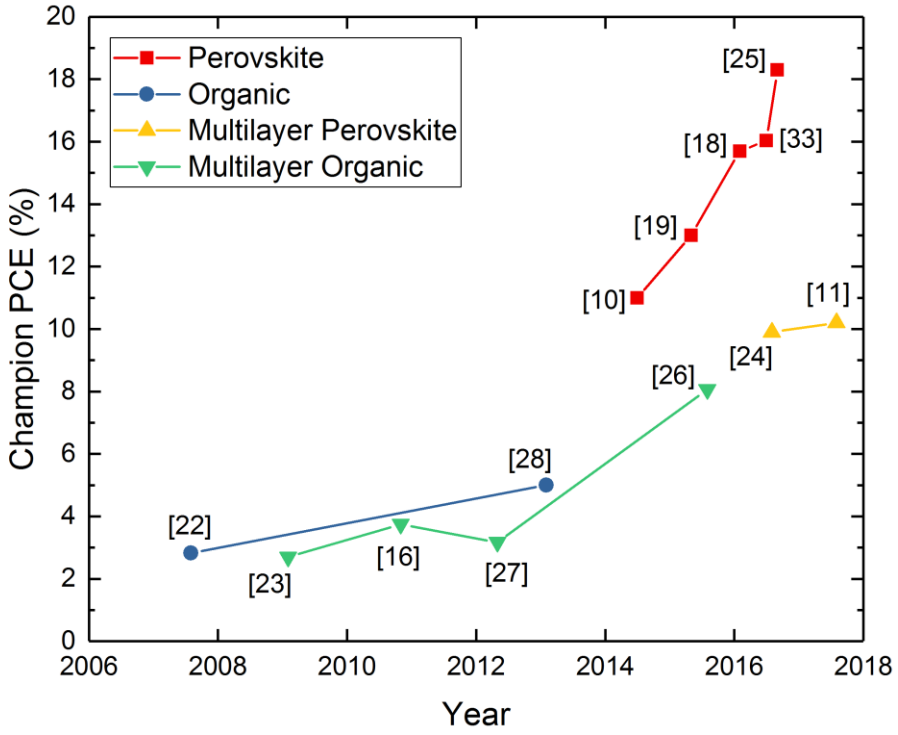

Figure 1: *Device efficiency improvements over time for spray-cast Organic (blue line) and Perovskite solar cells (red line) cited in this perspective. Organic and perovskite devices utilising more than one spray-cast layer (termed "multilayer" devices) are indicated using green and yellow symbols respectively.*

With the emergence of perovskite solar cells, a growing number of researchers have explored the fabrication of such materials via spray-deposition, with work building upon the techniques first developed for OPV fabrication. Here, initial work was undertaken by Barrows *et al.* at the University of Sheffield who utilised an ultrasonic spray coater to deposit a $CH_3NH_3PbI_{3-x}Cl_x$ perovskite solution, forming the active layer in an inverted architecture PV device. The devices constructed were based on a layer structure of ITO/PEDOT:PSS/Perovskite/PCBM/Ca/Al and achieved a peak PCE of 11%.[10]

Barrows *et al.* developed a simple process in which MAI and $PbCl_2$ powder were dissolved together in a DMF solvent at a molar ratio of 3:1 at a total concentration of 100 mg/ml and then deposited in a single spray pass using an ultra-sonic system onto a heated substrate under ambient conditions. The resultant dry film was then annealed in air to facilitate the crystallisation of the perovskite film.

It was found that it was necessary to control the precursor film drying-rate to maximise the quality of the resultant film (uniformity and lack of pinholes). For example, if the drying rate was too fast, the ink droplets dried before merging, with significant heterogeneities identified in the final film. Conversely, if the drying rate was too slow, the wet film underwent shrinkage or dewetting, resulting in a film having large-area thickness variations. By using a heated substrate, it was possible to use high boiling point solvents such as DMF without the necessity for prolonged drying times, with the films produced being of reasonably good quality.

An additional challenge encountered when spray-coating perovskite films is the necessity to control the crystallisation of the perovskite itself. Here, this process has been addressed extensively in spin-coating studies,[29,30] and it was noted that by changing the temperature of the device substrate during spray-deposition, it was possible to modify the morphology of the perovskite thin-film dramatically.[10] This is shown in Figure 2, where it can be seen that control of the deposition temperature can change the resultant size of the crystallites and the effective surface coverage of the perovskite film.

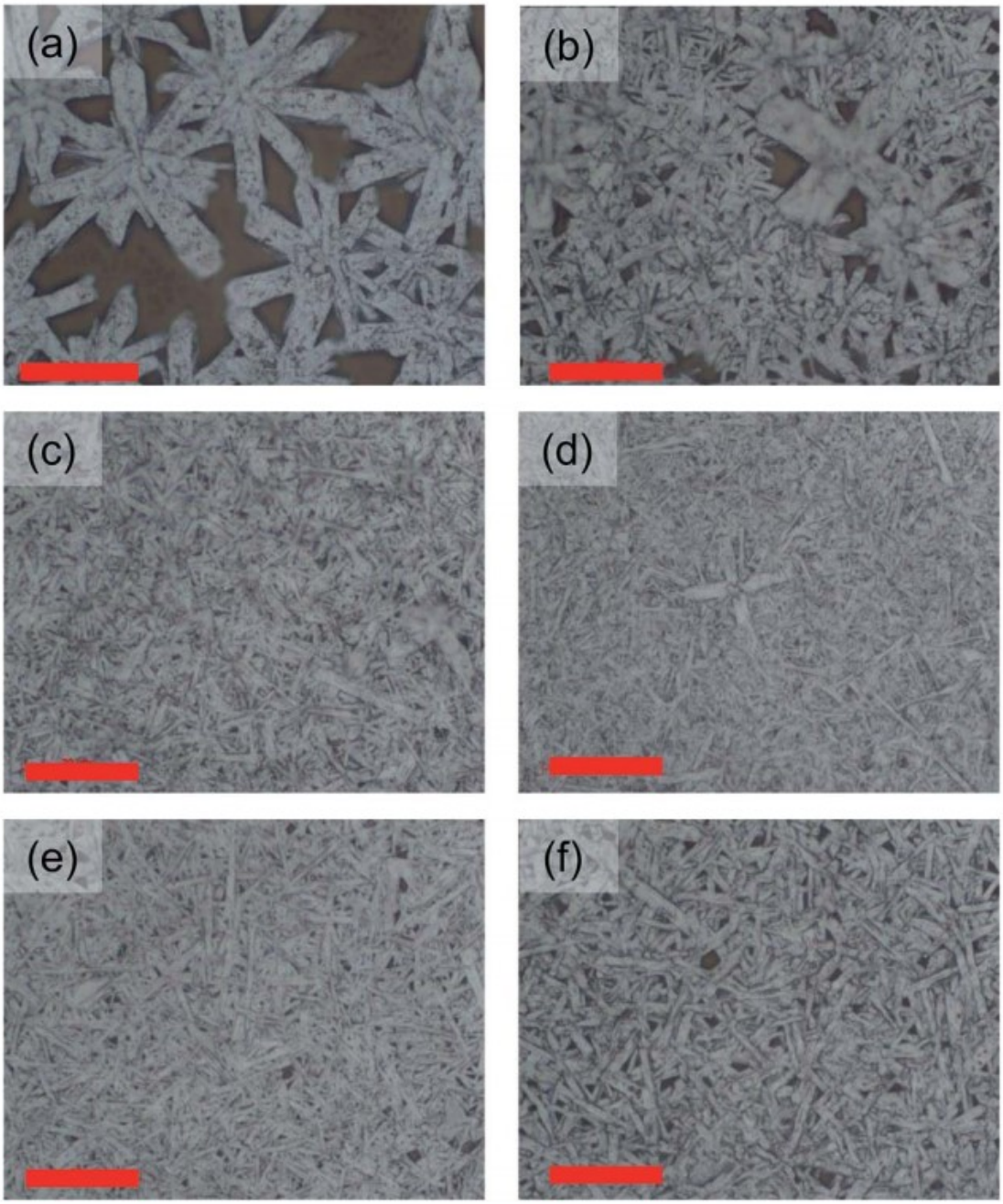

Figure 2: *Optical microscopy images of spray-deposited thin-films of methylammonium iodide and lead chloride onto substrates held at a range of elevated temperatures. (a) 28 ℃, (b) 38 ℃, (c) 55 ℃, (d) 75 ℃, (e) 80 ℃, (f) 87 ℃. The scale bar in each image corresponds to 20 mm. Reproduced from Ref. 10 with permission from The Royal Society of Chemistry.*

Following such progress, Das *et al.* used ultrasonic spray-deposition to fabricate a 13% efficient perovskite solar cell having a normal architecture (FTO/compact TiO_2/Perovskite/Spiro-OMeTAD/Au).[19] Again, an ultrasonic spray-coater was

used to deposit a $CH_3NH_3PbI_{3-x}Cl_x$ film in a manner very similar to that used by Barrows et al, with flexible devices fabricated onto ITO covered PET substrates having a PCE of 8.1%. It is generally difficult to deposit TiO_2 on ITO coated PET, as the TiO_2 hole-blocking contact requires sintering at 450 °C to become conductive; a temperature at which both ITO and PET undergo degradation. To address this issue, an infra-red lamp was used to sinter the TiO_2 layer whilst protecting the substrate. This process has already been applied to a perovskite precursor layer to speed up its conversion into a perovskite (a process that often requires an extended annealing time).[31]

In 2016 Tait *et al.* further increased the efficiency of spray-cast perovskite devices by fabricating a device fabricated from a lead acetate perovskite precursor ($Pb(C_2H_3O_2)_2$ or PbAc) having a PCE of 15.7%.[18] This device was scaled up to an active area of 3.8 cm^2 with modules demonstrated having an efficiency of 11.7%. Again, the active layer was deposited using an ultrasonic spray-coater, with the deposition performed within a nitrogen-filled glovebox environment. This offered control over humidity and oxygen levels which have been shown to improve perovskite crystallisation.[18,19]

Importantly, it was shown that a dual feed spray-head could be used to mix different perovskite precursors. Indeed, by controlling the flow rate, the relative ratio of the precursor materials could be tuned dynamically to determine an optimal blend ratio. Using a mixture of 25% $CH_3NH_3PbI_{3-x}Cl_x$ and 75% $CH_3NH_3PbI_{3-x}Ac_x$, it was shown that optimal efficiency could be achieved. It is known that lead acetate based mixtures form ultra-smooth high quality perovskite films that can be thermally converted from the precursor to the full perovskite after 10 minutes annealing (regular $CH_3NH_3PbI_{3-x}Cl_x$ films often require anneal times in excess of one hour).[32] Such properties are likely to be valuable in any high-speed production process. Figure 3 shows a schematic of the dual-head deposition process. Note the three stages of spray-deposition: (i) droplets landing on the substrate, (ii) coalescence of droplets into a wet film, and (iii) drying of the film.[18]

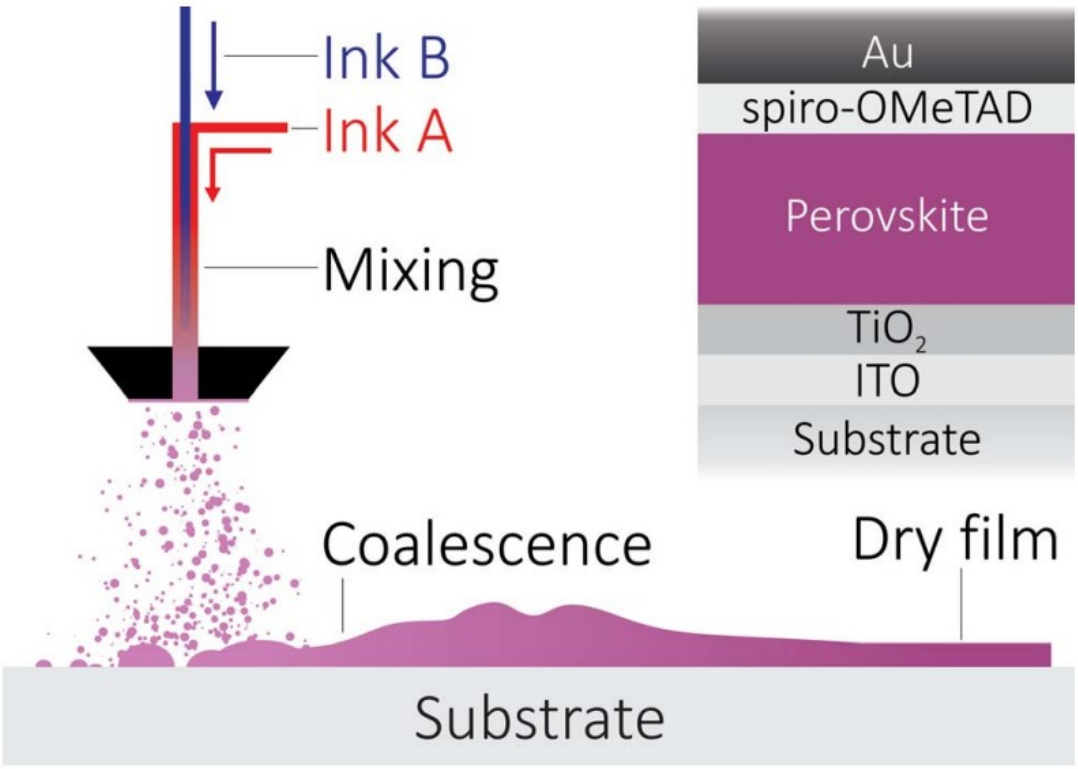

Figure 3: *Schematic of concurrently pumped ultrasonic spray coating for perovskite precursor deposition. The inks ultrasonically mix inside the nozzle, prior to aerosolization. The inset shows the basic device architecture implemented. Reproduced from Ref. 18 with permission from The Royal Society of Chemistry.*

A two-step method to spray-coat $CH_3NH_3PbI_3$ perovskite has also been demonstrated by Huang *et al.*, with devices demonstrating an efficiency of 16.03% on small-area cells and 13.09% on 1 cm^2 devices.[33] This approach was based on the work of Burschka et al in which a lead iodide film was deposited via spin coating, and then infiltrated with MAI via dip coating to form a perovskite[29]. Others had previously used spray-coating to infiltrate the lead iodide scaffold but Huang et al was the first to spray both layers.[33–36]

A schematic of the process developed is shown in Figure 4. Firstly a PbI_2 film was deposited from DMSO using an ultrasonic spray-coater onto a heated substrate.[33] Next MAI in IPA was spray-coated onto a dry PbI_2 layer. This mixed film was then heated at 100 °C for 2 hours to ensure all of the precursor underwent reaction, forming the perovskite. Again the substrate temperature during spray-casting was shown to be of key importance. A high temperature deposition-process (90 °C) effectively removed all DMSO from the film, yielding a dense PbI_2 layer. However if

the PbI_2 film was too dense, it was found that its reaction with MAI was incomplete, resulting in a film that was not fully converted. If the deposition temperature was instead lowered to 60 °C it was found that some of the DMSO solvent was left in the film, allowing the MAI to infiltrate and undergo diffusion more easily. Using this technique, it was found possible to create large-area high quality perovskite films and efficient PV devices.

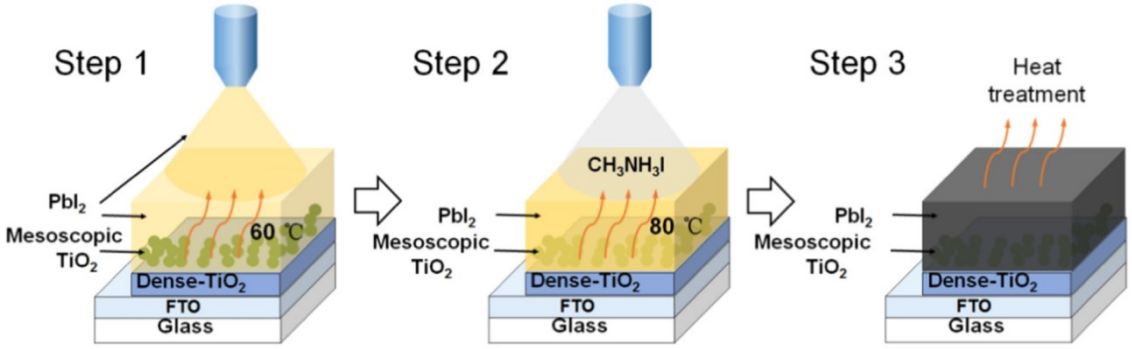

Figure 4: *Schematic diagram of the two-step spray method for the deposition of perovskite $CH_3NH_3PbI_3$ film. In Step one, PbI_2 dissolved in DMSO is ultrasonic sprayed onto the FTO/TiO2 substrate at 60 ℃. In step two, the CH_3NH_3I in isopropanol is sprayed onto the PbI_2 film at 80 ℃. In step three, the as-prepared film is heat treated to promote the interdiffusion reaction between PbI_2 and CH_3NH_3I and crystallization of $CH_3NH_3PbI_3$. Reproduced from Ref. 33 with permission from Elsevier.*

In 2016 Heo *et al.* reported (to the best of our knowledge) the highest performance spray-cast perovskite devices, having a PCE of 18.3%.[25] Here, a different deposition technique was employed, where a precursor fluid was continuously spray-cast onto a surface over a period of several minutes, where the outgoing flux of evaporating solvent was balanced by an incoming flux of fresh precursor ink. This method is in direct contrast to previous spray-based techniques in which the deposition process lasted for several seconds only.

In the process developed, MAI was first reacted with lead chloride in IPA to form $CH_3NH_3PbI_{3-x}Cl_x$ nanocrystals that were then washed, forming a high purity $CH_3NH_3PbI_{3-x}Cl_x$ nanocrystalline powder. This powder was then dissolved in a mixture of DMF and GBL. As GBL has a higher boiling point than DMF, the GBL extended the film drying rate despite the high temperature of the substrate during

the spray-deposition (120 °C); a method that allowed the perovskite crystal growth times to be extended.

It was shown that by controlling the ratio of DMF to GBL, it was possible to balance the solvent flux out of the film due to evaporation with the incoming flux of fresh solution. Indeed, if the solution simply consisted of DMF, the solvent flux out of the film was too high and the film dried rapidly forming a film characterised by small grains. However if the solution contained too much GBL, the flux into the film was much larger than the evaporation flux, resulting in solution dewetting. It was found that a solvent blend ratio of 80% DMF to 20% GBL was necessary to balance the incoming and outgoing solvent fluxes and thus reach a dynamic equilibrium. A schematic diagram of this process is shown in Figure 5. This process allowed crystals that had been formed to re-dissolve and then merge into much larger grains. This created a dense film composed of micron-sized grains that resulted in the creation of high performance devices. Using this method 10 x 10 cm^2 modules were created (FTO/TiO_2/Perovskite/Spiro-OMeTAD/Au) having an efficiency of 15.5%. We note however that such a long deposition times (around 2 minutes) would not be compatible with a high-speed manufacture process.

In an ideal commercial perovskite PV manufacture process, all solution-processed layers would be deposited via spray-deposition under ambient conditions. This was demonstrated in 2016 by Mohamad *et al.*, who reported an inverted device architecture based on spray-cast PEDOT:PSS, $CH_3NH_3PbI_{3-x}Cl_x$, and PCBM, with devices achieving an average efficiency of 7.1±1.7% (peak 9.9%) relative to a spin-cast reference of 12.1±0.9%.[24] To the best of our knowledge this is the first example of an spray-cast perovskite device in which all the layers were sequentially deposited under ambient conditions, with a single spray pass used to deposit each layer; a technique that would be compatible with a production line.[11,24,37–39]

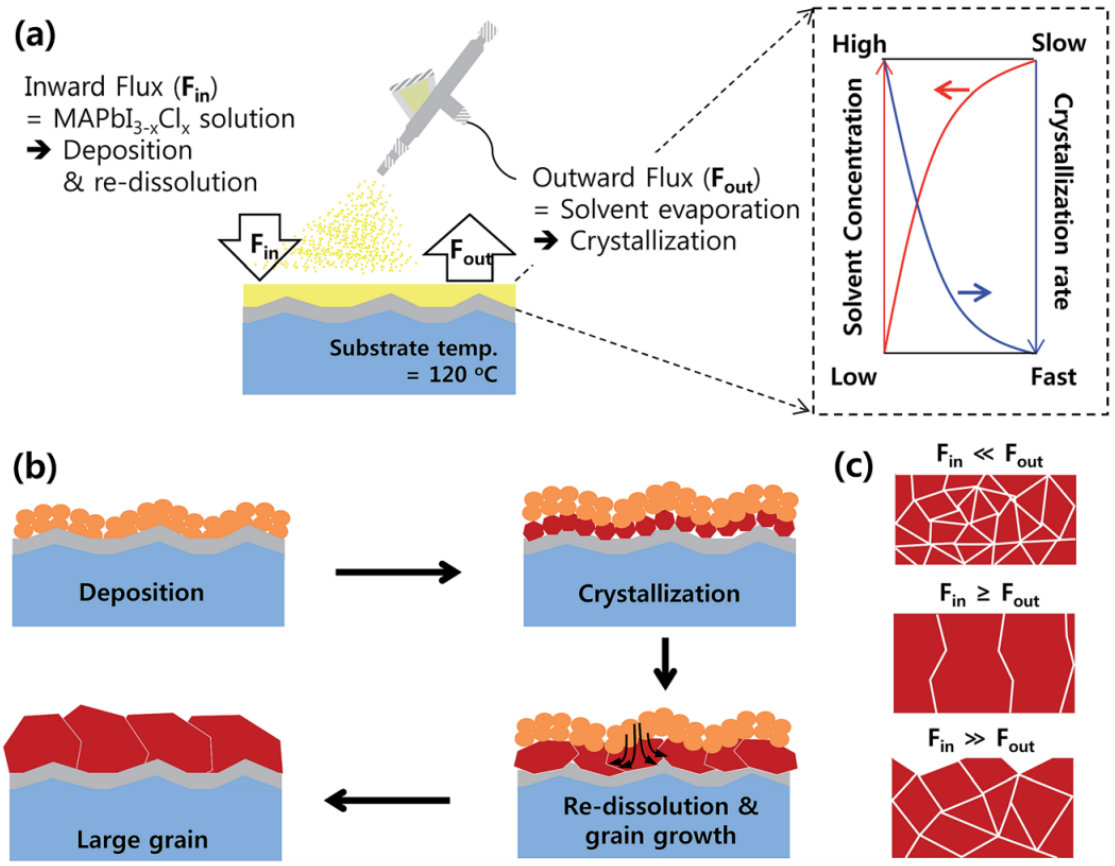

Figure 5: *Schematic illustration of (a) the proposed mechanism of the spray coating process, (b) crystalline grain growth, and (c) the morphology of the formed crystalline grains in the perovskite film with respect to the balance between F_{in} and F_{out}. Reproduced from Ref. 25 with permission from The Royal Society of Chemistry.*

Later work by Bishop *et al.* built upon this work by switching to a normal architecture (FTO/compact TiO_2/Mesoporous TiO_2/Perovskite/Spiro-OMeTAD/Au).[11] Here, a spray-based process was developed to sequentially deposit compact TiO_2, mesoporous TiO_2, $CH_3NH_3PbI_{3-x}Cl_x$, and spiro-OMeTAD. Again each layer was deposited in a single spray pass under ambient conditions. The devices created had an average efficiency of 9.2±0.6% (peak 10.2%) relative to a spin-cast reference of 11.4±1.0% on small-area devices. Significantly, it was found that compared to a spin-cast reference, there was some reduction in device efficiency observed which was mainly attributed to the quality of the spray-cast spiro-OMeTAD film that tended to de-wet. Some scale-up of the process was explored, with devices having an active area of 1.5 cm^2 demonstrated to have an efficiency of 6.9%. Here the efficiency reduction on scale-up was attributed to a reduction in PV fill factor resulting from a higher series resistance of the FTO

channel-lengths used. Improved patterning of this device would have likely improved its performance. One limitation identified by Mohamad et al and Bishop et al is the quality of the perovskite layer that can be spray-cast under ambient conditions. It is likely that better control over perovskite crystallisation will further enhance the efficiencies of multilayer all spray-cast devices.

It is important to develop a spray-based process that will allow devices to have an efficiency that approaches the most efficient devices fabricated by spin-casting, which currently have a PCE in excess of 22.1%.[2] At present, the most efficient spray-cast devices have an efficiency of around 18% and thus there is still significant work to be done in order to optimise this process.[25] Until now almost all spray-cast devices rely on methylammonium lead triiodide as the perovskite absorber. However state-of-the-art perovskite devices are now increasingly based on mixed cation formulations that generally incorporate caesium and formamidinium in addition to methylammonium at the A site position.[2,40] Such perovskites have enhanced efficiency and stability and are more likely to be the absorber of choice in a commercial device.[40]

In addition to the use of more complex perovskite formulations, it will also be necessary to integrate them with the highest performance hole and electron transport layers, with all such layers ideally deposited using spray-based processes.[41] Recent progress has been made into the use of copper thiocyanate (CuSCN) as an efficient hole-transporting material.[39,42] Significantly, this material has recently been deposited by spray-coating in a perovskite device (where only the CuSCN layer was spray-cast) with an efficiency of 17.1% demonstrated[39]. Notably however, attempts to spray-cast a spiro-OMeTAD hole-transporting layer have been frustrated by a tendency of the film to undergo dewetting from the perovskite surface[11]. This effect appeared to be promoted by the addition of dopant molecules to the spiro-OMeTAD to improve its conductivity, however it was found that dewetting could be largely suppressed by the use of viscosity modifiers.[11] Such additives have also been used to suppress dewetting of PEDOT:PSS films, and thus this approach could be applied more generally when formulating semiconductor inks for spray-coating applications.[43] Note however it will be important to explore the extent to which such materials can be used (even

within the perovskite active layer) to improve processing and film morphology without compromising electronic functionality.

The use of spray-coating also offers an opportunity to dispense entirely with the use of hole-transport materials. Here, the development of graded perovskite heterostructures created through vertical control of halide concentration within a device can be used to manipulate the electric field distribution and thereby enhance electron-hole splitting and hole extraction without the use of a hole-transporting semiconductor.[44] We believe, the ability to spray-cast perovskite semiconductors opens an interesting opportunity to develop such concepts by fabricating nanoscale structures within the perovskite absorber layer that cannot easily be formed through a regular solution-based deposition route. For example, by utilising a perovskite precursor ink that rapidly dries and crystallises during the spray-mist phase, it should be possible to deposit perovskite nanoparticles as a "dry" film onto other perovskite layers. This may allow a series of different perovskite materials to be deposited using a multiple-pass spray-process, with graded heterojunctions formed that offer a tailored control over electric-field and band offsets within a device.

Up to now, most work on the development of spray-cast PV devices has concentrated on the fabrication of relatively small devices or simple modules. The scale-up of this technology however will require individual devices to be patterned, allowing them to be connected together forming a device module. While thin-films can be patterned by spray-casting through a mask or stencil, this is not practical for high volume roll-to-roll manufacture. For this reason, it will be necessary to use a laser-based ablation technique to pattern the various layers within a spray-cast device. Laser machining of semiconductor films is already at an advanced stage and routinely used in manufacture, and thus such techniques could be readily adapted.[45]

It is important to acknowledge that whilst it is likely a process to fabricate high efficiency multilayer spray-cast PSCs will be developed, this does not necessarily mean that it will successfully transition into the commercial market. Silicon based devices, traditionally held back by high cost, have in recent years dramatically

reduced in price and continue to do so. Decades of research and development have brought module costs down to the point where they are equal to if not exceeded by those of the balance of systems.[46] Open questions remain as to whether a commercial perovskite module will ever reach a cost low enough to give it a significant edge over industrially mature silicon. Therefore we must look for new ways the technology can be applied to disrupt silicon's near monopoly of the market. This may involve creating perovskite-silicon tandem cells,[47] or to look for new opportunities to use perovskite cells in areas in which silicon based devices are unsuitable.

As spray-coating does not involve the close proximity of a coating head to a surface, it will in principle be possible to use it to fabricate PV devices over non-planar surfaces. This opens up the opportunity to coat PV devices over a range of different structural materials and thereby integrate PV onto complex, structured surfaces in a seamless and “invisible” fashion. This offers the potential to integrate PV with the built environment, the surface of airplane wings, autonomous aerial vehicles and automobiles etc. Here, distinct challenges remain; firstly, such surfaces may be much rougher than the well-controlled transparent conductive oxide materials that are often used to prototype devices. This will require the use of planarization layers to control the roughness of the surface of interest. Secondly, problems with inks dewetting and “running” are likely to be more severe when depositing over a three-dimensional surface, and thus various techniques will be necessary to control the motion of the ink, such as the use of viscosity modifiers and air-knives. It will also be necessary to develop high-performance encapsulation systems that are compatible with deposition over non-planar surfaces.

Looking further forward, it will be possible to use spray-coating to fabricate a range of other thin-film devices including perovskite light-emitting diodes. Here, such devices could be integrated over a variety of non-planar surfaces, creating an attractive media for lighting and signage etc.

In conclusion, significant progress has been made in the fabrication of perovksite PV via spray-coating. Such techniques however present a series of challenges

through the development of ink formulation and optimisation of parameter-space to create uniform thin films. However, the deposition of solution processable semiconductor materials via spray-coating offers a ready method to fabricate a range of electronic thin-film devices at high speed with low wastage. The coming years will determine whether this technology makes the transition from lab-based demonstrations to a practical manufacture environment.

Author Information

James Bishop was born and raised in the Black Country west of Birmingham (UK). In 2015 he graduated with an M.Phys from the University of Sheffield. He is currently studying for a Ph.D in Spray-Cast Perovskite Solar Cells as a member of the Electronic and Photonic Molecular Materials group (EPMM) under the supervision of Prof David Lidzey.

Thomas Routledge, originally from Solihull, Birmingham (UK), has been in Sheffield since 2010. In 2014 he received his M.Phys from the University of Sheffield. He is currently studying for a Ph.D in Spray-Cast Organic Light-Emitting Diodes under the supervision of Dr Alastair Buckley as a member of the EPMM group.

David Lidzey is originally from London, and studied for his B.Sc (1985-88) and Ph.D (1990-95) degrees in Physics at the University of Birmingham. Between degrees, he worked for Kodak Ltd (Harrow), undertaking research into new photographic products. In 1995, he moved to the University of Sheffield to undertake postdoctoral research in polymer LEDs. He was promoted to a personal Chair in Physics in 2007, and has held Fellowships from Lloyds of London and the EPSRC. He has an interest in the commercialisation of research, and is the Chairman and co-founder of the materials science company Ossila. His research interests are broad, and include the development of photovoltaic devices based on molecular materials and perovskites, spectroscopy of organic thin films, and photonic and polaritonic structures and devices based on organic and hybrid semiconductors.

Acknowledgment

The authors thank the UK EPSRC for funding this work via research grants "EP/I028641/Polymer/fullerene photovoltaic devices: new materials and innovative processes for high-volume manufacture", EP/J017361/1 and EP/P02484X/1 (Supergen Supersolar) and EP/M025020/1 "High resolution mapping of performance and degradation mechanisms in printable photovoltaic devices". The authors also thank Dave Coles for providing the graphical TOC entry. J.B. and T.R. thank the University of Sheffield for providing PhD scholarships.

3.3: Further Context

Following the publication of this paper other groups have reported on spray-cast perovskite solar cells although the highest efficiency devices remain those fabricated by Heo *et al.* in 2016. Chapters 7 and 8 summarise key developments from 2018 onwards.

3.4: References

[1] A. Kojima, K. Teshima, Y. Shirai, T. Miyasaka, *J. Am. Chem. Soc.* **2009**, *131*, 6050.

[2] W. S. Yang, B.-W. Park, E. H. Jung, N. J. Jeon, Y. C. Kim, D. U. Lee, S. S. Shin, J. Seo, E. K. Kim, J. H. Noh, S. Il Seok, *Science.* **2017**, *356*, 1376.

[3] M. A. Green, A. Ho-baillie, H. J. Snaith, *Nat. Photonics* **2014**, *8*, 506.

[4] G. E. Eperon, S. D. Stranks, C. Menelaou, M. B. Johnston, L. M. Herz, H. J. Snaith, *Energy Environ. Sci.* **2014**, *7*, 982.

[5] S. D. Stranks, G. E. Eperon, G. Grancini, C. Menelaou, M. J. P. Alcocer, T. Leijtens, L. M. Herz, A. Petrozza, H. J. Snaith, *Science.* **2013**, *342*, 341.

[6] J. Gong, S. B. Darling, F. You, *Energy Environ. Sci.* **2015**, *8*, 1953.

[7] T. M. Schmidt, T. T. Larsen-Olsen, J. E. Carlé, D. Angmo, F. C. Krebs, *Adv. Energy Mater.* **2015**, *5*, 1500569.

[8] Y. Deng, E. Peng, Y. Shao, Z. Xiao, Q. Dong, J. Huang, *Energy Environ. Sci.* **2015**, *8*, 1544.

[9] S. G. Li, K. J. Jiang, M. J. Su, X. P. Cui, J. H. Huang, Q. Q. Zhang, X. Q. Zhou, L. M. Yang, Y. L. Song, *J. Mater. Chem. A* **2015**, *3*, 9092.

[10] A. Barrows, A. Pearson, C. Kwak, A. Dunbar, A. Buckley, D. Lidzey, *Energy Environ. Sci.* **2014**, *7*, 2945.

[11] J. E. Bishop, D. K. Mohamad, M. Wong-Stringer, A. Smith, D. G. Lidzey, *Sci. Rep.* **2017**, *7*, 7962.

[12] M. Eslamian, *Coatings* **2014**, *4*, 60.

[13] A. Reale, L. La Notte, L. Salamandra, G. Polino, G. Susanna, T. M. Brown, F. Brunetti, A. Di Carlo, *Energy Technol.* **2015**, *3*, 385.

[14] S. Bose, S. S. Keller, T. S. Alstrøm, A. Boisen, K. Almdal, *Langmuir* **2013**, *29*, 6911.

[15] M. Majumder, C. Rendall, M. Li, N. Behabtu, J. A. Eukel, R. H. Hauge, H. K. Schmidt, M. Pasquali, *Chem. Eng. Sci.* **2009**, *65*, 2000.

[16] C. Girotto, D. Moia, B. P. Rand, P. Heremans, *Adv. Funct. Mater.* **2011**, *21*, 64.

[17] G. J. Gittens, *J. Colloid Interface Sci.* **1969**, *30*, 406.

[18] J. G. Tait, S. Manghooli, W. Qiu, L. Rakocevic, L. Kootstra, M. Jaysankar, C. A. Masse de la Huerta, U. W. Paetzold, R. Gehlhaar, D. Cheyns, P. Heremans, J. Poortmans, *J. Mater. Chem. A* **2016**, *4*, 3792.

[19] S. Das, B. Yang, G. Gu, P. C. Joshi, I. N. Ivanov, C. M. Rouleau, T. Aytug, D. B. Geohegan, K. Xiao, *ACS Photonics* **2015**, *2*, 680.

[20] J. Yao, L. Yang, F. Cai, Y. Yan, R. S. Gurney, D. Liu, T. Wang, *Sustain. Energy Fuels* **2017**, *2*, 436.

[21] X. Fanton, A. M. Cazabat, *Langmuir* **2002**, *14*, 2554.

[22] D. Vak, S.-S. Kim, J. Jo, S.-H. Oh, S.-I. Na, J. Kim, D.-Y. Kim, *Appl. Phys. Lett.* **2007**, *91*, 081102.

[23] C. N. Hoth, R. Steim, P. Schilinsky, S. A. Choulis, S. F. Tedde, O. Hayden, C. J. Brabec, *Org. Electron. physics, Mater. Appl.* **2009**, *10*, 587.

[24] D. K. Mohamad, J. Griffin, C. Bracher, A. T. Barrows, D. G. Lidzey, *Adv. Energy Mater.* **2016**, *6*, 1600994.

[25] J. H. Heo, M. Lee, M. H. Jang, S. H. Im, *J. Mater. Chem. A* **2016**, *4*, 17636.

[26] Y. Zhang, J. Griffin, N. W. Scarratt, T. Wang, D. G. Lidzey, *Prog. Photovoltaics Res. Appl.* **2011**, *24*, 275.

[27] J. W. Kang, Y. J. Kang, S. Jung, M. Song, D. G. Kim, C. S. Kim, S. H. Kim, *Sol. Energy Mater. Sol. Cells* **2011**, *103*, 76.

[28] T. Wang, N. W. Scarratt, H. Yi, A. D. F. Dunbar, A. J. Pearson, D. C. Watters, T. S. Glen, A. C. Brook, J. Kingsley, A. R. Buckley, M. W. A. Skoda, A. M. Donald, R. A. L. Jones, A. Iraqi, D. G. Lidzey, *Adv. Energy Mater.* **2013**, *3*, 505.

[29] J. Burschka, N. Pellet, S.-J. Moon, R. Humphry-Baker, P. Gao, M. K. Nazeeruddin, M. Grätzel, *Nature* **2013**, *499*, 316.

[30] W. S. Yang, J. H. Noh, N. J. Jeon, Y. C. Kim, S. Ryu, J. Seo, S. I. Seok, *Science.* **2015**, *348*, 1234.

[31] S. Sanchez, X. Hua, N. Phung, U. Steiner, A. Abate, *Adv. Energy Mater.* **2018**, *8*, 1702915.

[32] W. Zhang, M. Saliba, D. T. Moore, S. K. Pathak, M. T. Hörantner, T. Stergiopoulos, S. D. Stranks, G. E. Eperon, J. A. Alexander-Webber, A. Abate, A. Sadhanala, S. Yao, Y. Chen, R. H. Friend, L. A. Estroff, U. Wiesner, H. J. Snaith, *Nat. Commun.* **2015**, *6*, 6142.

[33] H. Huang, J. Shi, L. Zhu, D. Li, Y. Luo, Q. Meng, *Nano Energy* **2016**, *27*, 352.

[34] F. Li, C. Bao, H. Gao, W. Zhu, T. Yu, J. Yang, G. Fu, X. Zhou, Z. Zou, *Mater. Lett.* **2015**, *157*, 38.

[35] K. M. Boopathi, M. Ramesh, P. Perumal, Y. C. Huang, C. S. Tsao, Y. F. Chen, C. H. Lee, C. W. Chu, *J. Mater. Chem. A* **2015**, *3*, 9257.

[36] X. Xia, W. Wu, H. Li, B. Zheng, Y. Xue, J. Xu, D. Zhang, C. Gao, X. Liu, X. Xia, W. Wu, H. Li, B. Zheng, Y. Xue, J. Xu, D. Zhang, C. Gao, X. Liu, *RSC Adv.* **2016**, *6*, 14792.

[37] H. Huang, J. Shi, S. Lv, D. Li, Y. Luo, Q. Meng, *Chem. Commun.* **2015**, *51*, 10306.

[38] J. Troughton, D. Bryant, K. Wojciechowski, M. J. Carnie, H. Snaith, D. A. Worsley, T. M. Watson, *J. Mater. Chem. A* **2015**, *3*, 9141.

[39] I. S. Yang, M. R. Sohn, S. Do Sung, Y. J. Kim, Y. J. Yoo, J. Kim, W. I. Lee, *Nano Energy* **2017**, *32*, 414.

[40] M. Saliba, T. Matsui, J.-Y. Seo, K. Domanski, J.-P. Correa-Baena, N. Mohammad K., S. M. Zakeeruddin, W. Tress, A. Abate, A. Hagfeldt, M. Gratzel, *Energy Environ. Sci.* **2016**, *9*, 1989.

[41] M. Wong-stringer, J. E. Bishop, J. A. Smith, D. K. Mohamad, A. J. Parnell, V. Kumar, D. G. Lidzey, *J. Mater. Chem. A Mater. energy Sustain.* **2017**, *5*, 15714.

[42] N. Arora, M. I. Dar, A. Hinderhofer, N. Pellet, F. Schreiber, S. M. Zakeeruddin, M. Grätzel, *Science.* **2017**, *358*, 768.

[43] J. Griffin, A. J. Ryan, D. G. Lidzey, *Org. Electron. physics, Mater. Appl.* **2017**, *41*, 245.

[44] B. Li, Y. Zhang, L. Zhang, L. Yin, *Adv. Mater.* **2017**, *29*, 1701221.

[45] Y. Galagan, H. Fledderus, H. Gorter, H. H. 't Mannetje, S. Shanmugam, R. Mandamparambil, J. Bosman, J.-E. J. M. Rubingh, J.-P. Teunissen, A. Salem, I. G. de Vries, R. Andriessen, W. A. Groen, *Energy Technol.* **2015**, *3*, 834.

[46] Z. Zhou, M. Carbajales-Dale, *Energy Environ. Sci.* **2018**, *11*, 603.

[47] K. A. Bush, A. F. Palmstrom, Z. J. Yu, M. Boccard, R. Cheacharoen, J. P. Mailoa, D. P. McMeekin, R. L. Z. Hoye, C. D. Bailie, T. Leijtens, I. M. Peters, M. C. Minichetti, N. Rolston, R. Prasanna, S. Sofia, D. Harwood, W. Ma, F. Moghadam, H. J. Snaith, T. Buonassisi, Z. C. Holman, S. F. Bent, M. D. McGehee, *Nat. Energy* **2017**, *2*, 17009.

Chapter 4

Experimental Methods

4.1: Introduction

In keeping with University of Sheffield's guidelines for alternative format theses, experimental Chapters 5-7 are presented in publication format with their own separate and comprehensive methods sections. Therefore to avoid repeating content, this chapter presents an expanded discussion of several selected techniques employed to fabricate and characterise perovskite solar cells.

4.2: Materials

As has been previously discussed a typical perovskite solar cell consists of a vertical stack of materials designed to separate and extract electrons and holes generated within the perovskite absorber layer. Within the literature, a wide range of materials have been utilised each with their own advantages and disadvantages. For the sake of brevity here a description of the materials is limited to those used within Chapters 5-7. Figure 1 presents the energy level values relative to vacuum for the materials used in this thesis for the fabrication of PSCs.

Indium and fluorine doped tin oxide (ITO/FTO) coated glass substrates are both utilised as transparent conductive oxides upon which the devices are assembled. Titanium oxide (TiO_2)[1] and Tin Oxide (SnO_2)[2] are intrinsic n-type semiconductors used as electron selective contacts to the perovskite layer. Due to their deep valence band maxima they are effective at blocking holes.

Two perovskite absorber layers are used within this thesis. Methylammonium lead iodide can be formed either by a 3:1 mixture of methylammonium iodide (CH_3NH_3I/MAI) and lead chloride ($CH_3NH_3PbI_{3-x}Cl_x$/$MAPbI_{3-x}Cl_x$), or by a 1:1 mixture of MAI and lead iodide ($CH_3NH_3PbI_3$/$MAPbI_3$). Both approaches result in a film with the exact same band-gap despite the trace amount of chlorine present in

the $MAPbI_{3-x}Cl_x$ film.[3] Caesium-containing triple cation perovskites are also used in later chapters ($CsI_{0.05}((FAPbI_3)_{0.85}(MAPbBr_3)_{0.15})_{0.95}$/C-TC).[4]

Spiro-OMeTAD (2,2',7,7'-Tetrakis[N,N-di(4-methoxyphenyl)amino]-9,9'-spirobifluorene)[5] is a small molecule commonly used as a hole selective contact when it is p-doped through the addition of Li-TFSI (bis(trifluoromethanesulfonyl)imide), TBP (4-tert-butyl-pyridine) and FK209 (tris(2-(1H-pyrazol-1-yl)-4-tert-butylpyridine)cobalt(II) di[hexafluorophosphate]). Metallic gold (Au) is used as an electrical top contact.

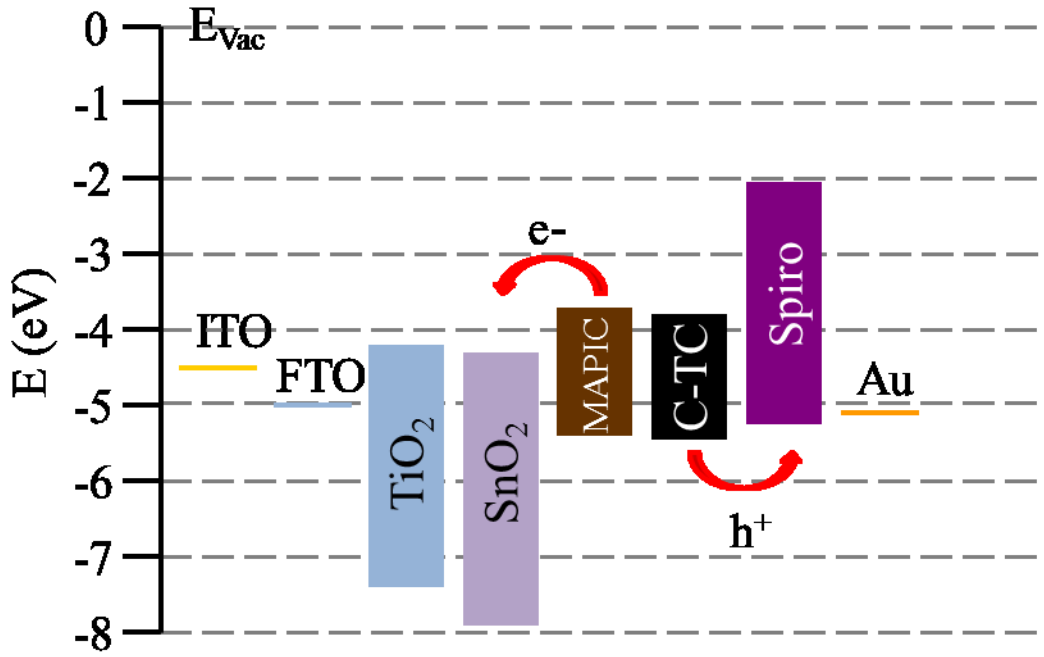

Figure 1: *Energy level alignment of the materials used in this thesis for the fabrication of perovskite solar cells, relative to vacuum.*

4.3: Deposition Techniques

4.3.1: Spin Coating

Here the substrate is held in place by a chuck with an appropriately sized recess to hold the substrate it in place. In a typical deposition a small quantity of solution (10-60 µL) is placed onto the substrate using a micropipette, before being accelerated up to several thousand revolutions per minute (rpm) for around 30 seconds.[6]

4.2.2: Spray-coating

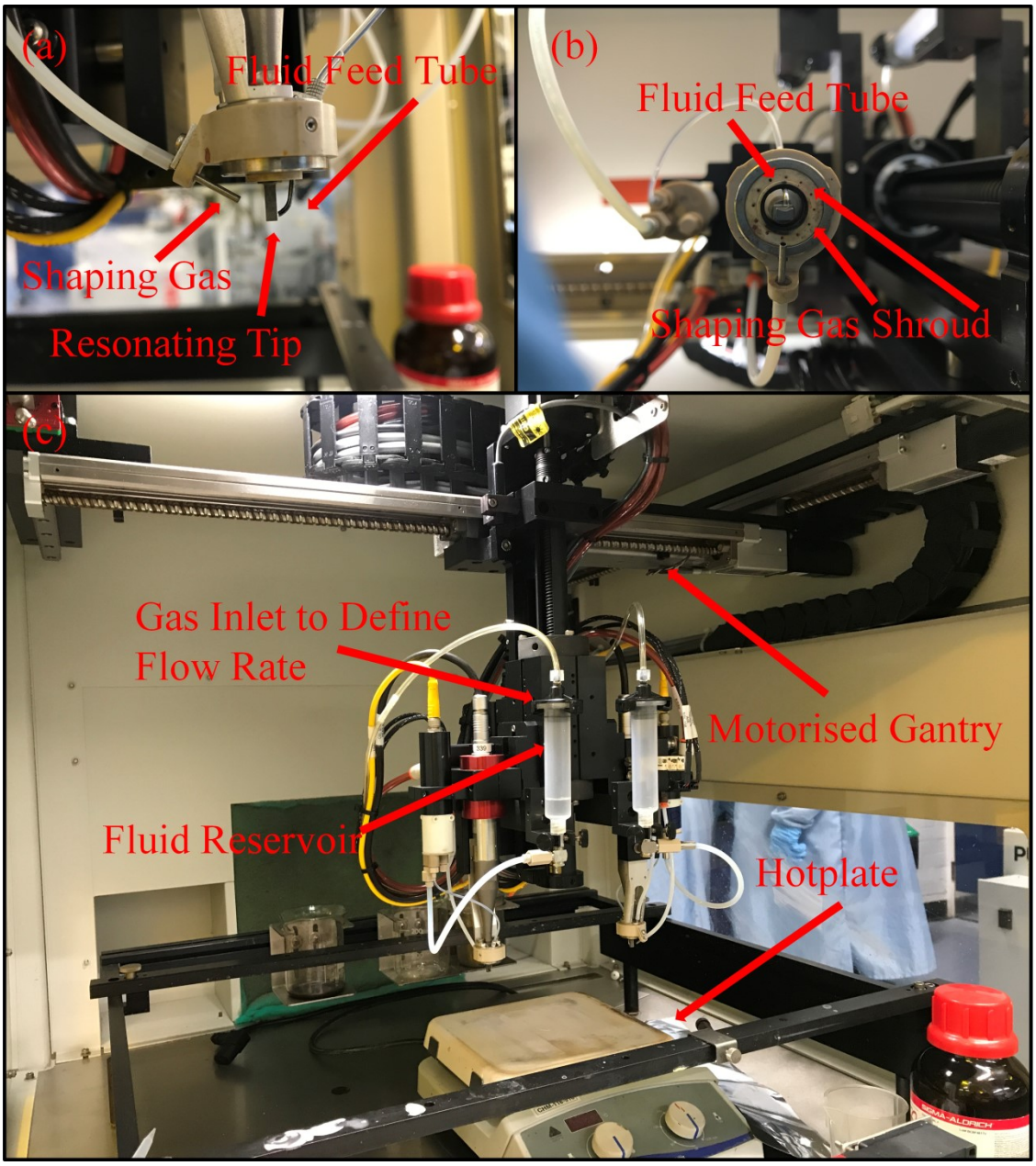

Figure 2: *Labelled photographs of the Prism Ultra-coat 300 spray-coater (USI) used for the fabrication of perovskite solar cells. Part (a) shows a side profile of one of the two spray-heads. Part (b) shows a view from below a spray-head. Part (c) shows the entire coating system mounted onto a motorised gantry.*

The general theory of spray-coating has already been discussed in Chapter 3. Here we give a more in depth description of the two automated spray-coaters used in Chapters 5-7. The first piece of equipment is a Prism Ultra-coat 300 system manufactured by Ultrasonic Industries (USI). Figure 2a shows a side profile of one of the two heads mounted within the system. The head has no nozzle and instead

uses a feed tube delivering solution onto a tip, which is then resonated to 30 kHz to aerosolise the fluid into a mist of micron sized droplets. A shaping gas (nitrogen) then guides the droplets as the head moves. Part (b) shows a view from below the head, where further shaping gas feeds are evident in a ring around the tip, which essentially collimate the mist down onto the surface being coated. Part (c) shows a full view of the system with both spray-heads in view as well as the motorised gantry. Fluid is stored in a reservoir which has a nitrogen gas inlet attached to the top creating an air tight seal. The gas pressure within the reservoir can be adjusted in order to control the flow rate of the solution onto the tip during deposition.

In a typical spray-deposition process the head is moved to a start position at a specific height above the surface. Then the ultrasonic tip, shaping gas, and fluid coating valve are triggered. Solution begins to flow onto the tip with a rate controlled by the pressure in the reservoir and a spray mist is formed. The head then moves in a line across the substrate coating it in solution before reaching its end position.

The Prism system has been in the Sheffield group for several years. Its main benefits are its low solution consumption and ease of maintenance. As the fluid feed tube to the tip is relatively short, the system requires about 1 mL of solution to fill the dead volume within the line. This minimises wasted solution when performing experiments which is a valuable property when using expensive materials such as spiro-OMeTAD. Cleaning the line is straightforward as the system is easy to access and only small quantities of solvent are required to flush any residue out of the line. The system does have a couple of major drawbacks. Firstly the flow rate ($mLmin^{-1}$) for any given deposition is not explicitly set in the software; instead the pressure applied to the solution in the reservoir tunes the flow rate. This means that there is uncertainty about the exact flow rate the system is delivering during deposition as it depends on the viscosity of the solution and surface tension, as well as the quality of the seal at the top of the reservoir. Secondly the system is housed within a humidity controlled lab however the solution is still exposed to both oxygen and water during deposition. Perovskites in particular are sensitive to this and as a result the quality of films produced by this system is limited.

In 2016 a Sonotek Exactacoat system was purchased that is mounted in a glovebox. The system has two different spray-heads but only the “Impact” head (shown in Figure 3a) was used for the work in this thesis. Unlike the USI system, the Impact head has a piezoelectric nozzle which can be resonated to create an antinode at the tip that shears the fluid into droplets. These droplets are then guided down onto the substrate by a flat jet gas deflector. Fluid is driven through the tip at a rate defined by a syringe driver shown in part (b). Part (c) shows the whole system and the motorised gantry within the glovebox.

The main benefit of this system is that it allows deposition in an inert atmosphere which is particularly useful when processing perovskite films. Furthermore as the system uses a syringe driver, the flow rate is more controllable than the USI system. However as the solution carrier line is much longer the dead volume is significantly higher (3 mL). As a result the Sonotek system requires much more solution to operate in comparison to the USI spray-coater (at least 5 mL).

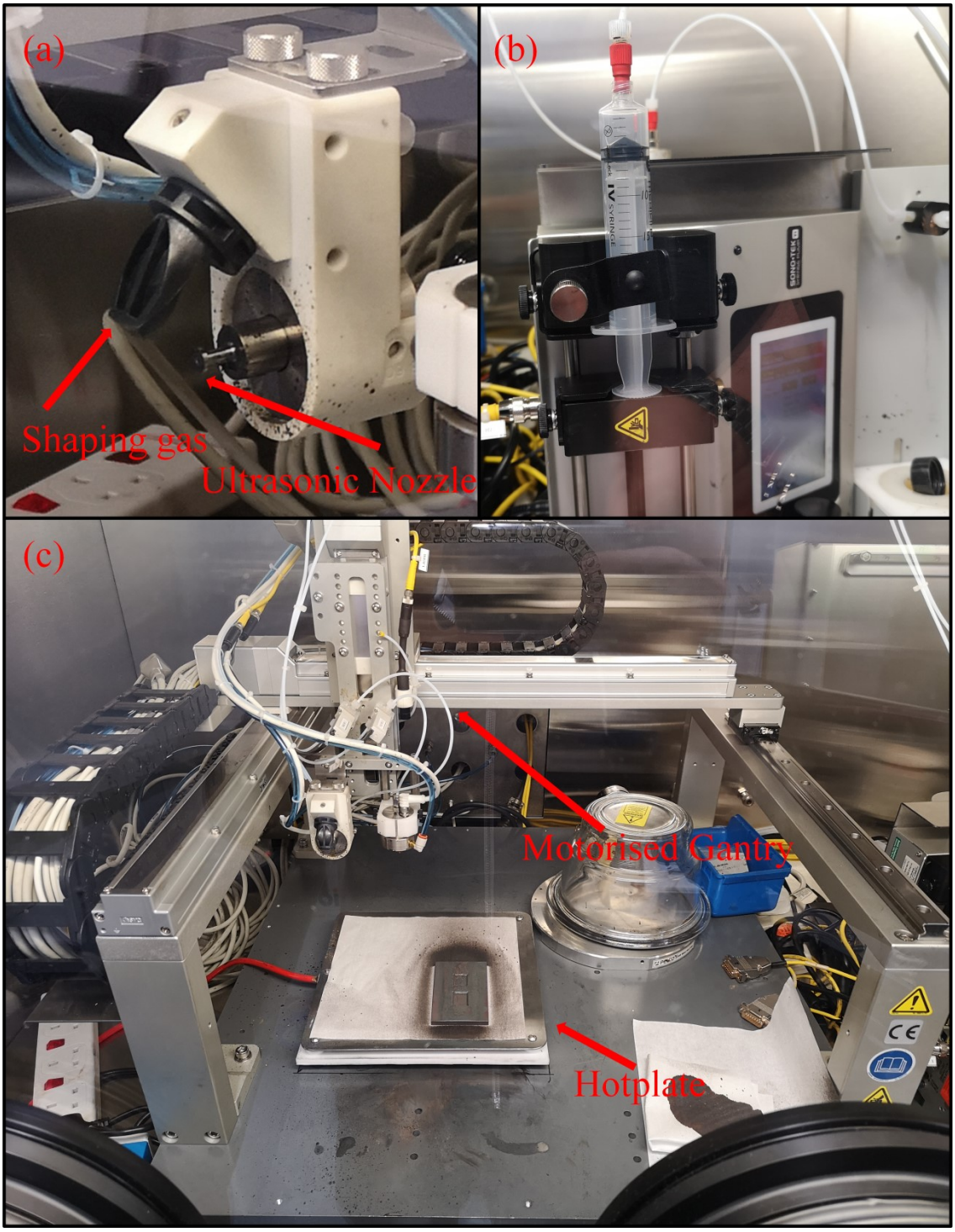

Figure 3: *Labelled photographs of the Exactacoat ultrasonic spray-coater. Part (a) shows a close up of the "Impact" spray-head. Part (b) shows an image of the syringe driver used to control the flow rate. Part (c) shows the entire coating system mounted onto a motorised gantry.*

4.3.3: Thermal Evaporation

Electrical contacts for perovskite solar cells were deposited via thermal evaporation using an Edwards bell jar evaporator. Here the devices are loaded into the vacuum chamber and a pump removes the air from the chamber. This ensures that during the deposition the metal atoms can travel unimpeded. Once the pressure reaches at least $4x10^{-6}$ mbar a tungsten boat containing a small amount of gold is heated by passing a large amount of current through it. This evaporates the metal which then travels up and nucleates onto the substrates. A calibrated quartz crystal gauge measures the rate of deposition (normally around 1 As^{-1}), which can be controlled by changing the current passed through the tungsten boat. By mounting the substrates in an evaporation mask, the metal contacts formed can be patterned into well-defined shapes.

4.4: Device Fabrication

In this section we outline the steps for the fabrication of perovskite solar cells within this thesis (see Figure 4). The vast majority of devices were fabricated on 20 mm x 15 mm glass substrates coated in either FTO or ITO. Larger area devices have been fabricated and further details of these devices are presented in Chapters 5-7.

4.4.1: Etching and Cleaning Substrates

The first stage of the device fabrication process is the chemical etching of the substrates forming spatially separated contacts. In order to do this roughly two thirds of each substrate is masked with Kapton tape. Next zinc powder is sprinkled onto the exposed ITO/FTO in order to facilitate the reaction of a small quantity of 4 mol Hydrochloric acid. The zinc acts to reduce the surface of the TCO attracting H_3O ions. This leads to the formation of hydrogen ions which penetrate the tin oxide and break the bonds between the tin and the oxygen. This reaction happens within a few seconds and the residue can be removed with a cotton bud before the proceeding to the cleaning step

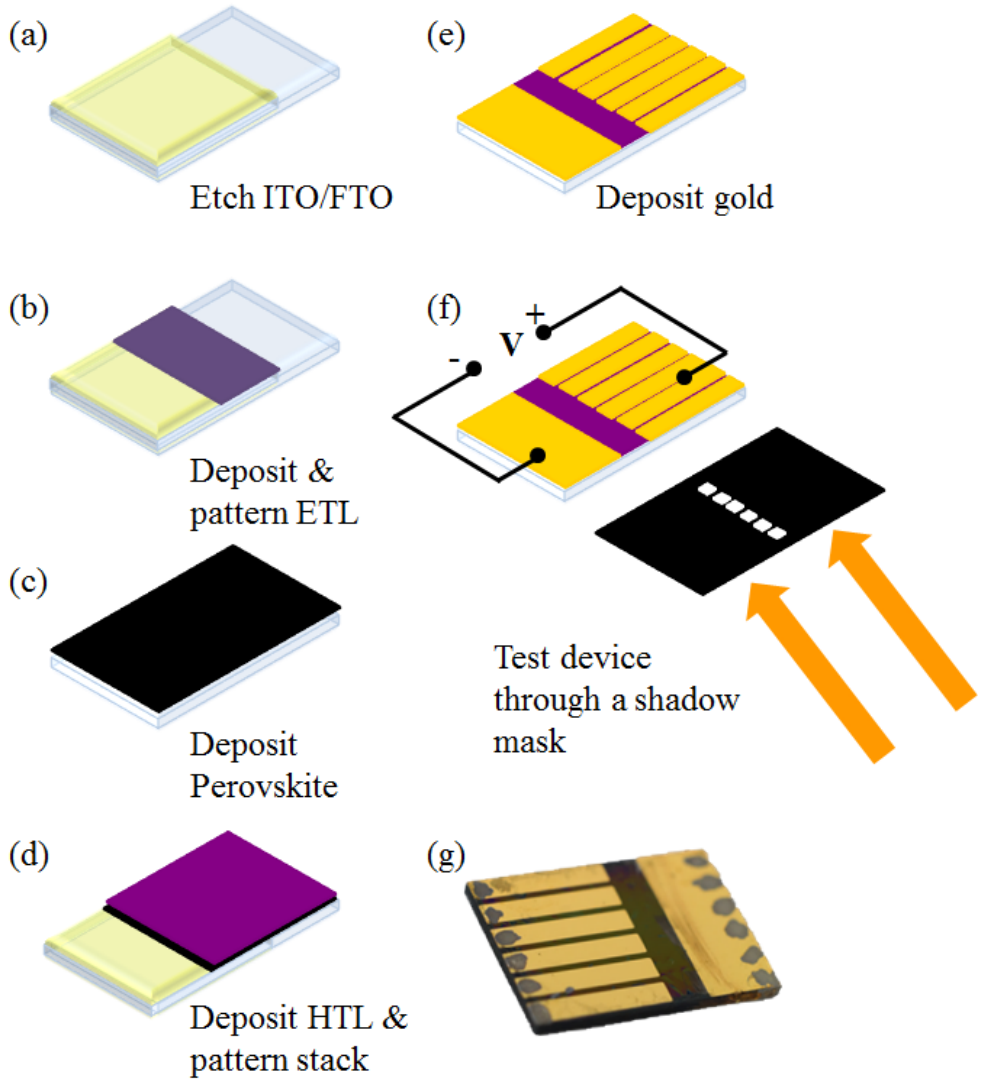

Figure 4: *Summary of device fabrication and testing. (a) ITO/FTO substrates are chemically etched and cleaned. (b) The electron transport layer is deposited and patterned. (c) The perovskite absorber layer is deposited. (d) The HTL is deposited and the stack is patterned to expose the ITO/FTO. (e) Gold is thermally evaporated to create 6 "pixels." (f) The device is tested under illumination through a shadow mask from a solar simulator. (g) Photograph of completed device.*

After removing the Kapton tape, the substrates are then cleaned by sonication in soapy water, de-ionised water, and the isopropanol for 10 minutes each. The samples are then dried using a nitrogen gun and treated via UV ozone to remove any organic contaminants on the surface. This cleaning stage is an important one as any dust/residue on the substrates can create defects in the subsequent layers.[7]

4.4.2: Electron Transport Layer

Within this thesis two ETLs are used; namely TiO_2 and SnO_2. Titanium oxide was deposited via spray-pyrolysis of titanium diisopropoxide bis(acetylacetonate) (TAA) which had been diluted in ethanol. During spray-pyrolysis the cleaned FTO was heated to 450 °C before being repeatedly coated with precursor solution, with a 30 s wait time between passes. As ITO degrades at this temperature FTO must be used instead. The high temperature vaporises the solution on contact, and the organic titanate is broken down allowing oxygen in the ambient environment to bond with the titanium ions. A mask was used to pattern the resulting layer of TiO_2 limiting its formation to the central region of the substrate.[8] A layer of mesoporous TiO_2 was then deposited by either spin or spray coating from a commercially available paste diluted in ethanol before being sintered at 450 °C for at least 45 minutes.

Alternatively to form SnO_2 a commercially available solution[9] was simply diluted in de-ionised water and either spin or spray-coated in air. The resulting film was then swabbed with a cotton bud soaked in water to pattern the layer before being sintered at 150 °C. The film was then UV oxone treated again for 15 minutes to improve the wetting of the perovskite layer. As the tin oxide layer formed is very thin (≈10 nm) ITO is preferable due to its lower roughness than FTO.

4.4.3: Perovskite

The deposition of high quality perovskite layers is the main focus of this thesis and as such is discussed in great detail in Chapters 5-7. As such only an overview is presented here to give more context to layer chapters. Before any deposition can be performed the perovskite precursor solution must be made. This involves first calculating the quantity of powder required to form the desired perovskite composition, before weighing the powders into a vial using a microbalance. Whilst all weighing was performed in air, the powders themselves were stored under nitrogen to minimise water absorption.

Next, the powders were taken into a glovebox and dissolved in anhydrous dimethylformamide (DMF) or a mixture of DMF and dimethyl sulfoxide (DMSO)

using a micropipette to measure out the solvent. The dissolution of the powder could be accelerated by heating to 70 °C for around half an hour, or by the addition of a small quantity of hydroiodic acid.

The solution was either spin or spray coated onto the substrate and then heated to 100-120 °C for up to 45 minutes to convert the precursor film into the perovskite phase. This can be performed in air but the best results are achieved in a nitrogen glovebox. A low vacuum was also been employed as a post deposition treatment prior to heating to improve film quality (see Chapters 6-7).

4.4.4: Hole Transport Layer

All devices fabricated in this thesis rely on spiro-OMeTAD as a hole transport layer. To prepare a solution, spiro-OMeTAD, Li-TFSI, and FK209 powders were weighed out into separate vials. Next the three powders are dissolved using chlorobenzene (spiro-OMeTAD) and acetonitrile (Li-TFSI and FK209). The dopants are then added to the spiro-OMeTAD solution along with the TBP (which is already in a liquid state) and well mixed. The solution can then be spin coated either in air or under nitrogen. For spray-deposition the solution is diluted with chloroform before being sprayed in air.

After the spiro-OMeTAD layer has been deposited it must ideally be left overnight in dry air to oxidise further, which improves its conductivity.[10] Prior to the gold deposition the spiro-OMeTAD and perovskite layers must be mechanically scribed to expose the ITO/FTO below.

4.4.5: Gold Cathode

The patterned samples are then placed in mask that defines six “pixels” and a busbar which will reduce the series resistance of the completed device upon testing. Gold is then thermally evaporated through the mask to a minimum thickness of 80 nm which completes the device.

4.5: Device Characterisation

4.5.1: Current-Voltage Measurements

Completed devices are immediately tested under AM 1.5 illumination from a Newport 92251A-1000 Solar Simulator which had been calibrated to 1000 Wm^{-2} using a silicon reference cell. Standard six pixel devices are illuminated through a shadow mask that defines a 2.6 mm^2 active area. Current-Voltage sweeps were performed using a Keithley 237 source measure unit. Standard testing protocol is to scan from -0.2 V to 1.2 V and then back to -0.2 V at a speed of 0.4 Vs^{-1}, which produces performance metrics for the forward and reverse scans. Selected devices were then held at a constant voltage close to the maximum power point for at least one minute to calculate their stabilised power output. It is common for unencapsulated devices to improve after a few days left in dry air as the spiro-OMeTAD layer oxidises further.

4.5.2: External Quantum Efficiency

External quantum efficiency (EQE) for perovskite solar cells was calculated using a custom setup (Figure 5a). Monochromatic illumination was produced from while light (L.O.T.-Oriel GmbH & Co, 10 – 150 W halogen lamp) passed through a monchromator (Spectral Products, DK 240) which was then focused onto either the sample or a silicon reference photodiode. The photodiode and the sample were mounted on a moving stage and connected to a source measure unit. By comparing the photocurrent generated from the photodiode with that from the sample, an EQE spectrum could be generated. In order to avoid second order diffraction effects two separate spectra were produced and stitched together. By combining the AM 1.5 and the EQE spectra an estimate of the J_{SC} of the device could be calculated.

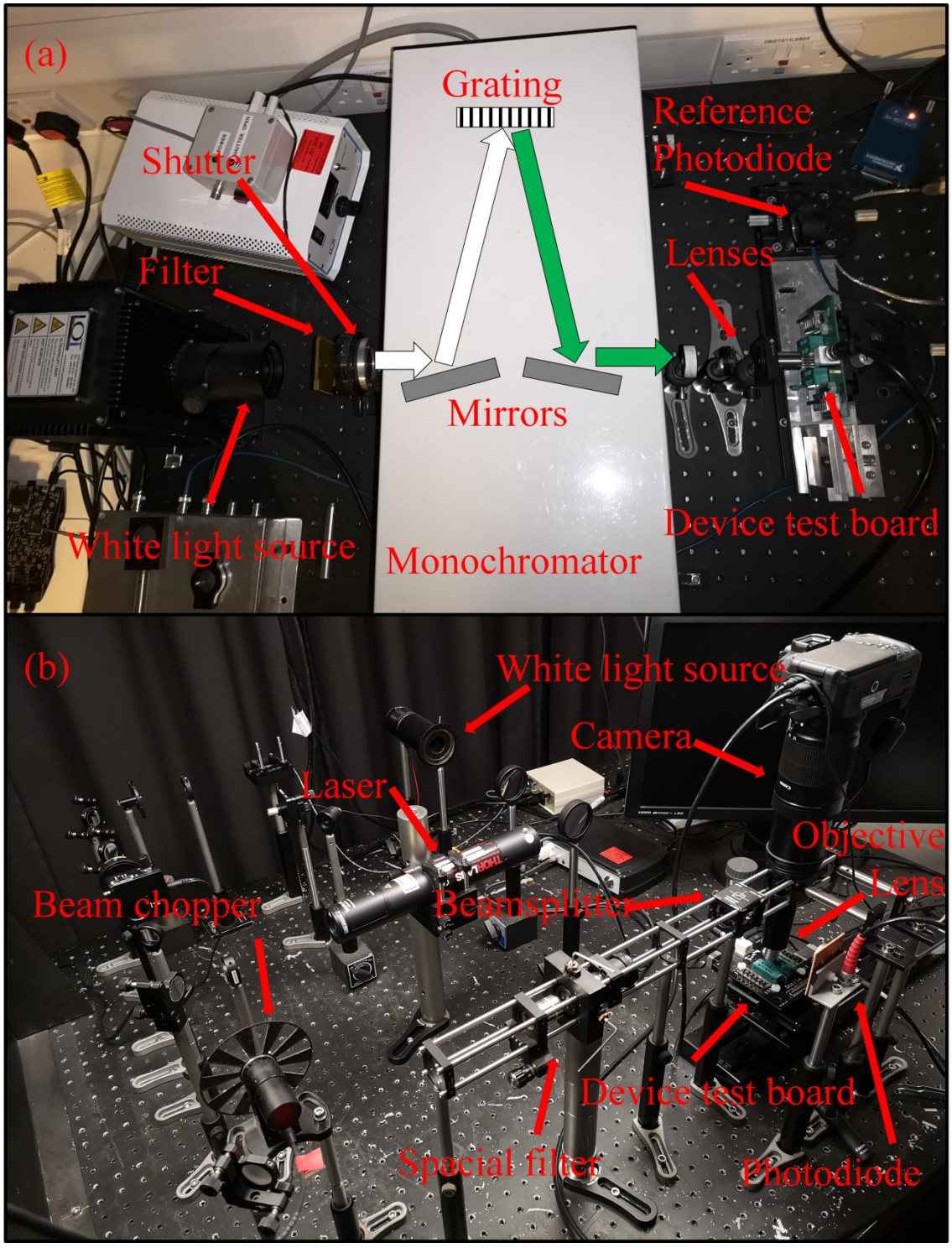

Figure 5: *Labelled photographs of external quantum efficiency (a) and laser-beam-induced-current mapping systems (b).*

4.5.3: Laser-Beam-Induced Current Mapping

Laser-beam-induced current mapping (LBIC) is an important technique used repeatedly within this thesis as it allows direct correlation between device morphology and performance. This is particularly important within the context of spray-deposition as achieving high uniformity is an important goal.

LBIC was performed using a custom setup which is shown in Figure 5b. Light from either a 405 nm, 635 nm (Thor labs, CPS635) or a 632 nm laser (Thor labs, HRS015B) was illuminated through a chopper before passing through a spacial filter to collimate the beam. The beam then passes through a beam splitter, with a fraction sent to a photodiode to measure any fluctuations in the laser power. The remainder of the beam is then focused onto the device via an objective lens. The device is mounted on a motorised test board which allows the laser spot to be scanned across the device in a sawtooth pattern. The photocurrent produced by the device was measured by a lock in amplifier (Stanford Research Systems SR830) which monitored the reference frequency of the beam chopper. In Chapter 5 the photocurrent was instead measured directly by a Keithley 2400 source measure unit.

In order to align the laser spot, a white light source was illuminated onto the sample through the objective lens, with a camera used to image the surface of the device. Once the desired area of the device is located and the laser focused, the white light source was removed and a computer program used to move the stages between photocurrent measurements. The area measured and the step sizes could be varied from measurement to measurement, but a typical area would be a few square millimetres which would take around 12 hours.

4.5.4: Dektak Surface Profilometry

A Bruker Dektak surface profilometer was used to characterise thin films. Here a stylus is scanned in a line across the surface of a sample with a fixed force applied to it (normally 3 mg). By measuring the magnitude of the restoring force on the stylus, a line profile for the surface is produced. This measurement allows an estimate for the roughness of the film to be characterised. Furthermore by

scratching a trench through the film and scanning over it an estimate for the film thickness can be obtained. The Dektak can also produce 2D surface maps by recording a series of adjacent line scans. This allows square millimetres of a film to be profiled allowing the surface uniformity of a film or indeed a PSC to be characterised.

4.5.5: Scanning Electron Microscopy

Electron microscopy utilises accelerated electrons rather than photons of visible light to produce high resolution images. In scanning electron microscopy, an electron beam is focused by a series of electromagnets and raster scanned across the surface. The incoming beam excites secondary electrons from the surface of the sample which are registered by a detector to produce the image. The entire setup is held at a low vacuum during measurement to prevent the electron beam scattering off gas molecules. Details of equipment and settings during use are provided in Chapters 5-7.

Scanning electron microscopy (SEM) is used many times in this thesis to characterise the surface morphology of perovskite films at the nanometre scale. SEM is also repeatedly used to produce cross-sections of completed devices by taking a cleaved PSC and imaging the individual layers. This allows a useful comparison between spin and spray-coated films to be made.

4.6: References

[1] D. O. Scanlon, C. W. Dunnill, J. Buckeridge, S. A. Shevlin, A. J. Logsdail, S. M. Woodley, C. R. A. Catlow, M. J. Powell, R. G. Palgrave, I. P. Parkin, G. W. Watson, T. W. Keal, P. Sherwood, A. Walsh, A. A. Sokol, *Nat. Mater.* **2013**, *12*, 798.

[2] J. P. Correa Baena, L. Steier, W. Tress, M. Saliba, S. Neutzner, T. Matsui, F. Giordano, T. J. Jacobsson, A. R. Srimath Kandada, S. M. Zakeeruddin, A. Petrozza, A. Abate, M. K. Nazeeruddin, M. Grätzel, A. Hagfeldt, *Energy Environ. Sci.* **2015**, *8*, 2928.

[3] P. Schulz, E. Edri, S. Kirmayer, G. Hodes, D. Cahen, A. Kahn, *Energy Environ. Sci.* **2014**, *7*, 1377.

[4] M. Deepa, M. Salado, L. Calio, S. Kazim, S. M. Shivaprasad, S. Ahmad, *Phys. Chem. Chem. Phys.* **2017**, *19*, 4069.

[5] S. Ameen, M. A. Rub, S. A. Kosa, K. A. Alamry, M. S. Akhtar, H. S. Shin, H. K. Seo, A. M. Asiri, M. K. Nazeeruddin, *ChemSusChem* **2016**, *9*, 10.

[6] Ossila, "Spin Coating: A Guide to Theory and Techniques," https://www.ossila.com/pages/spin-coating

[7] M. Saliba, J. P. Correa-Baena, C. M. Wolff, M. Stolterfoht, N. Phung, S. Albrecht, D. Neher, A. Abate, *Chem. Mater.* **2018**, *30*, 4193.

[8] L. Kavan, M. Grätzel, *Electrochim. Acta* **1995**, *40*, 643.

[9] Q. Jiang, L. Zhang, H. Wang, X. Yang, J. Meng, H. Liu, Z. Yin, J. Wu, X. Zhang, J. You, *Nat. Energy* **2016**, *2*, 16177.

[10] S. Fantacci, F. De Angelis, M. K. Nazeeruddin, M. Grätzel, *J. Phys. Chem. C* **2011**, *115*, 23126.

Chapter 5

Volume 7, Issue 1

2017/08/11

7962

SCIENTIFIC REPORTS

Spray-cast multilayer perovskite solar cells with an active-area of 1.5 cm^2

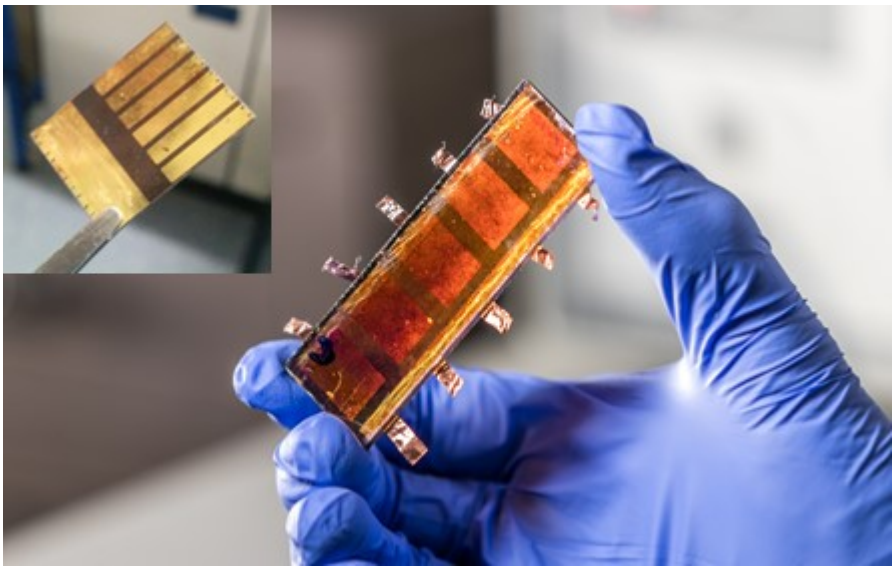

For the journals PDF:

DOI: 10.1038/s41598-017-08642-2 1

5.1: Publication Forward

By the end of 2016 several groups had been able to demonstrate high performance devices containing a spray-coated perovskite layer. However at the time nobody had attempted to extend this approach to the deposition of the other solution processed layers within a perovskite device, mainly the ETL and HTL. In this chapter a fabrication process to deposit all the layers in a normal architecture perovskite solar cell is developed; namely the compact TiO_2, mesoporous TiO_2, perovskite, and Spiro-OMeTAD. As of the writing of this thesis this paper has been cited 30 times.

5.2: Publication Main Body

Spray-cast multilayer perovskite solar cells with an active-area of 1.5 cm^2

James E. Bishop[1] and David K. Mohamad,[1] Michael Wong-Stringer,[1] Alex Smith[2] and David G. Lidzey[1]*

1) Department of Physics & Astronomy, University of Sheffield, Hicks Building, Hounsfield Road, Sheffield, S3 7RH, U.K.

2) CREST, Wolfson School, Loughborough University, Loughborough, Leicestershire, LE11 3TU U.K.

*Corresponding author, email d.g.lidzey@sheffield.ac.uk

Abstract

We utilise spray-coating under ambient conditions to sequentially deposit compact-TiO_2, mesoporous-TiO_2, $CH_3NH_3PbI_{(3-x)}Cl_x$ perovskite and doped spiro-OMeTAD layers, creating a mesoporous standard architecture perovskite solar cell (PSC). The devices created had an average power conversion efficiency (PCE) of 9.2% and a peak PCE of 10.2%; values that compare favourably with control-devices fabricated by spin-casting that had an average efficiency of 11.4%. We show that our process can be used to create devices having an active-area of 1.5 cm^2 having an independently verified efficiency of 6.6%. This work demonstrates the versatility of spray-coating as well as its potential as a method of manufacturing low-cost, large-area, efficient perovskite devices.

Introduction

Within the last seven years, devices based on perovskite absorbers have emerged as a leading thin-film photovoltaic (PV) technology, having power conversion efficiencies (PCEs) rising from 3.8%[1] to over 20%.[2] Perovskites combine the semiconducting properties typically associated with inorganic photovoltaics, such as strong light absorption,[3,4] high charge-carrier mobility,[4,5] tuneable bandgap[6,7] and low recombination rates[8,9] with ease of processing from solution. As a result perovskite based photovoltaics are predicted to have a shorter energy payback time than current commercial technologies of less than half a year.[10]

Spin-coating remains the principal method for thin-film preparation in high performance perovskite solar cells (PSCs).[11] Whilst this method is capable of delivering films of well-defined thickness and high uniformity, it is inherently unsuitable for large-scale PSC manufacture. If PSCs are to fulfil their promise as a low-cost, high-volume source of sustainable energy, their deposition must be achieved using truly scalable techniques.[12] This is a growing area of research, with perovskite materials now being deposited by ink-jet printing,[13] slot-die coating,[14] doctor-blading,[15] and spray-coating.[16–19]

Spray-coating is a versatile coating technique that is widely employed in industry. It can be used to deposit functional films at high coating-rates, over large

areas[20,21] with high material utilisation.[22] It also has the ability to apply conformal coatings to irregular surfaces.[23,24] Spray-coating has already been applied to the fabrication of standard architecture planar PSCs *via* single-step spray-deposition of $MAPbI_{3-x}Cl_x$[19] and $MAPbI_3$[25] reaching a PCE of up to 13%. By introducing $PbAc_2$ into the precursor ink, Tait *et al*.[17] demonstrated that such devices could reach a PCE of 15.7% though the development of a dense, highly uniform perovskite crystal lattice. Comparable device performance has been demonstrated by Huang *et al*.[18] through the development of a two-step spray-cast $MAPbI_3$ perovskite deposition protocol in which a thin-film of PbI_2 was first spray-cast onto mesoporous TiO_2. Onto this was spray-cast a film of methyl-ammonium iodide (MAI), with a perovskite film created via thermal annealing. Using this technique PSCs having an active-area 1 cm^2 were created having a PCE of 13%. Mesoscopic PSCs based on spray-deposited TiO_2 scaffolds have also been demonstrated[26]. However, comparably few examples of spray-coated inverted architecture PSCs exist.[16,27]

To develop a practical manufacture process to fabricate large-area perovskite PV, it is imperative that all layers within the device should be deposited via a scalable technique (ideally on a flexible substrate making it compatible roll to roll processing). However, this has only been demonstrated in a few cases, with most studies using inflexible glass substrates. One study of note fabricated devices in which all layers were deposited by doctor-blading (excluding the vacuum-processed back contacts) having an average PCE of over 10%.[28] This value was however reduced to 3.4% when the electrode was instead printed.[14] Recently, we reported on spray-coated planar inverted architecture PSCs where all solution-processed layers (namely PEDOT:PSS, perovskite and PCBM) were deposited by ultrasonic spray-coating, with an champion (average) PCE of 9.9% (7.1%) achieved.[27]

In this paper we extend our previous techniques, and use spray-coating to prepare all the layers in a mesoporous standard-architecture PSCs (except the contact electrodes), and create devices having improved performance and repeatability. Specifically, we spray-cast compact titania ($cTiO_2$),[29–31] mesoporous titania ($mTiO_2$),[32] a $CH_3NH_3PbI_{(3-x)}Cl_x$ precursor and doped spiro-OMeTAD layers,

creating a champion cell having a PCE of 10%. We then utilise a range of microscopy and mapping techniques to explore the homogeneity and uniformity of the layers, and conclude that device efficiency is partially limited by (i) the presence of ~ 10 μm diameter aggregate defects in the spray-cast perovskite layer that act as local current shunts, and (ii) non-uniformities in the spiro-OMeTAD film that results in reduced charge carrier extraction and thus reduced fill-factor. We also explore our techniques to fabricate devices having an active-area of 1.5 cm^2, reaching an efficiency of 6.6%. As far as we are aware, this is the first example of ultrasonic spray-coating being used to deposit a doped spiro-OMeTAD hole-transport layer, as well as the first example of a multilayer spray-cast mesoporous PSC.

Ultrasonic Spray-Coating

Spray-coating was carried out using a Prism ultrasonic spray-coating system supplied by Ultrasonic Systems, Inc. This instrument employs resonant oscillation of a piezo-electric tip to shear a coating ink into a fine mist of micron-sized droplets that are then directed to a surface of interest via a focused nitrogen gas jet.[22] Such "nozzle-less" techniques offer independent control of droplet formation and spray pattern. During the coating procedure, the spray-head is passed over the surface at a fixed height. From extensive optimization trials, we were able to adjust film thickness and drying rates *via* control of lateral head-speed, solution concentration and substrate surface temperature. Here, the formation of uniform thin-films is dependent on the ability of the ink to wet the surface. Unlike spin-coating, there are no lateral forces in a conventional spray-coater that act to spread a wet-film across a surface and ensure that droplets coalesce to form a continuous film. Instead, only capillary forces (which are relatively weaker) act to move liquid droplets across the substrate surface. This can lead to poor surface coverage, particularly if the solvent has a high surface tension or a low surface energy. The rate at which the film dries is also important; if the drying time is too short then the droplets can dry before forming a uniform wet film. Conversely if film drying occurs too slowly, then the wet film can undergo shrinkage[16,33] forming "coffee-ring" patterns.[34]

To address this, we have performed a detailed optimisation study in which we have developed a series of different ultra-sonic spray-coating processes and inks to deposit mesoporous TiO_2, a MAI:$PbCl_2$ precursor and a doped spiro-OMeTAD hole-extracting layer (see further details of ink formulations and deposition parameters in Table 1 in *Experimental Methods* section). For comparative purposes, the deposition of all layers was also explored by spin-casting. Small-area devices were fabricated on pre-patterned 15 x 20 mm glass-FTO substrates. The fabrication process commences with the deposition of a hole-blocking compact TiO_2 layer (cTiO2) by spray pyrolysis using a hand-held spray-gun. Here, TAA (titanium diisopropoxide bis(acetylacetonate)) was diluted in isopropanol and sprayed onto FTO-glass placed on a hot-plate and held at 450 °C[35] and then sintered for 1 hour. A mesoporous TiO_2 ($mTiO_2$) layer was then deposited at room temperature to act both as a scaffold for the perovskite layer and as an electron-accepting contact. Here, a $mTiO_2$ paste was used that was diluted to 10 wt% and 22 wt% with ethanol for spray- and spin-casting respectively. After the evaporation of the ethanol, the samples underwent further sintering for 1 hour at 450°C to harden the films into a dense $mTiO_2$ scaffold ready for perovskite precursor deposition.

The precursor perovskite films (2.95:1.00) MAI:$PbCl_2$ solution containing 1 % (by volume) hydrogen iodide (HI) in DMF were then coated on the FTO/$cTiO_2$/$mTiO_2$ surface under ambient lab conditions maintained at (20 ± 2) °C and (30 ± 5)% RH. Here, the role of the HI additive was to improve the solubility of $PbCl_2$ and increase the surface coverage of the final perovskite film.[36] This precursor was spray-cast using our previously-described methods used to fabricate inverted-architecture PSC devices.[16,27] Here the substrate is heated to 55 °C during deposition to replicate the drying dynamics that occur during spin-coating.[37] After deposition, the samples were transferred to a secondary hotplate held at 100°C for 45 minutes to convert the precursor film to a $MAPbI_{3-x}Cl_x$ perovskite.

Spiro-OMeTAD films were prepared by both spin- and spray-casting. For spray-casting, we developed a mixed solvent system (1:1 chlorobenzene:chloroform) to deposit doped spiro-OMeTAD. This exploited solvent surface tension gradient induced flows (Marangoni effect) to produce favourable spreading

capabilities,[38,39] resulting in the formation of a relatively smooth film. It was found however that the addition of dopants (Li-TFSI, TBP, and FK209) to the spiro-OMeTAD solution (conventionally used to increase the conductivity of the final film) had the unwanted effect of increasing ink surface tension which suppressed its wetting and spreading properties (see *Supplementary Information*). To address this issue, we found that the addition of a small quantity (0.003 mg mL^{-1}) of a high molecular weight (M_N ~ 8 MDa) polyethylene glycol polymer (PEG) to the ink increased its viscosity through chain entanglement effects.[40] Using this formulation, we were able to deposit films having improved uniformity (*see* Figure S1).

Finally, to create a PSC device, patterned gold counter electrodes were vacuum evaporated onto the Spiro-OMeTAD surface, creating six independent cells. Each cell had an active-area of 4 mm^2 whose size was defined by the overlap of anode and cathode stripes. In order to evaluate effects associated with scaling-up of our spray-deposition protocols, we used the same spray-casting methodology to create large-area PSC devices on 25 x 75mm FTO/glass slides. Here, five independent large-area PSCs were fabricated, with each device having an active-area of 1.51 cm^2. Images of completed all-spray-cast PSCs having an active-area of 4 mm^2 and 1.51 cm^2 are shown Figure 1.

Devices were characterized by measuring their J-V curves under 1 Sun AM1.5G simulated solar illumination (see *Experimental Methods*). Note that although six PSC devices were fabricated on each small-area substrate, the two devices at the edge of the substrate were omitted from our analysis due to defects associated with film formation at this location. We have also used laser-beam induced imaging (LBIC) to explore the homogeneity of photocurrent generation. In this technique, 405 nm light from a diode-laser was focused to a point and raster scanned across the surface in 25 μm step-sizes, with the photocurrent recorded using a pico-ammeter. Scanning profilometry using a Bruker DektakXT having a vertical and lateral spatial resolution estimated to be 1 nm and 12.5 μm (defined by the tip radius) respectively were also used to obtain topographic images of the surfaces of individual layers at various stages in the device fabrication process.

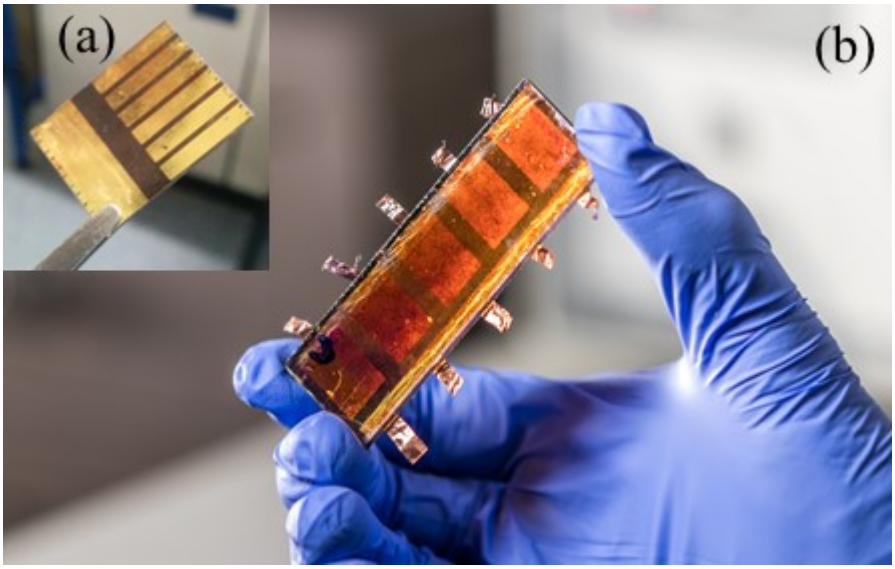

Figure 1: *Part (a) and (b) show images of completed small-area and large-area PSC devices respectively.*

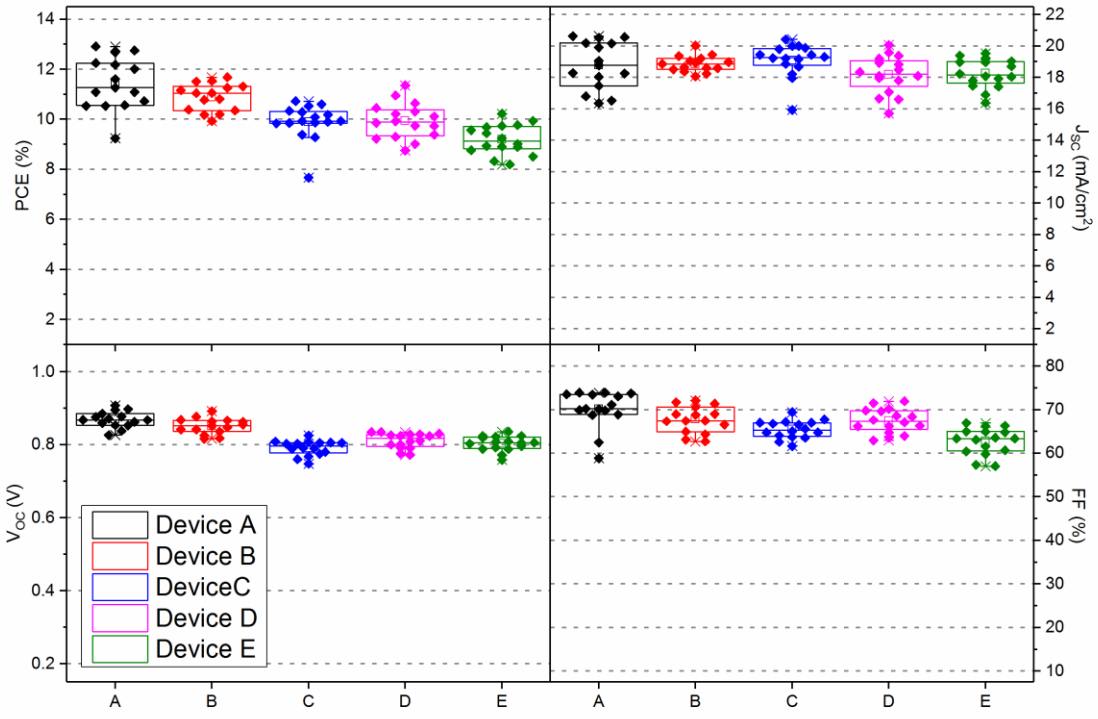

Figure 2: *Box plots showing statistical data of PSC performance from devices A-E (see Table 2 for a description of device labels).*

Parameter	$mTiO_2$		Perovskite		Doped Spiro-OMeTAD	
	spin	**spray**	**spin**	**spray**	**spin**	**spray**
*substrate temperature**	Ambient	Ambient	Ambient	55 ºC	Ambient	40 ºC
annealing	1hr min @ 450 ºC	1hr min @ 450 ºC	45 minutes @ 100 ºC	45 minutes @ 100 ºC	none	None
speed	3000rpm/30 s	60 mm s^{-1}	2000rpm/30s	200 mm s^{-1}	2000rpm/30s	150 mm s^{-1}
ink conc	22 wt%	10 wt%	630 mg ml^{-1}	450 mg ml^{-1}	96 mg ml^{-1}	45 mg ml^{-1}
solvent	Ethanol	Ethanol	DMF	DMF	CB	1:1 CF:CB
ink temp.	Ambient	Ambient	Ambient	Ambient	Ambient	Ambient

Table 1: *Summary of thin-film deposition protocols (*) refers to substrate temperature during ink deposition.*

	Device A	Device B	Device C	Device D	Device E	Device E
Area (cm^2)	0.026	0.026	0.026	0.026	0.026	1.008
$mTiO_2$	Spin	Spray	Spin	Spray	Spray	Spray
Perovskite	Spin	Spin	Spray	Spray	Spray	Spray
HTM	Spin	Spin	Spin	Spin	Spray	Spray
PCE (%)	**12.9** (11.4±1.0)	**11.7** (10.9±0.5)	**10.7** (9.9±0.7)	**11.4** (9.9±0.7)	**10.2** (9.2±0.6)	**6.9**
J_{SC}(mA/cm^2)	**20.6** (18.8±1.5)	**20.0** (18.9±0.5)	**20.4** (19.1±1.0)	**20.1** (18.2±1.2)	**19.5** (18.2±0.9)	**18.6**
V_{oc} (V)	**0.91** (0.87±0.02)	**0.89** (0.85±0.02)	**0.82** (0.79±0.02)	**0.83** (0.81±0.02)	**0.84** (0.80±0.02)	**0.83**
FF (%)	**74** (70±4)	**72** (68±3)	**69** (65±2)	**72** (67±3)	**67** (63±3)	**45**

Table 2: *A summary of PSC performance metrics and deposition technique used to fabricate each layer. Bold is the peak value with the average and standard deviation presented in parenthesis.*

Device and Film Characterisation

We first present a summary of performance metrics from our small-area device fabrication study in Table 2, together with statistical data recorded from 16 independent cells in a box plot in Figure 2. Here, device A was fabricated by spin-coating all layers and had a PCE of (11.4 ± 1.0)%. On spray-casting the $mTiO_2$ scaffold (device B), we find that the PCE is slightly reduced at (10.9 ± 0.5)%, however the statistical significance of this reduction is low. Here, any reduction in average PCE results from a drop in V_{OC} from (0.87 ± 0.02) V to (0.85 ± 0.02) V, and in FF from (70 ± 4)% to (68 ± 3)%. Such differences appear to result from changes in the $mTiO_2$ thickness that appears dependent on the nature of the technique used

in its deposition. This is illustrated in Figures 3(a) and (b) respectively, where we plot topographic images of spin and spray-cast $mTiO_2$ thin-films after sintering. Interestingly, we find that the spin-cast film shows strong evidence of solutal Marangoni effects[41,42] whereby surface tension gradients cause a flow of the material to highly concentrated areas. Such effects area characterised by striations[43] in film thickness that appear as periodic features (70 ± 1)μm in the cross-sectional thickness data (*see* Figure 3(b) inset). This results in much larger peak-to-valley thickness variations in the spin-cast film surface compared with its spray-cast analogue (90 nm compared with 20 nm respectively). Because of this, one might anticipate superior performance from device B owing to its improved $mTiO_2$ uniformity, however this is not observed. We are unable to account for the reduction in fill factor responsible for this; however we note that the efficiency of mesoporous standard architecture PSCs is very sensitive to differences in $mTiO_2$ film thickness, and the efficiency variations may simply reflect uncertainties associated with film thickness and measurement.

We now turn our attention to the perovskite absorber layer. Here, we find that there is a reduction in efficiency associated with spray-casting this layer in particular. Returning to Table 2, we compare devices A and C in which the perovskite precursor layer was either spin- or spray cast (with all other layers being spin-cast). Here, we find a significant reduction in PCE from (11.4 ± 1.0)% to (9.9 ± 0.7)% as a result of spray-casting the perovskite layer. This effect is also evident when comparing devices B and D. Here, both devices employ spray-cast $mTiO_2$ and spin-cast spiro-OMeTAD layers, with the perovskite precursor layer being spin-cast in device B and spray-cast in device D. Here, we find a reduction in efficiency as a result of spray-casting, with efficiency dropping from (10.9 ± 0.5)% to (9.9 ± 0.7)%; an effect that is almost entirely accounted for by losses in V_{OC}.

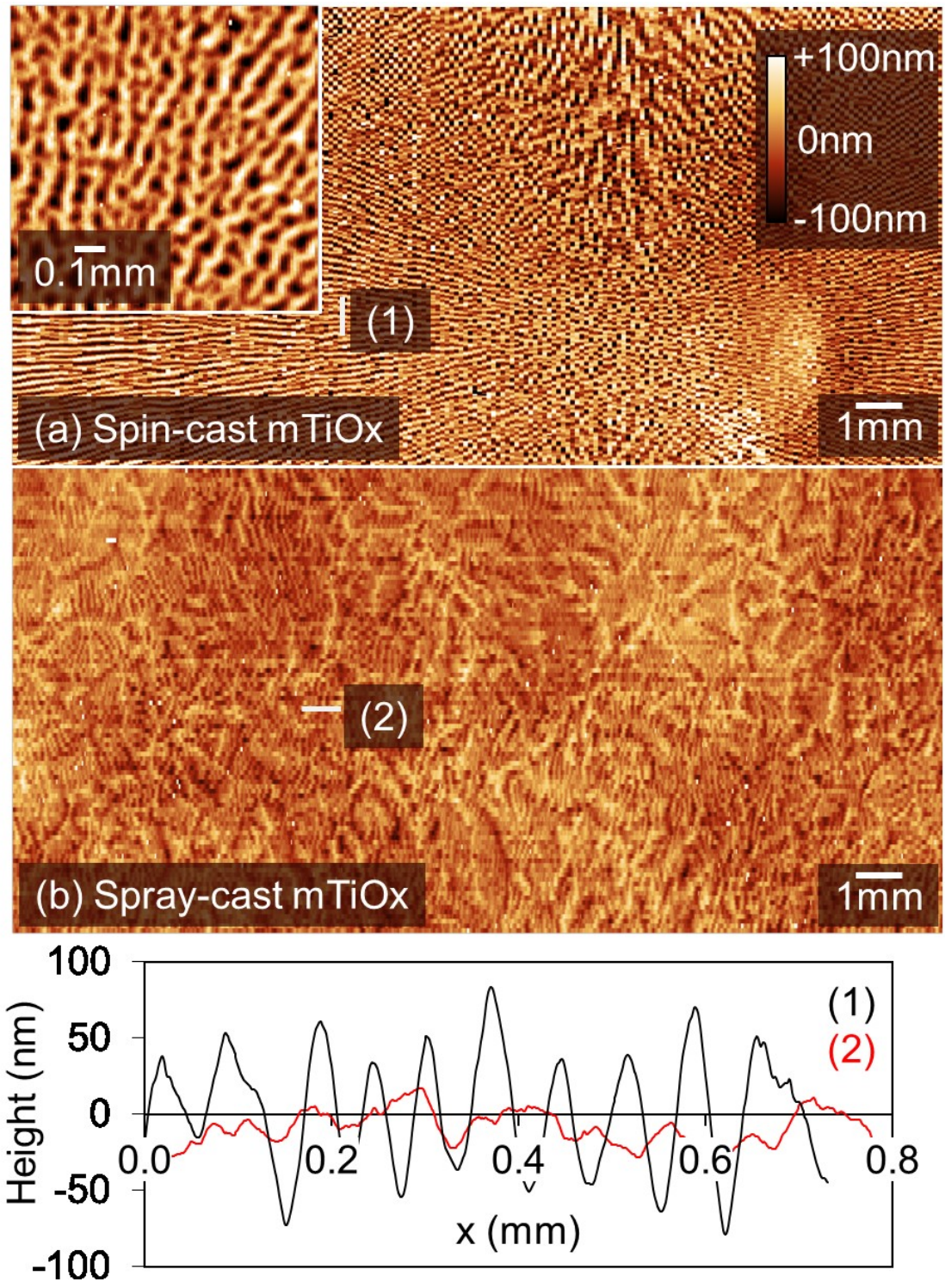

Figure 3: *Topographic images of mTiOx prepared on a glass/FTO/cTiOx surface. Part (a) shows a spin-cast film with a high-resolution map shown in the inset. Part (b) shows surface topography of a spray-cast film, with line profiles determined from sections labelled (1) and (2) plotted using black (spin-cast) and red (spray-cast) lines shown as an inset. All images are plotted on the same colour scale.*

Once again, we use surface profilometry to understand such effects. In Figure 4(a) to (e), we plot topographic images of devices A to E (image recorded over the surface of the gold anode and surrounding region). Here the active-area of each device can be recognised *via* the raised rectangular region that corresponds to the evaporated gold film, with dark region in the lower part of each image corresponding to the edge of the etched FTO. Faint striations consistent with the underlying spin-cast $mTiO_2$ topology are evident in device A [Figure 4(a)] and device C [Figure 4 (c)] as expected. It is also apparent that small raised features (defects) having a lateral diameter of 10 to 40 μm and height of up to 25 μm are observable in all images.

To characterise such defects, we threshold image data recorded from device A to D at 1 μm and perform a particle size analysis characterising both particle height and number density[44] (*see* Figure S2). From these plots and the images shown in Figure 4, it is apparent devices in which the perovskite precursor film is spray-cast are characterised by a greater density of defects (see Table 3). Note, that most defect particles imaged using the surface profiler had an apparent in-plane diameter of around 10 – 15 μm. This value however is coincident with the spatial resolution of the surface profiler, indicating that the diameter of many of the defects is likely to be smaller than this. To determine the typical size of such defects, we have used an optical microscope to image the surface of a spray-cast perovskite film, with a typical image shown in Figure S7. An analysis of such images suggests that the defect structures indeed have a diameter of around 10 μm.

	Device A	Device B	Device C	Device D
Defects per 1 cm^2	100	140	320	420
Height (μm)	2 (6)	4 (24)	2 (12)	3 (14)

Table 3: *Results of particle size analysis carried out on data from surface topographs shown in Figure 4 (a) to (d). Average values are shown outside and maximum values inside parentheses. Data was thresholded at 1μm and image area remained fixed at 13.5 mm^2.*

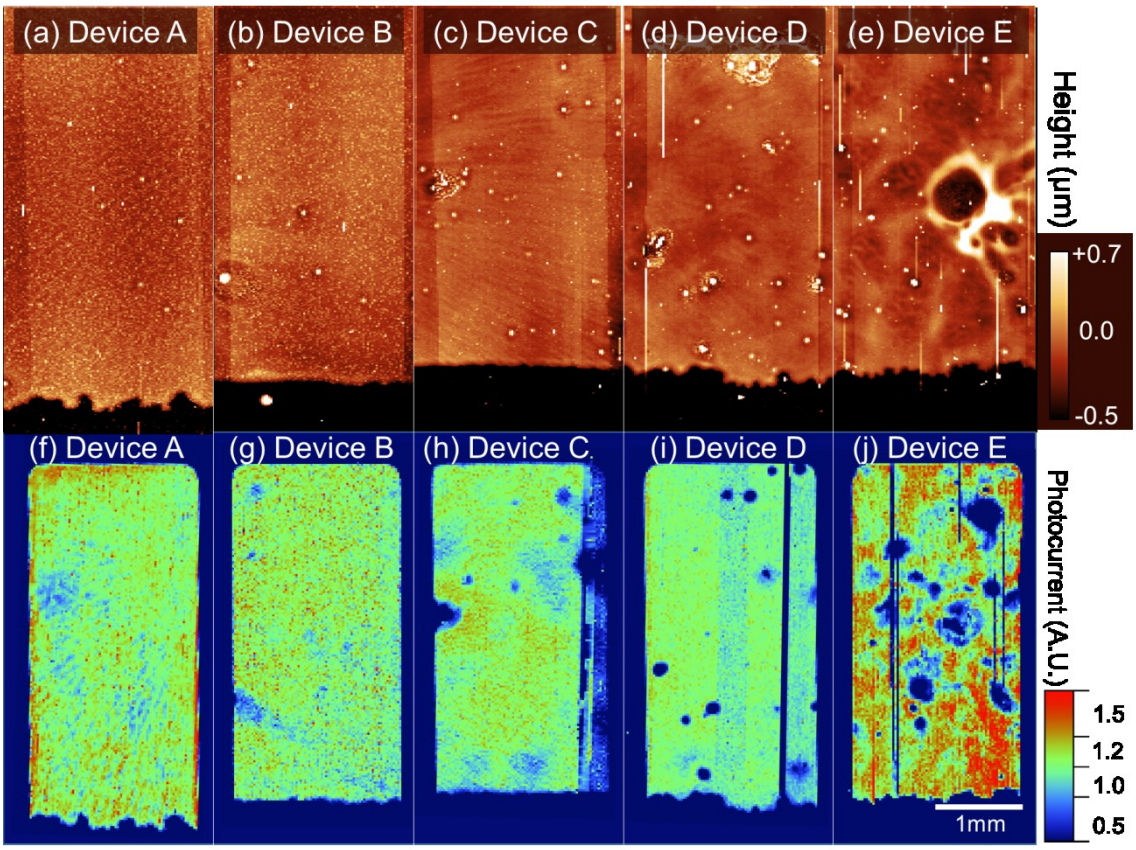

Figure 4: *Topographic images of device A-E (parts (a-e)) measured by scanning profilometry with colour and lateral scales shown inset in part (a) and (e) respectively. LBIC (laser beam induced current mapping) maps of Devices A to E shown in parts (f) to (j). The horizontal dashed lines correspond to the photocurrent sections plotted in parts (k) to (o). Data has been normalised to the average photocurrent and represented on the same colour scale. All images are plotted on the same lateral scale shown inset in part (j).*

To confirm that film defects seen in Figure 4 are associated with the perovskite film, we have studied FTO/cTiO_2/mTiO_2/perovskite surfaces prepared by spray-coating. In Figure 5(a) we show an optical image of the film recorded in transmission, with part (b) showing a topography map of a representative area of the film with both images plotted on the same scale. It can be seen that the optical image [Figure 5(a)] is characterised by a series of dark spots that are apparently consistent with aggregate-like defects that are visible as white-spots in the

representative topography map [*see* Figure 5(b)]. We plot a cross-section recorded through a single aggregate-defect in the Figure 5(c) where it can be seen that the height of such defects is indeed much greater than the thickness (and normal roughness) of the perovskite film. Notably, such defects are not observed in spin- or spray-cast $cTiO_2$ or $mTiO_2$ layers. An analysis of the height distribution of these aggregates [(*see* Figure 5(d)] indicates a distribution of particle sizes having an expectation value of 1.8 μm and variance of 3.2 μm.

At this point, we are unable to assign the origin of these defects, however we speculate that they are in fact $PbCl_2$ aggregates. We base this conclusion on the fact there is a large difference in relative solubility of $PbCl_2$ and MAI, and that $PbCl_2$ may undergo local aggregation or crystallisation during film drying as a result of fluctuations in local material concentration. It is unclear why larger aggregates apparently appear in the spray-cast films when their drying time is in fact shorter than the spin-cast analogues (15 *vs* 30 s respectively). We suspect that films that are spin-cast are subject to shear forces that constrain the film surface[45] and reduce any tendency for the creation of compositional concentration gradients that lead to the formation of aggregates. In spray-casting however, such shear forces are absent, with convective flows due to the heated substrate possibly driving lateral material flow across the surface[37] even though the overall drying time is shorter in the latter. We speculate therefore that such effects are responsible for the increased density of aggregates found in spray-cast films. Such aggregates in the perovskite film most likely result in charge-carrier leakage pathways through the top spiro-OMeTAD hole-transport layer that is (400 ± 10) nm thick in devices A-D. This leads to additional charge-carrier recombination losses that act to reduce V_{OC} and reduce device performance compared to their spin-cast analogues.

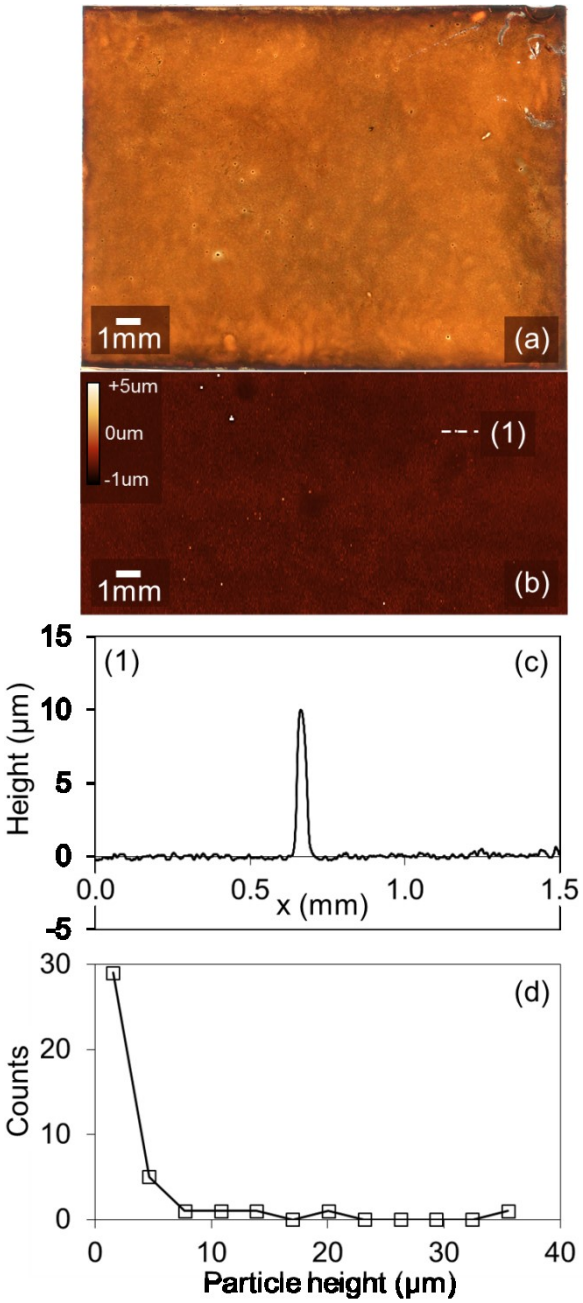

Figure 5: *Part (a) shows an optical transmission image of a FTO/cTiOx/mTiOx/perovskite film prepared by spray-coating. Part (b) shows a representative topographic image of the film shown in part (a), however these images do not correspond to the same location on the film surface. Part (c) shows a cross-section recorded through one of the aggregates (visible as white-spots) in part (b). The location at which this data was recorded is shown using a dotted line. Part (d) plots a histogram of particle height determined from an analysis of the film recorded over an area of 5 x 10 mm².*

Finally, we discuss the spray-deposition of spiro-OMeTAD. Here, we again saw a reduction in device performance on spray-casting this layer as shown in Table 2. We now compare device D and E in which TiO_2 and perovskite-precursor films were deposited by spray-casting, but spiro-OMeTAD films were spin and spray-cast respectively. It can be seen that on spray-casting, the device PCE reduces from (9.9 ± 0.7)% to (9.2 ± 0.6)% as a result of a reduction in FF from (67 ± 3)% to (63 ± 3)%. We ascribe this reduction to a general decrease in HTM layer uniformity; a process that leads to a concomitant increase in series resistance. Despite the reduction in efficiency resulting from spray-coating the perovskite-precursor and spiro-OMeTAD layers, it can be seen that device E in which all layers were spray-cast has an average PCE of (9.2 ± 0.6)%. This represents a marked enhancement in performance (with a narrowed spread in device performance) compared to our previous study on all-spray inverted PSCs[27] in which we obtained an average PCE of (7.1 ± 1.7)%. For completeness, we include EQE spectra recorded from champion all spin (A) and all spray (E) devices in Supplementary information Figure S6. The reduction in the homogeneity of devices incorporating a spray-cast spiro-OMeTAD film can be seen in Figure 4(e) (corresponding to device E) where large variations in height are evident. This is likely responsible for the reduced fill factor for these devices. Indeed, we found that the spray-deposition of doped spiro-OMeTAD to be very challenging, however highly uniform films of *undoped* spiro-OMeTAD could be prepared by spray-coating without apparent difficulty. We suspect that the presence of ionic dopants such as LiTFSI and FK209 may increase the surface tension of the spiro-OMeTAD ink and therefore adversely impact its wetting properties as a result of increased surface tension (*see* Figure S1(c)). This is likely to impede droplet coalescence and thus causes solution dewetting. However the uniformity of the doped spiro-OMeTAD film can be significantly improved through the addition of a PEG rheology modifier, which we found enhanced the performance of resultant PSC devices (*see* Figure S3).

Laser Beam Induced Current Mapping

To further characterise the uniformity of our PSCs and explore spray-cast film properties we have used Laser Beam Induced Current (LBIC) mapping. This powerful diagnostic technique can be used to create a spatial map of photocurrent homogeneity. This is shown in Figure 4 where we plot LBIC maps recorded from devices A to E (shown in parts (f) to (j) respectively). It is immediately apparent that the efficiency of photocurrent generation across devices A and B (corresponding to devices in which the perovskite-precursor is spin-cast), is highly uniform and only varies by around 8 % over length-scales of a few mm. Conversely, PSCs containing spray-cast perovskite precursors (devices C and D), are characterised by less uniform photocurrent generation, varying by 16 and 21 % respectively. Interestingly in device D, we observe isolated regions having a diameter of (110 ± 10)μm that are characterized by a low photocurrent. By comparing topographic and LBIC images (Figure 4 (a) to (e) and (f) to (j) respectively) we find that regions of low photocurrent closely correlate with the large aggregate-type defects associated with perovskite spray-deposition.

It is also apparent that there are periodic (radial) features visible in the LBIC images recorded from devices A and C that were also apparent in the topography images shown in Figure 4. We conclude therefore that the thickness variations in the $mTiO_2$ play a significant role in determining the efficiency of photocurrent generation, and that accurate control over this layer is of key importance for effective device optimisation. Notably such features are not observable in the LBIC images recorded from devices B and D due to the improved uniformity of the spray-cast $mTiO_2$ layer. The effect of the non-uniform spray-cast spiro-OMeTAD film on photocurrent generation in device E is clearly apparent in Figure 4(j), and in the photocurrent histogram and cross-sectional data (*see* Figure S4 & 5). Here, the photocurrent varies by as much as 22 % across the surface of the device, indicating the importance of developing improved processing protocols for this layer. For completeness, we also present cross-sectional SEM images recorded from devices A and E in Supplementary Information, Figure S8. This confirms the results presented in Figure 4, with enhanced non-uniformity across both the perovskite and spray-cast spiro-OMeTAD being evident.

Large-Area Device

In order to evaluate the scalability of our spray-casting deposition protocols, we have fabricated large-area cells on 25 x 75mm FTO/glass slides. Here, all solution processable layers were deposited via spray-coating using the techniques developed to fabricate device E. Again, the devices utilised a thermally evaporated gold contact to define five independent cells, each having an active-area of 1.51 cm^2 (as shown Figure 1(b)). To gain additional confidence in our device test protocols, we have also recorded *JV* characteristics of devices having an active-area of 1.51 cm^2 using a solar simulator at CREST, UK. These measurements (performed through a 1 cm^2 aperture mask) confirmed a device PCE of (6.59 ± 0.16)%; a value in good accord with measurements recorded using the solar simulator in Sheffield. A *JV* scan from the champion large/small-area devices with a corresponding stabilised PCE measurement is plotted in Figure 6 (for more JV data see S6). It is clear that J_{SC} and V_{OC} are largely unaffected by scale-up which demonstrates the robustness of our process. However there is a significant reduction in FF from 67 % to 45 % that leads to a loss in PCE associated with scale-up from 10.2% to 6.9%. This reduction in PCE results from parasitic losses as a result of increased series resistance associated with longer FTO channel lengths which tend to increase with the device area.[46]

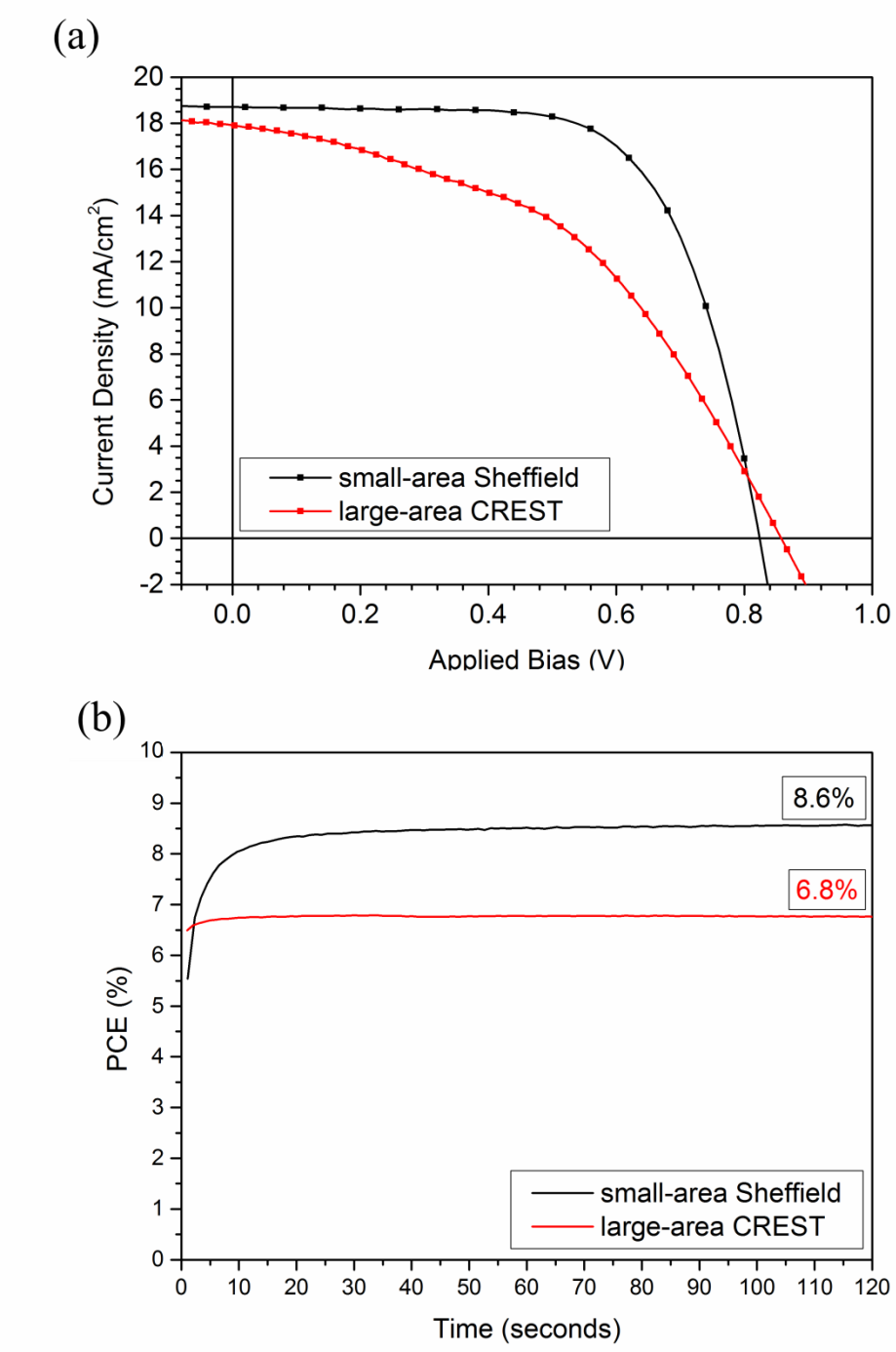

Figure 6: *Part (a) shows the champion reverse scan JV characteristics for the small-area (measured in Sheffield) and large-area devices (measured at CREST). Part (b) shows the stabilised PCE for the champion devices held at a fixed voltage around the maximum power point.*

Discussion

We have developed a method to fabricate multilayer standard architecture perovskite solar cells in which all solution processible layers ($cTiO_2$, $mTiO_2$, perovskite absorber and doped spiro-OMeTAD) were deposited by spray-casting. We show that this method can be used to fabricate cells with a peak PCE of over 10% and an average of 9.2%, with a relatively low distribution in cell performance (σ = 0.6). This result compares favourably with devices in which all layers were deposited by spin-casting, where devices had an average PCE of 11.4%. Note that the baseline efficiencies of spin-cast devices demonstrated here are around a factor of two lower than state of the art devices that are processed using different perovskite formulations in an inert water and oxygen-free environment. The reduced efficiencies reported here result from the fact that all processing steps here were performed in air; a condition that is likely to be beneficial when developing a low-cost industrial process. However we expect that higher efficiency devices will be possible by transferring our process to a spray-coater housed within a nitrogen filled glove-box. Using laser beam induced photocurrent mapping and optical microscopy, we attribute the reduction in performance associated with spray-casting (compared to spin-casting) to the presence of micron-sized defects in spray-cast perovskite films that reduce V_{OC} through charge-carrier recombination losses, and significant film-thickness fluctuations in the spray-cast spiro-OMeTAD films that reduce FF by series resistance losses. We also explore the suitability of this process to fabricate larger-area devices, and fabricate fully spray-cast cells having an active-area of 1.5 cm^2. These were characterised using a solar simulator at CREST, where a device PCE of (6.59 ± 0.16)% was determined. This reduction in PCE on scale-up resulted from parasitic losses caused by increased serial resistance of the FTO electrode.

Acknowledgments

This work was funded by the UK Engineering and Physical Sciences Research Council (EPSRC) via grants EP/M025020/1 ‘High resolution mapping of performance and degradation mechanisms in printable photovoltaic devices’ and EP/M014797/1 ‘Improved understanding, development and optimisation of

perovskite-based Solar cells'. We also thank the EPSRC for PhD studentships via the University of Sheffield DTG account (J.E.B.) and from the Centre for Doctoral Training in New and Sustainable PV, EP/L01551X/1 (M.W-S.), Jonathan Griffin (Ossila Ltd) for helpful insight regarding spiro-OMeTAD ink preparations, Tom Routledge for assistance in testing large-area devices and Samuele Lilliu for taking the photographs shown in Figure 1. We also thank Vikas Kumar for performing cross-sectional SEM (EP/N008065/1 and EP/M025020/1).

Author Contributions

J.E.B., M.W-S. and D.M. fabricated and tested devices. J.E.B. and D.M. performed EQE and surface profilometry measurements. D.M. performed LBIC measurements and analysis. A.S. independently tested a large-area device at CREST. D.G.L. contributed to the conception and design of the experiments, analysis of the data and writing of the manuscript in collaboration with J.E.B and D.M. All authors reviewed the manuscript.

Methods

Device Fabrication. Small- and large-area devices were fabricated on TEC 10 and TEC 8 FTO/glass substrates (XOP glass) respectively. Substrates were etched with zinc powder and 4 M HCl before being sonicated with Helmanex detergent solution, deionised water, and IPA. All device steps reported below were conducted under ambient lab conditions (in air) unless otherwise stated. All solvents used in this research were purchased from Sigma.

Substrates were first transferred to a hotplate where spray-pyrolysis was performed. 1.72 mL of titanium diisopropoxide bis(acetylacetonate) (Sigma 325252) was diluted with IPA to 20 mL. This was then sprayed onto the substrates held at 450°C *via* a handheld spray gun (Draper 09709) with a nitrogen feed at 30 psi. Substrates were coated every 30 seconds until all the precursor was used. These were then left to sinter for 30 minutes.

Spray coating was performed using an Ultrasonic Systems Inc. Prism 300 system. During coating, the ultra-sonic tip was positioned 60 mm above the substrate

surface and vibrated at 35 kHz while fluid from a coating reservoir was fed to the tip. This dispersed the ink into micron-sized droplets that were directed to the surface using a carrier gas whose pressure was set to 10 psi giving a wide spray pattern (*ca* 50 mm). During spraying, the spray head was scanned a lateral distance of 150 mm over the device substrates in a single pass. Note that the width of the spray-pattern was wider than the individual device substrates (25 mm), and thus significant heterogeneity across the spray-mist pattern at the sample surface is not anticipated. Between coating processes, pure solvent was flushed through the ink delivery system before the next ink reservoir was refilled. Substrates were mounted on a hotplate at elevated temperature in order to control the film drying-rate.

Mesoporous titanium oxide paste (18-NRT Dyesol) was diluted to 22 wt% in ethanol for spin-coating, and 10 wt% for spray-coating. The paste was spin coated at 3000 rpm. The spray parameters were as follows: fluid pressure 60 mbar, head velocity 60 mm s^{-1} and substrate temperature 22°C. After deposition, the substrates were sintered for 1 hour at 450°C.

Perovskite precursor ink was prepared using a stoichiometric ratio of 2.95:1.00 MAI (Ossila) to lead chloride (99.999%). Precursor inks were prepared at 630 mg ml^{-1} in DMF containing 1 v% hydroiodic acid. This precursor was the spin-coated at 2000 rpm to create thin films. For spray-coating the precursor ink was diluted with DMF to 450 mg/ml and deposited using the following parameters: fluid pressure 50 mbar, head velocity 200 mm s^{-1}, and substrate temperature 55°C. After deposition, substrates were annealed at 100°C for 45 minutes to convert them to a perovskite.

A stock Spiro-OMeTAD solution (Ossila) was prepared at a concentration of 96 mg mL^{-1} in chlorobenzene. This material was then doped by adding the following quantities of dopant to 1 mL of solution: 30 µl Li-TFSI (175 mg mL^{-1} in acetonitrile), 10 µl TBP, and 20 µl of FK-209 (175 mg mL^{-1} in acetonitrile). Films were then spin-cast onto the perovskite at 2000 rpm. For spray-coating, the doped solution was diluted to 45 mg mL^{-1} in chlorobenzene and chloroform such that the solvent ratio was 1:1. A small quantity of the polymer PEG (5 mg mL^{-1} in

chlorobenzene) was added such that the PEG concentration was 0.003 mg mL^{-1}. The spray parameters used to deposit the doped Spiro-OMeTAD solution were as follows: fluid pressure 20 mbar, head velocity 150 mm/s and substrate temperature of 40°C.

Finally an 80nm gold top contact was evaporated in an Edwards Auto 306 bell-jar evaporator at a pressure of *ca* 10^{-6} mbar.

Device characterisation. Devices were characterised by measuring their J-V curves under AM1.5 simulated solar irradiance. When testing a large- and small-area cells the illuminated area was defined through a shadow mask having an aperture of 1.0077 and 0.026 cm^2 respectively. Devices were tested under ambient conditions using a Newport 92251A-1000 solar simulator. An NREL certified silicon reference cell was used to calibrate the simulated AM1.5G light-output to 100 $mWcm^{-2}$. A Keithley 237 source measure unit was then used to perform J-V measurements. During testing devices were swept from -1.2 V to +1.2 V, and then back to -1.2V at a scan speed of 0.4 Vs^{-1}. Performance metrics were extracted from the reverse J-V scan. Stabilised power measurements were performed on the cells by holding them at a fixed voltage and recording the current over the course of a few minutes.

The champion large-area solar-cell was taken to CREST for testing using a WACOM solar simulator. Full details of this test as well as the test report are included in the supplementary information. EQE measurements were performed using a custom-built setup. Devices were illuminated with light from a 100W tungsten-halogen light source coupled to a monochromator (Spectral Products DK240 1/4m). The photocurrent was recorded with an Ossila Xtralien X100 source measure unit. The photocurrent from the device under test was compared to a reference silicon photodiode (Newport) with a known spectral response to calculate the EQE.

Dektak and LBIC measurements. Laser beam induced current (LBIC) maps were performed using a custom-built setup. A 3 mW 405 nm diode laser was passed through a spatial filter before being focused to a power density of 27 W cm^{-2}. The sample was mounted on a computer-controlled XY-stage and moved in a sawtooth pattern. To map the sample, the beam was focused ***via*** a 10X infinity-corrected

objective lens to a spot size of ***ca*** 10 µm and the stage was moved in 25 µm steps. The PSC photocurrent was collected using a Keithley 2400 source measure unit.

Surface topographs were measured with a Bruker Dektak:XT profilometer in map scan mode (12.5 µm tip radius, 3 mg stylus force) over an area of 2.7 x 5.0 mm^2 with 25 (slow-scan) and 0.83 µm (fast-scan axis) step-size respectively.

5.3: Supplementary Information

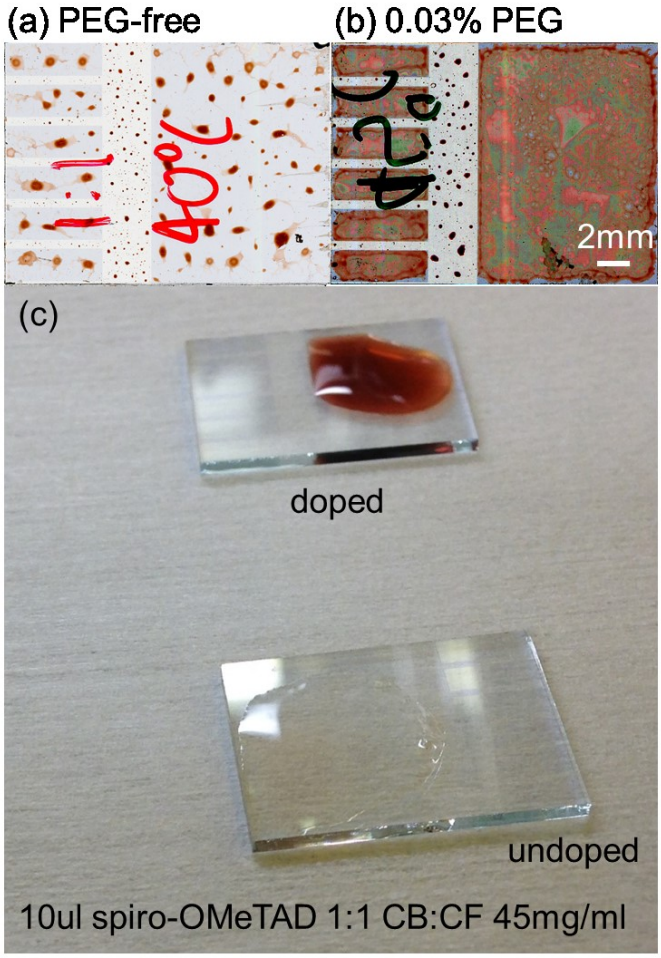

Figure S1: *Spray-coating spiro-OMeTAD ink onto an ITO/glass surface (a) without and (b) with 0.03 mg/mL PEG added to the ink. The increased contact angle can be seen in the image shown in part (c) when dopants are added to the ink.*

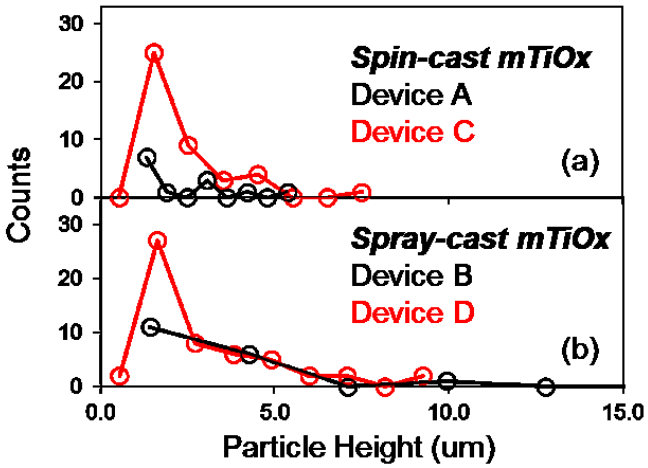

Figure S2: *The results of particle size analysis from topographic maps shown in Figure 4 are shown in parts (a) and (b): a particle height histogram from device A and C in shown in part (a) and device B and D in part (b).*

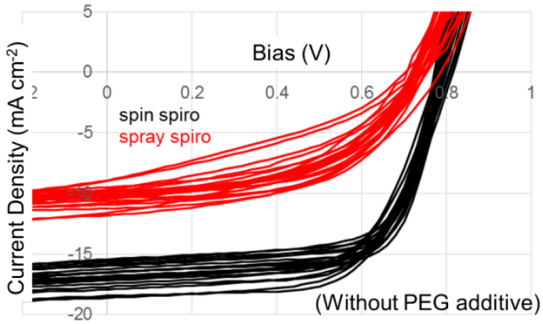

Figure S3: *Analogous spin-cast PSCs fabricated with spin-cast (black lines) and spray-cast (red lines) spiro-OMeTAD thin-films without the PEG additive.*

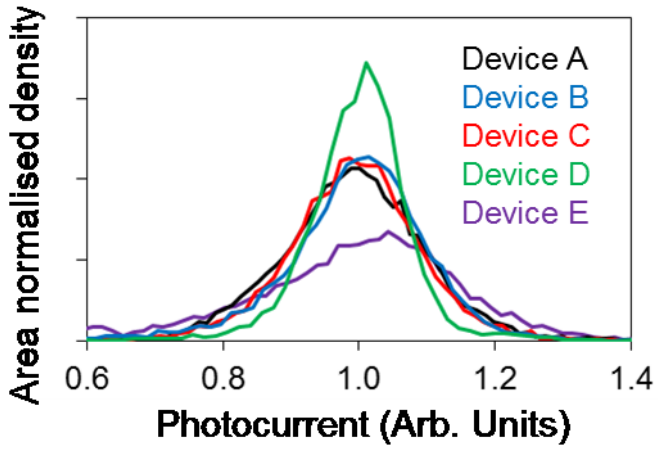

Figure S4: *Area normalised photocurrent histogram plotted from LBIC map data shown in Figure 4(f-j).*

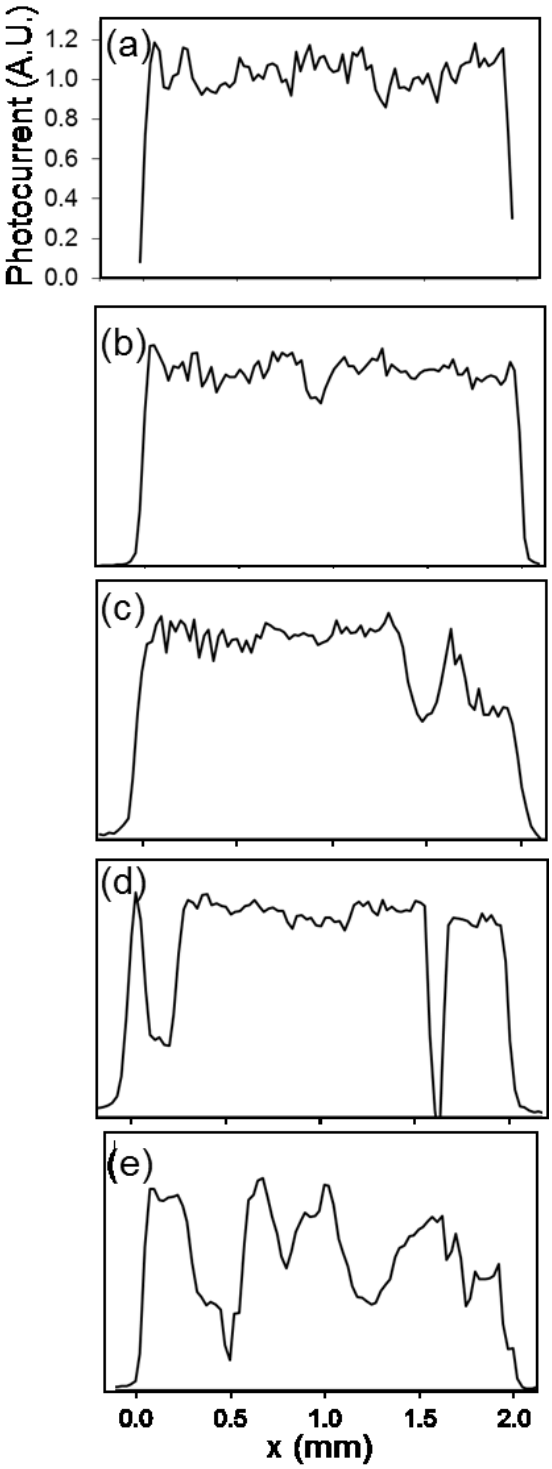

Figure S5: *Cross-sectional data from LBIC maps of Device A-E shown in Figure 4 (main text) shown in parts (a) to (e).*

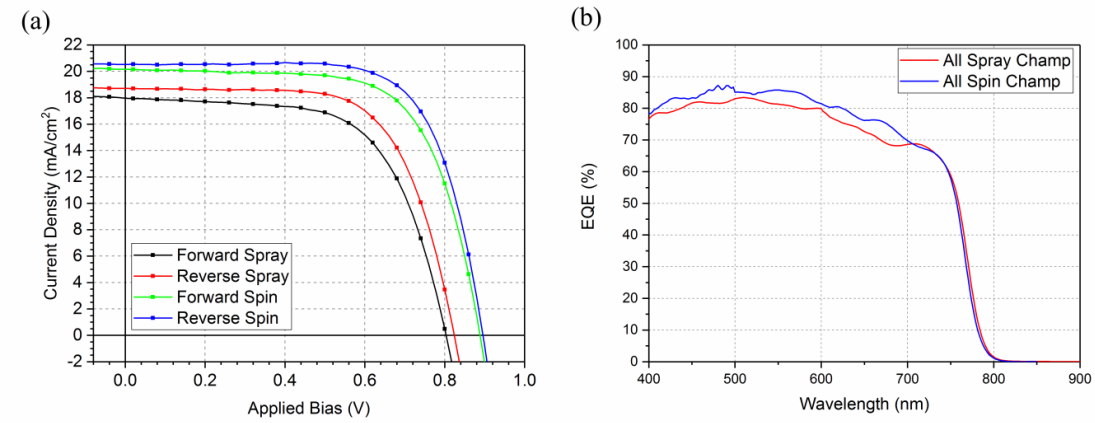

Figure S6: *Champion J-V [part (a)] from small-area device's E (all-spray-cast) and A (all-spin cast). The champion all-spin device has an efficiency of 12.9 % whilst the champion all-spray device has an efficiency of 10.2 %. Part b shows EQE spectrum's for these devices with respect to AM 1.5 illumination. We calculate the expected values for the* J_{SC} *as 18.4 mA cm*$^{-2}$ *for device E and 19.0 for device A.*

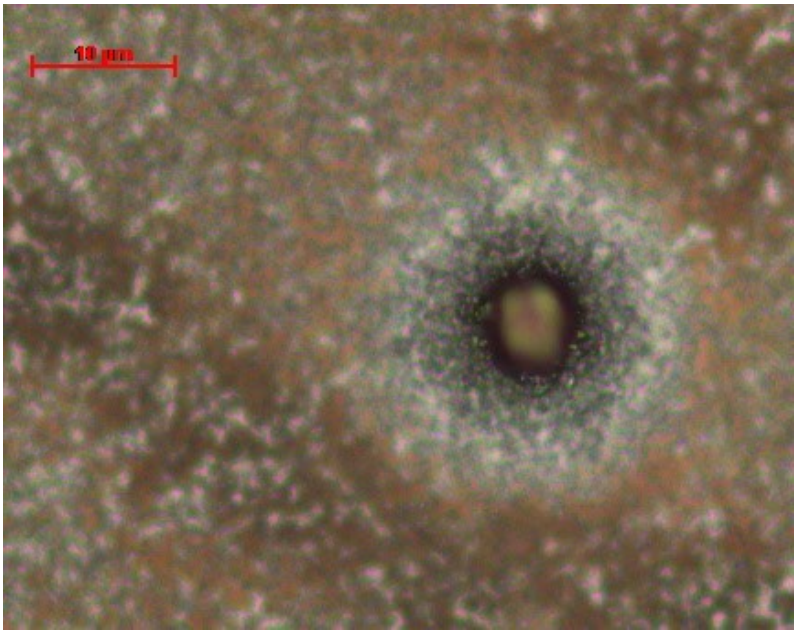

Figure S7: *Optical microscope image of aggregate in spray-cast perovskite film. The scale bar is 10 µm.*

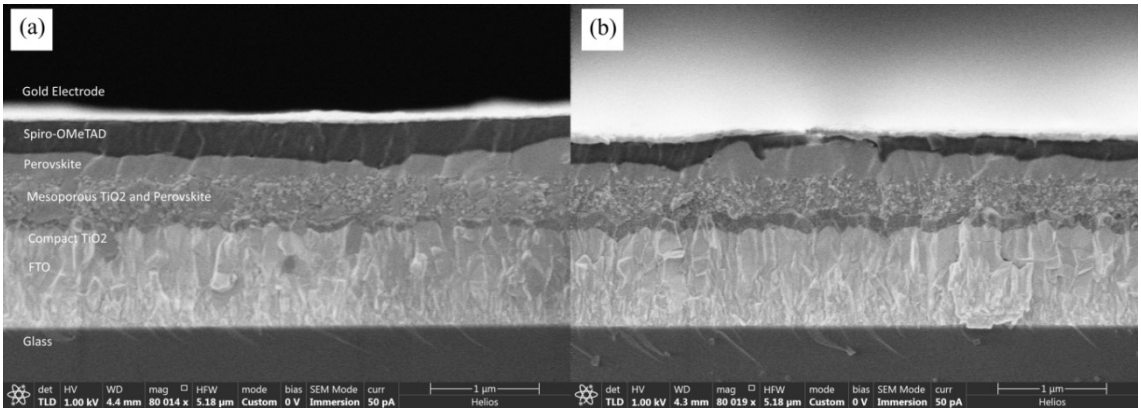

Figure S8: *Cross sectional SEM for device A (part a) and device E (part b).*

5.4: Further Context

Whilst undertaking this work it quickly became apparent that the performance of spray-cast PSCs was limited by the quality of the perovskite that could be produced in air. Compared to the state-of-the-art triple-cation based perovskites processed under nitrogen, spray-cast films were extremely rough and non-uniform. It became apparent that a method to manage the crystallisation of the precursor would have to be developed, in order to improve both uniformity of the perovskite and device performance (>15%). Fortunately the group had recently acquired a new glovebox based spray-coater and work began on developing new fabrication protocols with the aim to increase device performance.

5.5: References

[1] A. Kojima, K. Teshima, Y. Shirai, T. Miyasaka, *J. Am. Chem. Soc.* **2009**, *131*, 6050.

[2] W. S. Yang, J. H. Noh, N. J. Jeon, Y. C. Kim, S. Ryu, J. Seo, S. I. Seok, *Science.* **2015**, *348*, 1234.

[3] M. A. Green, A. Ho-baillie, H. J. Snaith, *Nat. Photonics* **2014**, *8*, 506.

[4] G. Xing, N. Mathews, S. S. Lim, Y. M. Lam, S. Mhaisalkar, T. C. Sum, *Science.* **2013**, *342*, 344.

[5] S. D. Stranks, G. E. Eperon, G. Grancini, C. Menelaou, M. J. P. Alcocer, T. Leijtens, L. M. Herz, A. Petrozza, H. J. Snaith, *Science.* **2013**, *342*, 341.

[6] R. J. Sutton, G. E. Eperon, L. Miranda, E. S. Parrott, B. A. Kamino, J. B. Patel, M. T. Hörantner, M. B. Johnston, A. A. Haghighirad, D. T. Moore, H. J. Snaith, *Adv. Energy Mater.* **2016**, *6*, 1502458.

[7] G. E. Eperon, S. D. Stranks, C. Menelaou, M. B. Johnston, L. M. Herz, H. J. Snaith, *Energy Environ. Sci.* **2014**, *7*, 982.

[8] H. J. Snaith, *J. Phys. Chem. Lett* **2013**, *4*, 3623.

[9] M. A. Green, *Prog. Photovoltaics Res. Appl.* **2012**, *20*, 472.

[10] J. Gong, S. B. Darling, F. You, *Energy Environ. Sci.* **2015**, *8*, 1953.

[11] L. Yang, A. T. Barrows, D. G. Lidzey, T. Wang, *Reports Prog. Phys.* **2016**, *79*, 026501.

[12] D. Guo, J. Yu, K. Fan, H. Zou, B. He, *Sol. Energy Mater. Sol. Cells* **2017**, *159*, 518.

[13] S. G. Li, K. J. Jiang, M. J. Su, X. P. Cui, J. H. Huang, Q. Q. Zhang, X. Q. Zhou, L. M. Yang, Y. L. Song, *J. Mater. Chem. A* **2015**, *3*, 9092.

[14] T. M. Schmidt, T. T. Larsen-Olsen, J. E. Carlé, D. Angmo, F. C. Krebs, *Adv. Energy Mater.* **2015**, *5*, 1500569.

[15] Y. Deng, E. Peng, Y. Shao, Z. Xiao, Q. Dong, J. Huang, *Energy Environ. Sci.* **2015**, *8*, 1544.

[16] A. Barrows, A. Pearson, C. Kwak, A. Dunbar, A. Buckley, D. Lidzey, *Energy Environ. Sci.* **2014**, *7*, 2945.

[17] J. G. Tait, S. Manghooli, W. Qiu, L. Rakocevic, L. Kootstra, M. Jaysankar, C. A. Masse de la Huerta, U. W. Paetzold, R. Gehlhaar, D. Cheyns, P. Heremans, J. Poortmans, *J. Mater. Chem. A* **2016**, *4*, 3792.

[18] H. Huang, J. Shi, L. Zhu, D. Li, Y. Luo, Q. Meng, *Nano Energy* **2016**, *27*, 352.

[19] S. Das, B. Yang, G. Gu, P. C. Joshi, I. N. Ivanov, C. M. Rouleau, T. Aytug, D. B. Geohegan, K. Xiao, *ACS Photonics* **2015**, *2*, 680.

[20] F. C. Krebs, *Sol. Energy Mater. Sol. Cells* **2009**, *93*, 394.

[21] R. R. Søndergaard, M. Hösel, F. C. Krebs, *J. Polym. Sci. Part B Polym. Phys.* **2013**, *51*, 16.

[22] S. Bose, S. S. Keller, T. S. Alstrøm, A. Boisen, K. Almdal, *Langmuir* **2013**, *29*, 6911.

[23] N. P. Pham, E. Boellaard, J. N. Burghartz, P. M. Sarro, *J. Microelectromechanical Syst.* **2004**, *13*, 491.

[24] N. P. Pham, J. N. Burghartz, P. M. Sarro, *J. Micromechanics Microengineering* **2005**, *15*, 691.

[25] Z. Liang, S. Zhang, X. Xu, N. Wang, J. Wang, X. Wang, Z. Bi, G. Xu, N. Yuan, J. Ding, *RSC Adv.*

2015, *5*, 60562.

[26] H. Huang, J. Shi, S. Lv, D. Li, Y. Luo, Q. Meng, *Chem. Commun.* **2015**, *51*, 10306.

[27] D. K. Mohamad, J. Griffin, C. Bracher, A. T. Barrows, D. G. Lidzey, *Adv. Energy Mater.* **2016**, *6*, 1600994.

[28] K. Hwang, Y. S. Jung, Y. J. Heo, F. H. Scholes, S. E. Watkins, J. Subbiah, D. J. Jones, D. Y. Kim, D. Vak, *Adv. Mater.* **2015**, *27*, 1241.

[29] C. Chen, Y. Cheng, Q. Dai, H. Song, *Sci. Rep.* **2015**, *5*, 1.

[30] C. Zhang, Y. Luo, X. Chen, W. Ou-Yang, Y. Chen, Z. Sun, S. Huang, *Appl. Surf. Sci.* **2016**, *388*, 82.

[31] C. Liang, Z. Wu, P. Li, J. Fan, Y. Zhang, G. Shao, *Appl. Surf. Sci.* **2017**, *391*, 337.

[32] S. Sanzaro, E. Smecca, G. Mannino, C. Bongiorno, G. Pellegrino, F. Neri, G. Malandrino, M. R. Catalano, G. G. Condorelli, R. Iacobellis, L. De Marco, C. Spinella, A. La Magna, A. Alberti, *Sci. Rep.* **2016**, *6*, 1.

[33] T. Wang, N. W. Scarratt, H. Yi, A. D. F. Dunbar, A. J. Pearson, D. C. Watters, T. S. Glen, A. C. Brook, J. Kingsley, A. R. Buckley, M. W. A. Skoda, A. M. Donald, R. A. L. Jones, A. Iraqi, D. G. Lidzey, *Adv. Energy Mater.* **2013**, *3*, 505.

[34] R. D. Deegan, O. Bakajin, T. F. Dupont, **1997**, *389*, 827.

[35] L. Kavan, M. Grätzel, *Electrochim. Acta* **1995**, *40*, 643.

[36] D. K. Mohamad, B. G. Freestone, R. Masters, M. Reinhardt, S. Canning, C. Rodenburg, D. G. Lidzey, *J. Mater. Chem. C* **2017**, *5*, 2352.

[37] G. Cotella, J. Baker, D. Worsley, F. De Rossi, C. Pleydell-Pearce, M. Carnie, T. Watson, *Sol. Energy Mater. Sol. Cells* **2017**, *159*, 362.

[38] X. Fanton, A. M. Cazabat, *Langmuir* **2002**, *14*, 2554.

[39] C. Girotto, D. Moia, B. P. Rand, P. Heremans, *Adv. Funct. Mater.* **2011**, *21*, 64.

[40] J. Griffin, A. J. Ryan, D. G. Lidzey, *Org. Electron. physics, Mater. Appl.* **2017**, *41*, 245.

[41] D. P. Birnie, *Langmuir* **2013**, *29*, 9072.

[42] D. E. Haas, D. P. Birnie, *J. Mater. Sci.* **2002**, *37*, 2109.

[43] C. Yi, X. Li, J. Luo, S. M. Zakeeruddin, M. Grätzel, *Adv. Mater.* **2016**, *28*, 2964.

[44] Gwyddion – Free SPM (AFM, SNOM/NSOM, STM, MFM, …) data analysis software (http://gwyddion.net/, 2016).

[45] J. H. Heo, D. H. Song, S. H. Im, *Adv. Mater.* **2014**, *26*, 8179.

[46] J Nelson, *The Physics of Solar Cells*, Imperial College Press, **2003**.

Chapter 6

Volume 10, Issue 46

2018/11/21

39428

ACS APPLIED MATERIALS & INTERFACES

High Efficiency Spray-Coated Perovskite Solar Cells Utilising Vacuum Assisted Solution Processing

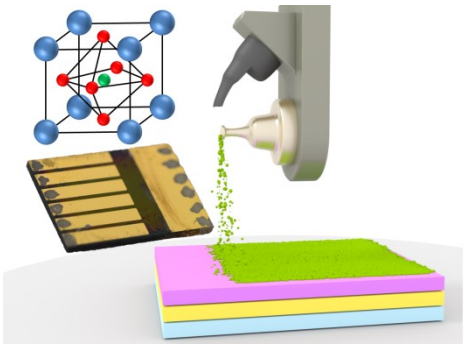

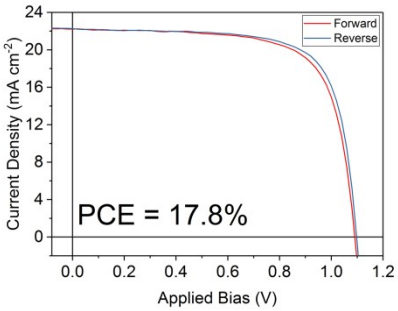

For the journals PDF:

DOI: 10.1021/acsami.8b14859

6.1: Publication Forward

By the summer of 2018 several groups had reported spray-cast perovskite solar cells with increasing power conversion efficiency. However all of the examples in the literature were using Methylammonium Lead Triiodide as the perovskite absorber which is a well-studied material, but many labs had moved towards the higher performance triple-cation perovskite formulations. A gap in the literature therefore existed to demonstrate the use of triple-cation perovskite in a spray-cast device. In this chapter a fabrication process to produce highly efficient perovskite solar cells via spray-deposition is developed, where a low vacuum is employed to manage the crystallisation of the perovskite layer. As of writing this paper has been cited three times.

6.2: Publication Main Body

High Efficiency Spray-Coated Perovskite Solar Cells Utilising Vacuum Assisted Solution Processing

James E. Bishop,[1] Joel A. Smith,[1] Claire Greenland,[1] Vikas Kumar,[2] Naoum Vaenas,[1] Onkar S. Game,[1] Thomas J. Routledge,[1] Michael Wong-Stringer,[1] Cornelia Rodenburg,[2] and David G. Lidzey[1*]

1) Department of Physics & Astronomy, University of Sheffield, Hicks Building, Hounsfield Road, Sheffield, S3 7RH, U.K.
2) Department of Materials Science & Engineering, University of Sheffield, Mappin Street, Sheffield S1 3JD, U.K.

*Corresponding author, email d.g.lidzey@sheffield.ac.uk

Abstract

We use ultrasonic spray-coating to fabricate caesium containing triple-cation perovskite solar cells having a power conversion efficiency up to 17.8%. Our fabrication route involves a brief exposure of the partially wet spray-cast films to a coarse-vacuum; a process that is used to control film crystallisation. We show that films that are not vacuum exposed are relatively rough and inhomogeneous, while vacuum exposed films are smooth and consist of small and densely-packed perovskite crystals. The process techniques developed here represent a step towards a scalable and industrially compatible manufacturing process capable of creating stable and high-performance perovskite solar cells.

Publication Main Text

Metal-halide perovskites are high-performance semiconductor materials that have received significant attention due to their applications in photovoltaic (PV) devices. Although initial power conversion efficiencies (PCEs) of perovskite PVs were low (3.8% in 2009),[1] this has increased rapidly as a result of world-wide research effort, with the best single junction devices now having an efficiency in excess of 23% PCE.[2] Perovskites combine many properties that make them effective photovoltaic materials, including efficient light absorption, tuneable bandgap, high charge-carrier mobility and low non-radiative recombination rates.[3,4] Importantly, perovskite films can be formed from solution at low temperature; a useful property for mass production of cheap, efficient solar cells using a variety of scalable deposition techniques such as slot-die coating,[5] ink-jet printing,[6] blade coating,[7] and spray-coating.[8]

For perovskite PV to be manufacturable at high volume, it is necessary to develop practical processes that enable the fabrication of high quality, uniform thin-films. Amongst the techniques that are currently being explored to fabricate perovskite PV, spray-coating has emerged as an industrially compatible process that can coat large areas at speed. Ultrasonic spray-coating was first used to deposit a $CH_3NH_3I/PbCl_2$ precursor ink which was then used to fabricate PV devices having a maximum PCE of 11%.[8] A number of groups have subsequently explored spray-coating to deposit perovskite materials, with a range of techniques explored.

Notably Das *et al.* created spray-cast $CH_3NH_3PbI_{(3-x)}Cl_x$ PV devices using a compact $TiO_2$and spiro-OMeTAD electron- and hole-transport layers, with an efficiency of 13% demonstrated.[9] Tait *et al.* further improved device efficiency to 15.7% by spray-casting PV devices based on a lead acetate/$PbCl_2$ precursor.[10] By separately spray-coating PbI_2 and MAI in a two-step process, Huang *et al.* improved device efficiency to 16.03%.[11] Recent work by Heo *et al.*[12] explored a process in which a substrate held at 120 °C was continually spray-coated with a DMF / GBL solution containing $CH_3NH_3PbI_{3-x}Cl_x$ for 2 minutes. By balancing incoming and outgoing solvent fluxes (with the outgoing flux controlled via solvent compositon), they created a solvent-rich layer in which the growth of large perovskite grains was encouraged, forming highly uniform perovskite films.[12] Such films were then combined with other spin-cast charge-extraction layers to create a PV device with 18.3% PCE. While such efficiencies are very impressive, there are questions about whether such a slow deposition process would be commercially scalable. Secondly, we note that the $CH_3NH_3PbI_{3-x}Cl_x$ perovskite is thermally unstable above 85 °C due to the low energy required to liberate organic decomposition products from the perovskite crystal lattice;[13,14] a feature that might limit its possible applications.

To circumvent this problem researchers have increasingly turned to the use of mixed cation/halide systems. Here, formamidinium ($HC(NH_2)_2$) (FA) was first introduced into a methylammonium based perovskite to reduce the semiconductor bandgap and thereby increase optical absorption at longer wavelengths.[15] It was then found that the photoactive black phase of $FAPbI_3$[16] could be stabilised by combining $MAPbBr_3$ with $FAPbI_3$. Further improvements in material properties then resulted from the addition of caesium to the perovskite, creating high-performance and stable "triple-cation" devices with PCEs of up to 21.1%.[17] While this material system currently represents the state-of-the-art for perovskite semiconductors, triple-cation perovskites have not yet been deposited by spray-coating.

In this article we demonstrate for the first time the spray-deposition of triple-cation perovskite layers, which we then use to produce cells with PCEs up to 17.8%. Importantly, we utilise a vacuum flash assisted solution processing (VASP) method[18] to control the crystallisation of the wet precursor film, with this

technique allowing us to spray-coat highly specular perovskite films of comparable quality to those produced via spin coating. This combination of advanced materials-selection, scalable-deposition processes and control over crystallisation processes are likely be key ingredients in a spray-based manufacture process.

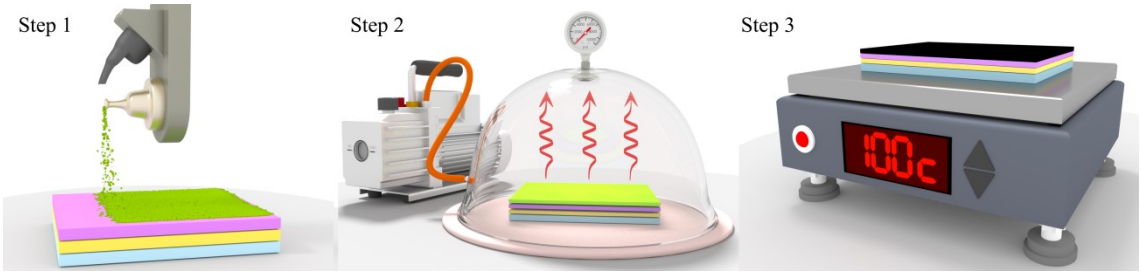

Figure 1: *Schematic illustration of the spray-deposition and VASP treatment process used to fabricate high quality perovskite films. In step 1 the spray-head moves across the surface depositing the precursor ink which then forms into a wet film. In step 2 the wet film is exposed to a partial vacuum for 5 minutes to drive out DMF from the film, forming a partially crystallised layer. In step 3 the semi-crystallised perovskite film is annealed at 100* °C *to form the perovskite phase.*

The perovskite precursor inks from which we have fabricated PV devices were created from a mixture of caesium iodide, formamidinium iodide, lead iodide, methylammonium bromide and lead bromide dissolved in a mixture of DMF and DMSO at a 4:1 ratio. The powders were mixed stoichiometrically such that the final perovskite precursor had the composition $CsI_{0.05}((FAPbI_3)_{0.85}(MAPbBr_3)_{0.15})_{0.95}$. A detailed process recipe and further experimental details are given in the Supporting Information.

Thin-films were spray-cast using a Sonotek ExactaCoat system fitted with an "Impact" ultrasonic nozzle, with the system located inside a nitrogen filled glovebox. Our deposition process is summarised schematically in Figure 1. The ultrasonic spray-coating process is based upon a piezo-electric nozzle that is resonated at kHz frequency. A solution of interest is then fed through the nozzle, with shear forces created by the oscillation causing the solution to break into a mist of micron-sized droplets. A carrier gas (in this case nitrogen) is then used to guide the droplets to the surface. The key advantage of ultrasonic spray-coating over traditional air-brush techniques is that a highly uniform size distribution of

droplets can be generated. This can - in principle - lead to the formation of more uniform surface coatings and hence better quality films.[8,19,20]

In the experiments described, the ultrasonic spray-head was mounted onto a motorised gantry, with the spray-head moving across the substrate and coating it in a single pass that took a few seconds. This process reproduces the action of a R2R production line, in which a substrate moves continuously through the system (here corresponding to a coating velocity of 50 mm s^{-1}).

We have found through careful optimisation that uniform perovskite precursor films can be created by spray-coating the precursor ink onto a substrate held at 40 °C at a flow rate of 1 mL min^{-1}. Coating was performed at a spray-head velocity of 50 mm s^{-1} with a head height of 10 cm above the substrate, with a shaping gas pressure of 3 psi and an ultrasonic nozzle power of 2 W. This produces a spray-pattern 3 cm wide that we use to coat our substrates in a single pass. After 30 seconds, droplets were observed to have merged into a uniform wet film. As we describe below it is critical that this wet film is exposed to a partial vacuum. Following this VASP process, films were annealed at 100 °C for 30 minutes to remove any remaining DMSO and convert the film into a smooth (root mean square roughness 22 nm), black perovskite film (see Figure S1).

To create PV devices, we have used the architecture ITO/np-SnO_2/perovskite/spiro-OMeTAD/Au. Here, the nanoparticle (np) SnO_2 film[21] was deposited by spin-coating a commercially available np-SnO_2 solution onto the ITO, which was then annealed at 150 °C for 30 minutes. In order to complete the device, a layer of doped spiro-OMeTAD was spin-cast onto the perovskite layer, followed by a gold top contact deposited by thermal evaporation through a shadow-mask, forming a series of 2 mm x 2 mm electrode-contacts. Devices were then tested via current-voltage (JV) measurements following exposure (through a 2.6 mm^2 aperture mask) to light from an AM 1.5 calibrated solar simulator. To explore film morphology and crystallinity, we performed scanning electron microscopy and thin-film x-ray diffraction. Device homogeneity was also characterised using laser-beam-induced current (LBIC) measurements. Here light from a 635 nm laser was

focussed onto the cell and then raster scanned in two dimensions whilst recording the photocurrent generated.

We have also performed time-resolved photoluminescence (TRPL) mapping of spray-cast films deposited on glass. Here a pulsed laser was focused onto the film using a microscope lens, with the laser spot raster scanned across the surface. The PL emission generated was collected using the same microscope lens, with a time correlated single photon counting technique then used to produce a TRPL decay curve at each location. These decay curves were fitted with a bi-exponential function, allowing us to build an image of the bimolecular recombination lifetime.

Perovskite films are polycrystalline in nature and controlling the morphology of such films often presents a challenge, as the size, shape and interconnectedness of the crystal grains is highly dependent on processing conditions. When triple-cation perovskite precursor films are deposited by spin-coating, it is common to utilise a so-called "anti-solvent quenching technique", where the precursor film is exposed to either chlorobenzene, toluene or some other non-polar solvent.[22] This exposure rapidly drives DMF out of the film,[23] with the remaining DMSO forming a crystalline intermediary phase with the perovskite constituents.[24] Subsequent annealing of the film removes the DMSO, thereby forming a high quality perovskite layer. In our experiments, we have found that it is relatively straightforward to create a uniform triple-cation perovskite precursor film by spray-coating, however the conversion of such a film into an optically dense, specular perovskite film is difficult. Simply annealing the unconverted precursor-film results in perovskite-films that are characterised by poor surface coverage and a high degree of roughness (100 nm). This appears to occur because there are insufficient nucleation sites for the crystallisation of the perovskite phase,[25] and as the substrate is heated, the rate of crystal growth suppresses the formation of further nucleation sites. This results in a film characterised by large crystallites having a lateral size of tens of microns,[8,26] rather than a uniform film composed of small, densely-packed crystallites (see Figures S2 and S3). We have found that PV devices based on triple-cation films created via a regular spray-coating process followed by thermal annealing are characterised by a low open circuit voltage and thus relatively low PCEs of around 10% (see Figure S4).

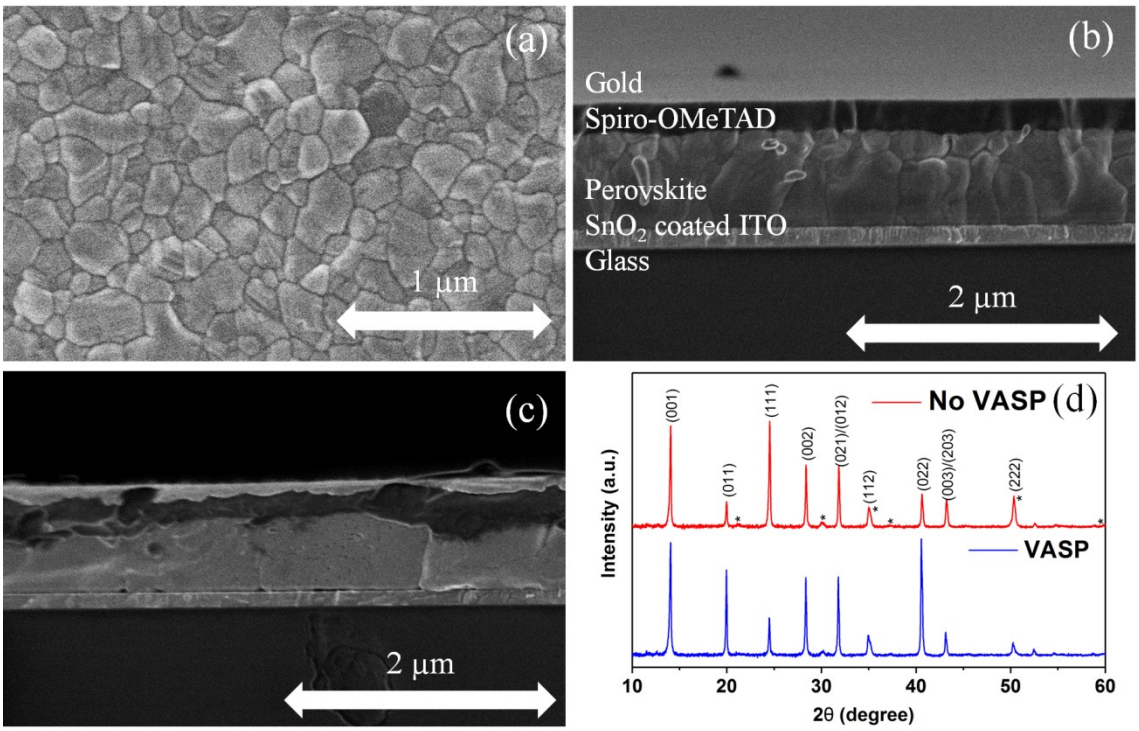

Figure 2: *Part (a) shows a SEM surface image of a spray-cast VASP treated triple-cation perovskite film. Parts (b) and (c) shows a cross-sectional SEM of a completed device containing a spray-cast triple-cation perovskite layer. Here the perovskite film shown in part (b) was exposed to a vacuum, while the film shown in part (c) was thermally annealed. Part (d) shows the results of thin film XRD measurements on VASP treated and untreated films. The asterisks refer to background peaks from the substrate.*

We note that Ulicna *et al.* have recently demonstrated high efficiency (17.3%) $CH_3NH_3PbI_{3-x}Cl_x$ spray-cast devices created by dipping a precursor film in diethyl ether to rapidly extract DMF from the film.[27] We have tried to replicate such an anti-solvent quench process, with both the perovskite-precursor and the antisolvent (chlorobenzene) delivered to the surface via spray-coating. Unfortunately this has proved to be an ineffective means of inducing the intermediate perovskite-DMSO phase. We also note that the scalability of this process is sub-optimal, as it requires the use and recovery of significant quantities of solvent.

To address this issue, we have explored a vacuum-based solvent extraction process developed by Li *et al.*[18] Here, it was shown that by exposing a freshly spin cast FA/MA mixed cation/iodide-bromide mixed anion precursor film to a low vacuum,

it was possible to form a DMSO intermediary phase. On annealing such vacuum treated films, high-quality, fully-crystalline perovskite layers were formed that were used to create high efficiency (20.5%) PV devices.

We have applied this technique to freshly spray-cast triple-cation perovskite precursor films, with films placed in a glovebox antechamber (reaching a final pressure of 0.8 mBar) for a period of 5 minutes immediately after deposition. An SEM image of the perovskite film surface and a device cross-section is shown in Figures 2a and b respectively. Here it can be seen that the film is composed of tightly packed grains having an average lateral size of around 200 nm. Figure 2c shows a cross-section of an otherwise identical spray-cast device that was fabricated without vacuum exposure. Here, it is evident that the perovskite layer is highly non-uniform, with significant thickness variations occurring over micron length-scales and numerous voids visible throughout the layer.

To compare the crystallinity of VASP treated and annealed-only triple-cation perovskite films we used X-ray diffraction (XRD) shown in Figure 2d. Samples were scanned across a broad 2θ range and peaks were identified associated with the room temperature cubic perovskite structure (space group $Pm3m$).[28] Comparing the scattering patterns of the two films, we find that there is significantly lower scattering intensity from the (011) plane in the untreated film, however scattering from the (111) plane is greatly increased, with scattering intensity from both the (002) and (021)/(012) peaks being reduced. Notably, there is no evidence of remnant solvent complexes or other precursor phases, which would be observed at small scattering angles in the region $2\theta<14°$.[22] This result suggests that the material formed in both cases is a cubic perovskite, but the different crystallisation routes clearly lead to a change in the crystal orientation of the resultant film. This difference in crystallographic orientation may impact the device performance due to different charge transport characteristics and interface behaviour. However the improved nanoscale morphology, controlled nucleation and overall better film quality achieved via the VASP treatment route are anticipated to play a dominant role in delivering high device performance.

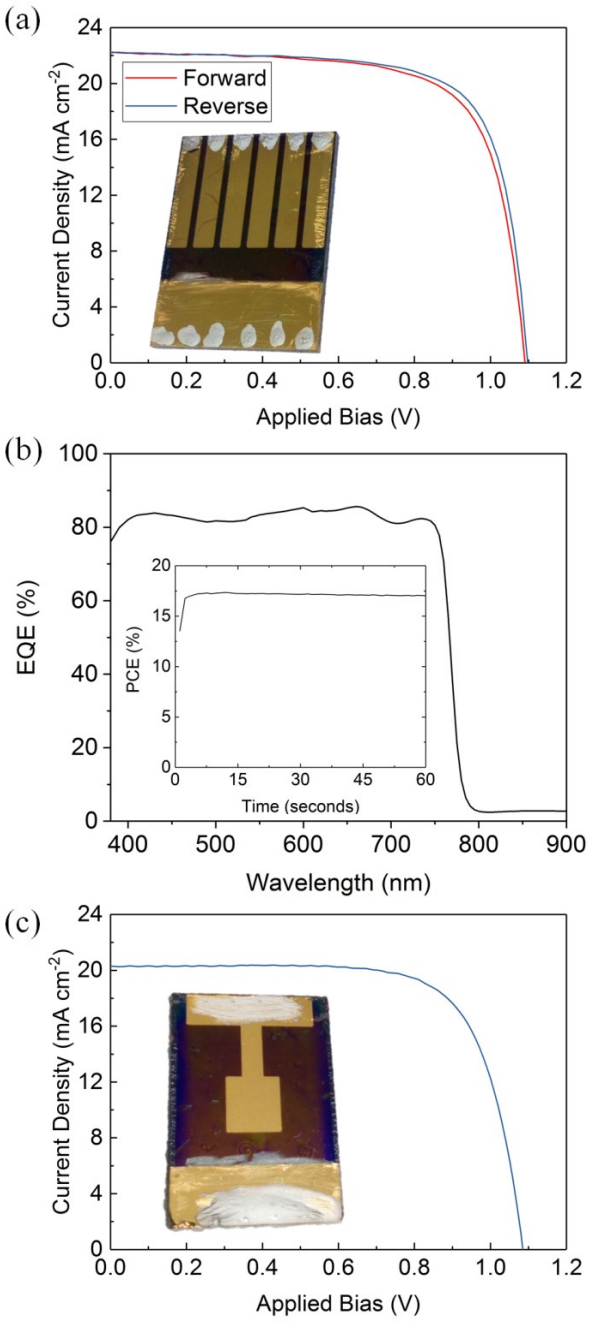

Figure 3: *Part (a) shows the current voltage characteristics for the champion spray-cast triple-cation perovskite solar cell with a reverse scan efficiency of 17.8%. The inset shows a photograph of the device. Part (b) shows an EQE spectrum recorded from a representative spray-cast perovskite cell (J_{SC} 21.4 mA cm^{-2}) corresponding to an integrated current of 20.3 mA cm^{-2}. The inset shows output power of the champion device held at a fixed voltage close to the maximum power point (920 mV) recorded over 60 s indicating a stabilised power output of 17%. Part (c) shows the current voltage characteristics of a larger area device with a reverse scan efficiency of 16%. The inset shows a photograph of the device.*

We have utilised this vacuum treatment step to make a series of photovoltaic devices. A JV curve of a champion device is shown in Figure 3a. Here, on reverse sweep, we obtained a device PCE of 17.8%; a value which compares favourably to the current highest efficiency spray-cast devices reported by Heo *et al.* that had an efficiency of 18.3%[12]. It is clear that the devices have only minimal hysteresis; a fact that we attribute to the use of SnO_2 nanoparticles, which have more favourable band alignment to triple-cation perovskite than the more widely used TiO_2.[21,29]

Scan direction	J_{SC} mA cm^{-2}	V_{OC} (V)	FF (%)	PCE (%)
Forward	**22.2** (21.4 ± 0.4)	**1.09** (1.07 ± 0.01)	**71** (65 ± 5)	**17.3** (14.7 ± 1.4)
Reverse	**22.3** (21.4 ± 0.4)	**1.10** (1.08 ± 0.01)	**73** (65 ± 4)	**17.8** (15.1 ± 1.3)

Table 1: *Reverse and forward sweep performance metrics for 18 spray-cast perovskite solar cells. Bold font indicates device metrics for the champion cell. Data shown in parenthesis represents average device metrics and associated standard deviation.*

In Table 1 we tabulate the average performance metrics of 18, 2.6 mm^2 spray-cast cells together with champion cell metrics. While this is a relatively small sample size, the low hysteresis and small standard deviation suggests our process is highly reproducible. Indeed, the J_{SC} and V_{OC} are consistently high, with variations in efficiency occurring as a result of a scatter in device fill factor (FF). The origin of this scatter in FF is currently not understood. We have determined the wavelength-dependent external quantum efficiency (EQE) of a representative cell as shown in Figure 3b. Here the integrated J_{SC} of 20.3 mA cm^{-2} is within 6 % of the average value reported in Table 1 (21.4 mA mA cm^{-2}). Unfortunately our EQE system cannot measure spectral response below 380 nm and thus the integrated J_{SC} is likely to be a slight underestimate of its actual value. We have also fabricated larger area devices (active area 16 mm^2) that have similar device performance to small area devices (see Figure 3c). A stabilised measurement recorded from such a device (15.4%) is shown in Figure S5.

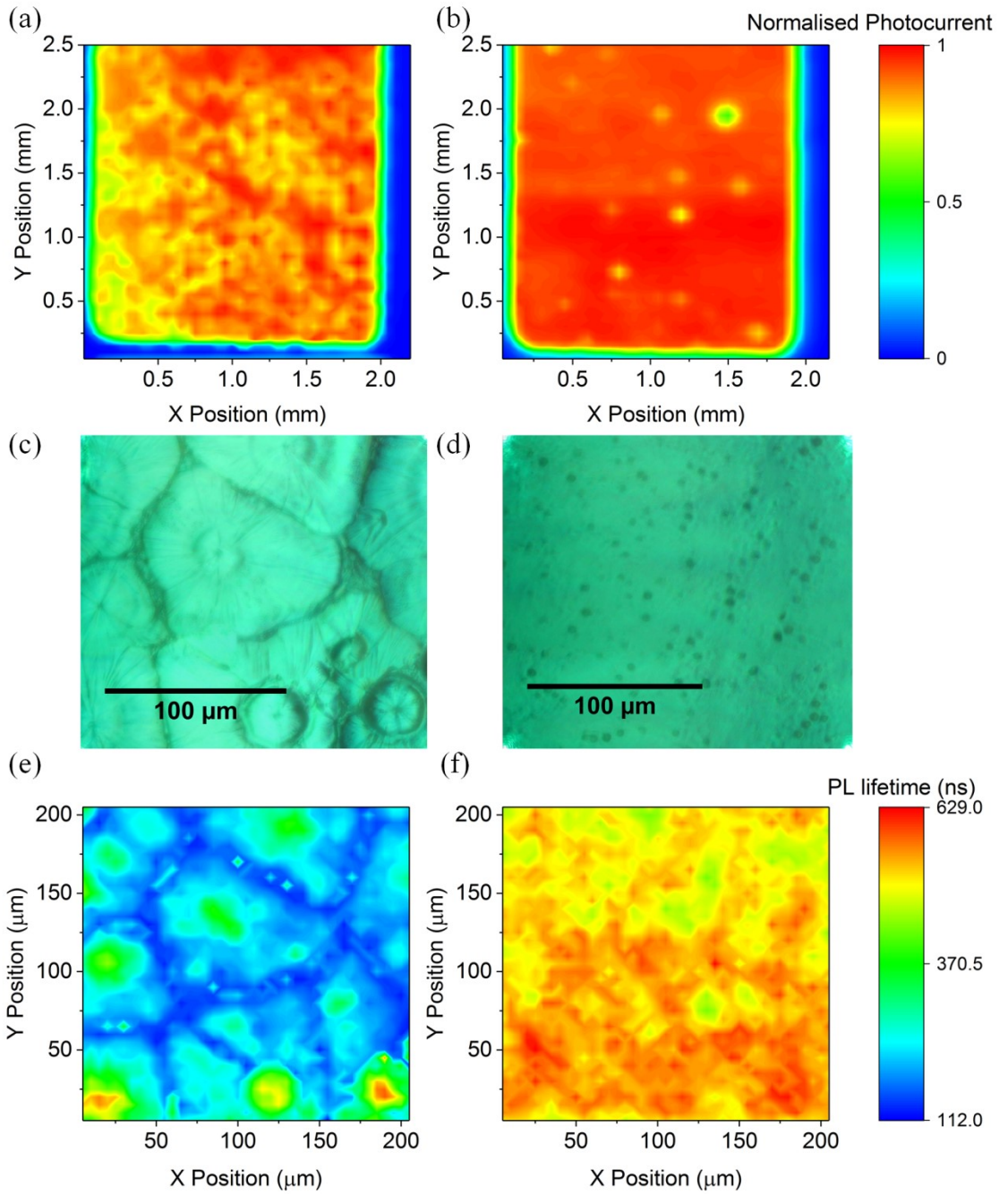

Figure 4: Laser-beam-induced current (LBIC) mapping, optical-microscope images, and time resolved photoluminescence (TRPL) mapping of spray-cast perovskite solar cells and films. Part (a) is an LBIC image of device that includes a perovskite layer that was thermally annealed only. Part (b) is a comparable device in which the perovskite precursor film was treated using the additional VASP process. Part (c) is an optical micrograph of a spray-cast film deposited on glass that had simply been annealed, and part (d) is a film that has undergone VASP treatment. Parts (e) and (f) are TRPL maps of the same regions of the film shown in parts (c) and (d).

In order to explore the homogeneity of the device photocurrent across the active area, we have performed laser-beam induced photocurrent mapping (LBIC) on spray-cast devices fabricated either with or without the additional vacuum exposure step. Typical images are shown in Figure 4. Part (a) shows an LBIC image of a device in which the perovskite precursor material had not undergone vacuum crystallisation. Here, it can be seen that there is a significant variation in the photocurrent generation over length-scales of around 100 μm. Part (b) shows an image of a comparable device that was fabricated using vacuum exposure; here the generated photocurrent appears significantly more uniform, apart from a small number of ``cold-spots'' that again have an average diameter of around 100 μm. We anticipate that such features most likely correspond to undissolved aggregates (most likely composed of lead-based compounds) that were originally contained within the perovskite precursor solution.[26]

In order to understand whether charge carrier lifetimes differ between VASP treated and untreated films we have performed time resolved photoluminescence (TRPL) mapping of films deposited on glass substrates. Figures 4c and 4d show microscope images of regions from untreated and treated samples that were then selected for mapping. It is clear from these images that the VASP treated film is significantly more uniform whereas the untreated film is dominated by large “flower-like” crystallites. Figures 4e and 4f show TRPL maps of the long decay lifetimes extracted from fits to the bimolecular recombination decay curves. Examples of the fits used to calculate these values are presented in Figure S6. Here the flower-like crystallites are clearly resolved, with the emission from the edges of such features apparently having much shorter lifetimes than those recorded from their centre. We speculate this is due to a higher density of non-radiative recombination centres found in these regions that occur as a result of a more disordered macro-structure together with compositional variations that are also observed in energy-dispersive x-ray spectroscopy (see Figure S7). In contrast, the VASP treated films are characterised by much longer average decay-lifetimes, with such decay transients having enhanced uniformity across the film surface.

In conclusion, we have demonstrated a method to fabricate triple-cation based perovskite solar cells having a peak power conversion efficiency of 17.8% using a

combination of ultrasonic spray-coating and vacuum assisted solution processing. The device efficiencies demonstrated are comparable with the highest efficiencies reported for a spray-cast perovskite devices.[12] Here the use of a relatively coarse vacuum both removes trapped solvent and initiates crystallization through controlled nucleation, with the films produced being of comparable quality to those produced via spin-coating. This allows us to create PV devices having enhanced photocurrent uniformity as evidenced using photocurrent mapping studies. Importantly, our work is the first example of the use of spray-casting to fabricate photovoltaic devices based on a triple-cation perovskite. Such perovskite materials are compatible with stable device-operation over prolonged time-scales[17] and have higher efficiency than those based on methylammonium lead triiodide; the current material of choice used to spray-cast PV devices.[8–12] We anticipate that further process optimisation will allow us to create spray-coated perovskite devices having efficiencies that match the state-of-the-art.

The process demonstrated uses a rapid, single-pass, spray-technique and is thus an important step towards high-speed, high volume perovskite PV device manufacture. Indeed, we expect that the deposition process used here could be further accelerated by using flash infrared annealing instead of the relatively slow thermal-annealing stage.[30] We emphasize that the use of vacuum processing steps are compatible with high-volume manufacture; for example metallised films are routinely deposited on moving substrate films such as polyethylene terephthalate (PET) via vacuum-based physical vapour deposition (PVD).[31] Notably, our process does not require the use of large quantities of solvent either in the initial spray-deposition step or in a subsequent anti-solvent quench, and is thus a step towards a more environmentally benign manufacture process.

Acknowledgements

This work was funded by the UK Engineering and Physical Sciences Research Council (EPSRC) via grants EP/M025020/1 “High resolution mapping of performance and degradation mechanisms in printable photovoltaic devices”, EPSRC grant EP/N008065/1 “Secondary Electron Emission - Microscopy for Organics With Reliable Engineering-Properties”, and EP/M014797/1 “Improved

Understanding, Development and Optimization of Perovskite-based Solar Cells". We also thank the EPSRC for PhD studentships via the University of Sheffield DTG account (J.E.B. and T.J.R.) and from the Centre for Doctoral Training in New and Sustainable PV, EP/L01551X/1 (M.W.S., J.A.S. and C.G.). We thank Dave Coles for providing an illustration of the spray-deposition process for figure 1.

Notes

D.G.L. is co-director of the company Ossila Ltd that retail materials and equipment for perovskite photovoltaic device research and development.

6.3: Supporting Information

Device Fabrication

Triple Cation Precursor - FaI (Ossila), MaBr (Dyesol), $PbBr_2$ (TCI), PbI_2 (TCI), and CsI (Sigma) were weighed out into a vial stoichiometrically to form the triple cation perovskite $CsI_{0.05}((FAPbI_3)_{0.85}(MAPbBr_3)_{0.15})_{0.95}$. For each 1 mL of precursor solution the following quantities of powder were used out: FaI (167 mg), PbI_2 (467 mg), MaBr (19 mg), $PbBr_2$ (68 mg) and CsI (16 mg). The powders were then dissolved in a mixture of DMF and DMSO at a ratio of 4:1 (800 µL and 200 µL).

Tin Oxide - Unpatterened ITO (20 Ω/sq, Ossila) was etched with 4M HCL and zinc powder before being sonicated in Hellmanex, deionised water and IPA. The substrates were then treated with a UV ozone plasma cleaner for 15 minutes. Tin oxide nanoparticle solution (SnO_2 colloidal solution 15% wt water) was diluted 1 part to 6.5 parts DI water (2.67% dilution) and spin coated in ambient conditions onto the ITO at 3000 rpm. The tin oxide was then heated for 30 minutes at 150°C and UV ozone treated for a further 15 minutes.

Perovskite Spray-Coating - The SnO_2 coated substrates were then transferred to a glovebox for spray deposition using a Sonotek Exactacoat system mounted with an Impact spray-head. Perovskite precursor was delievered at a rate of 1 $mLmin^{-1}$ through a tip driven at 2 W with a shaping gas at 3 Psi. The head was held 10 cm above the substrate which was mounted on a hotplate held at 40°C. During

deposition, the head moved in a line scan over the substrate at 50 mms^{-1} coating it in precursor. The width of the spray pattern is 3 cm allowing the coating of the 15 mm x 20 mm substrate in a single pass without any thickness variation.

After deposition the substrate was left for 30 s to allow an even wet film to form. The substrate was then transferred to the glovebox antechamber for vacuum exposure. The film was left for 5 minutes in the vacuum chamber whilst it pumped down to approximately 80 Pa. After 5 minutes, the vacuum chamber was rapidly re-filled with nitrogen. The film was then returned to the glovebox and placed on a secondary hotplate at 100°C for 30 minutes.

Several films did not undergo the VASP treatment and were directly transferred to the secondary hotplate for 30 minutes after spray-deposition to convert.

Spiro-OMeTAD/AU - Perovskite films were then transferred to a second glovebox for spiro-OMeTAD deposition. 2,2',7,7'-Tetrakis[N,N-di(4-methoxyphenyl)amino]-9,9'-spirobifluorene (Spiro-OMeTAD) powder was dissolved in CB at a concentration of 86.6 mgmL-1. It was then doped with lithium bis(trifluoromethanesulfonyl)imide (LITFSI Sigma), 4-tert-butyl-pyridine (TBP Sigma), and tris(2-(1H-pyrazol-1-yl)-4-tert-butylpyridine)cobalt(II) di[hexafluorophosphate] (FK209 Co(II) PF6 Dyesol). The quantity of dopant used in 1 mL of spiro-OMeTAD solution was as follows: 20 µL of LiTFSI (500 mgmL-1 in acetonitrile), 36 µL TBP, and 11 uL of FK209 (300 mgmL-1 in acetonitrile). The solution was filtered and then spin coated at 4000 rpm. Devices were left overnight in dry air to allow the Spiro-OMeTAD to oxidise. Finally 80 nm of gold was deposited in an Edwards bell jar evaporator through a shadow mask to create six 4 mm2 cells per substrate. Larger area devices were fabricated by using a larger shadow mask to create one 25 mm^2 cell per pixel.

Device and Film Characterisation

Current-Voltage Measurements - Devices were tested under AM 1.5 light produced by a Newport solar simulator. The light intensity was calibrated using a silicon reference cell (Newport) to 1000 Wm^2. The devices were mounted with a shadow mask to define an illuminated area of 2.6 mm^2 per 4 mm^2 cell. Devices

were scanned from -0.2 V to 1.2 V and then back to -0.2 V at a speed of 0.4 Vs^{-1} using a Keithley 237 source measure unit. Stabilised measurements were performed by holding the device at a fixed voltage close to the maximum power point. Larger area devices were illuminated through a 16 mm^2 shadow mask.

External Quantum Efficiency - EQE measurements were performed using a custom setup. Light from a 100 W tungsten halogen lamp was passed through a monochromator (Spectral Products DK240 1/4m) and illuminated onto the device. Photocurrent was measured using an Xtralien X100 source measure unit (Ossila) and compared to that produced by a silicon reference photodiode (Newport) with a known spectral response to calculate the EQE.

Laser-Beam-Induced Current Mapping - The laser-beam-induced-current (LBIC) mapping system comprised of a mechanically chopped laser that was passed through a spatial filter before being focused to a spot size of about 50 μm onto a device via a 10x objective. The sample was mounted on a computer controlled XY-stage, and moved in a sawtooth pattern in steps of 50 μm. A 4.5 mW, 635 nm diode laser (Thor labs, CPS635) was used to generate a photocurrent that was measured using a lock-in amplifier (Stanford Research Systems, SR830) which was referenced to the chopped laser.

Scanning Electron Microscopy – Top record topview SEM images, the sample was prepared with layers glass/ITO/SnO_2. An FEI Helios NanoLab G3 UC was used for all secondary electron (SE) imaging using a primary electron beam at an accelerating voltage of 1 keV with a working distance of 4 mm. SEs were detected through the lens detector (TLD) in immersion mode. Compositional analysis was performed using EDX-SEM using the Helios NanoLab G3 UC at an accelerating voltage of 10 keV. The emitted signals measured using an Oxford Instruments EDX spectrometer and analysed using AZtecEnergy acquisition and analysis software.

Atomic Force Microscopy - Tapping mode AFM was performed on an MFP-3D Bio using Brucker TESPA-V2 (320 kHz, 42N/m) cantilevers.

Time-Resolved Photoluminescence (TRPL) Mapping - TRPL maps were generated by raster scanning a laser spot across the surface of a thin film sample.

Here the sample was mounted on two stepper motor stages, facilitating movement in x- and y-directions with a step size of 5 μm. A TRPL decay curve was then measured using time-correlated single-photon counting (TCSPC) at each point in the scan. To generate the TRPL trace, the sample was excited with a 510 nm pulsed laser at a pulse frequency of 2.5 MHz, with PL emission collected using a PDM-series single photon avalanche diode (SPAD) purchased from Micro Photon Devices. Timing electronics were provided by a TimeHarp 260 PCIe board purchased from PicoQuant. The integration time for each measurement was 30 seconds with a time resolution of 0.1 ns.

The decay curves were fitted with a bi-exponential of the form $y(t) = Ae^{-Bt} + Ce^{-Dt}$ with the fluorescence lifetime τ shown in the maps in the main paper determined from $\tau = -\frac{1}{D}$.

X-ray Diffraction - X-ray diffraction patterns were collected from rotating perovskite films using a PANalytical X'Pert Pro diffractometer system using CuKα radiation (1.5406 Å) operating at 45 kV and 40 mA

Steady-State Photoluminescence and Absorbance – Absorbance data was recorded from thin films deposited on glass using an Ocean Optics Spectrometer (HR2000+ER) measuring attenuated signal from a deuterium halogen lamp (DH-2000-BAL). Excitation from a 405 nm diode laser was used to generate photoluminescence which was measured by an Andor Shamrock SR-303i-A triple grating imaging spectrograph.

Figure S1: *Photograph of spray-cast triple cation perovskite films. The edges of the substrates are sometimes rougher than the centre due to edge effects.*

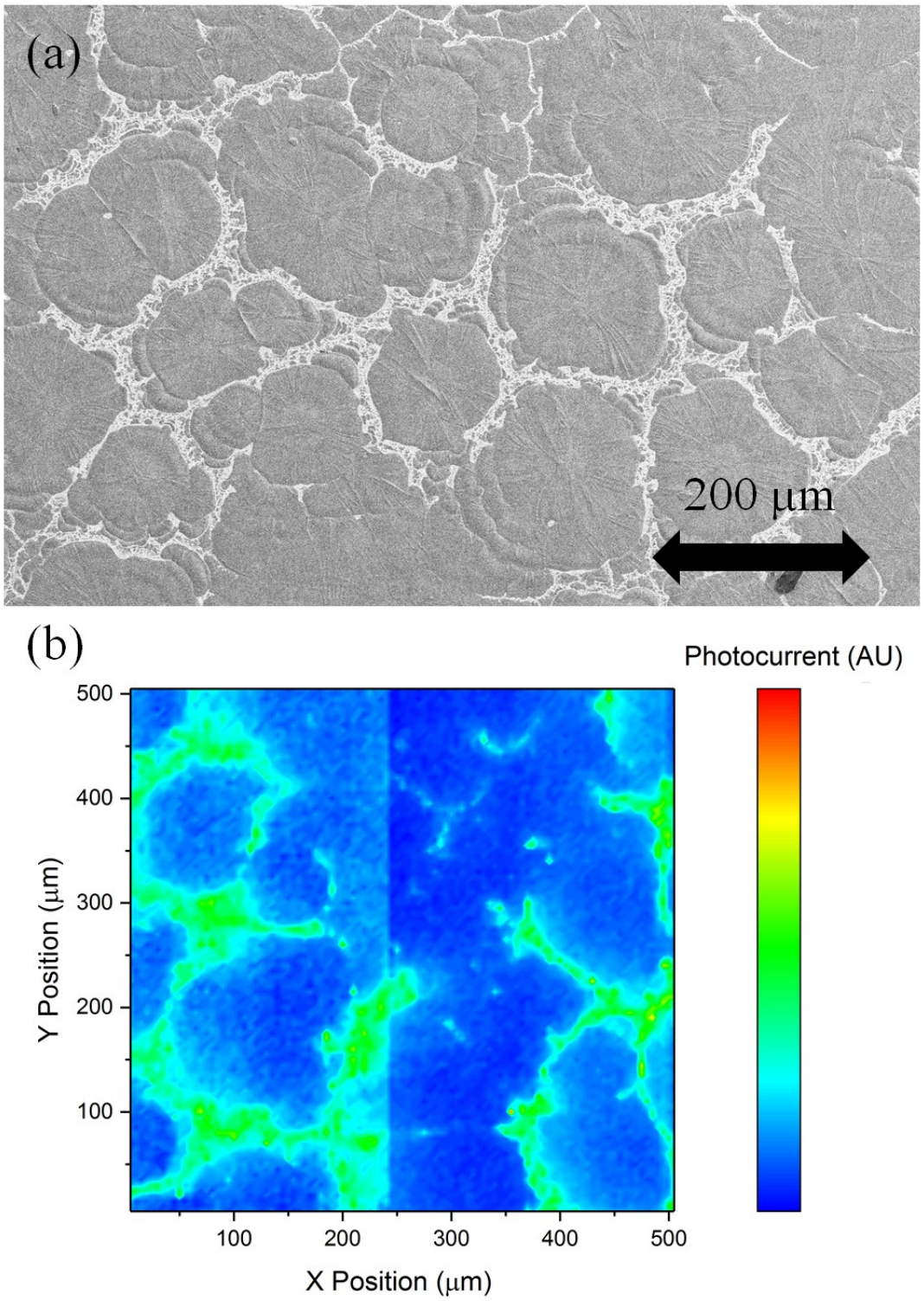

Figure S2: *(a) Low-resolution surface SEM image of a non-VASP treated spray-cast perovskite film. (b) High resolution LBIC image of a non-VASP treated spray-cast device.*

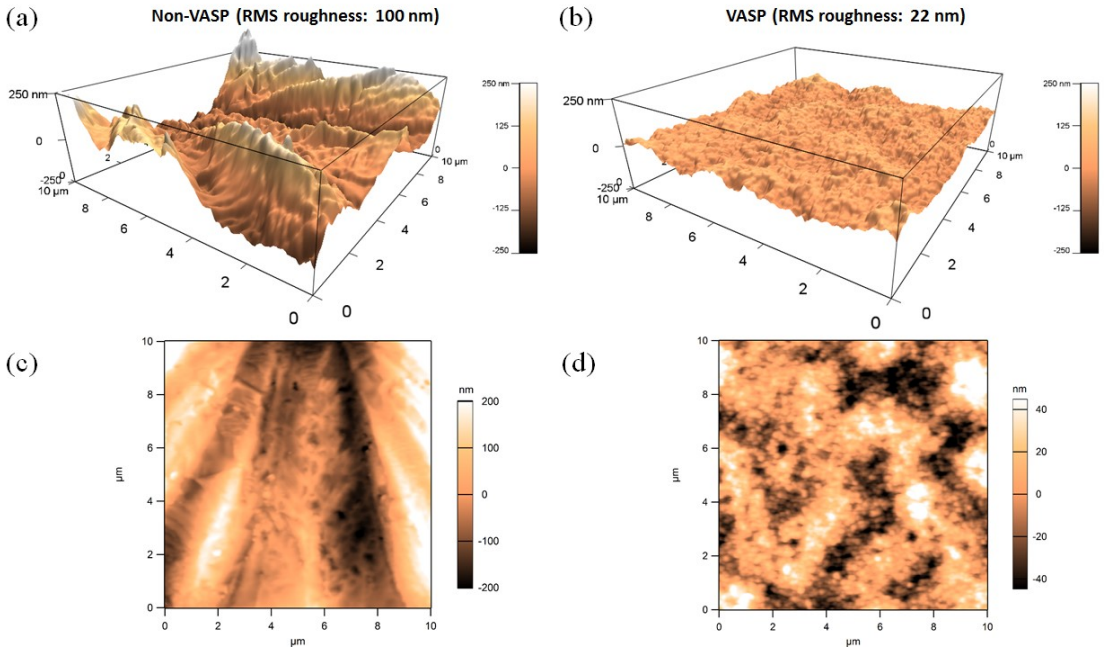

Figure S3: *Results of tapping mode surface AFM of non-VASP (parts (a) and (c)) and VASP treated (parts (b) and (d)) spray-cast films.*

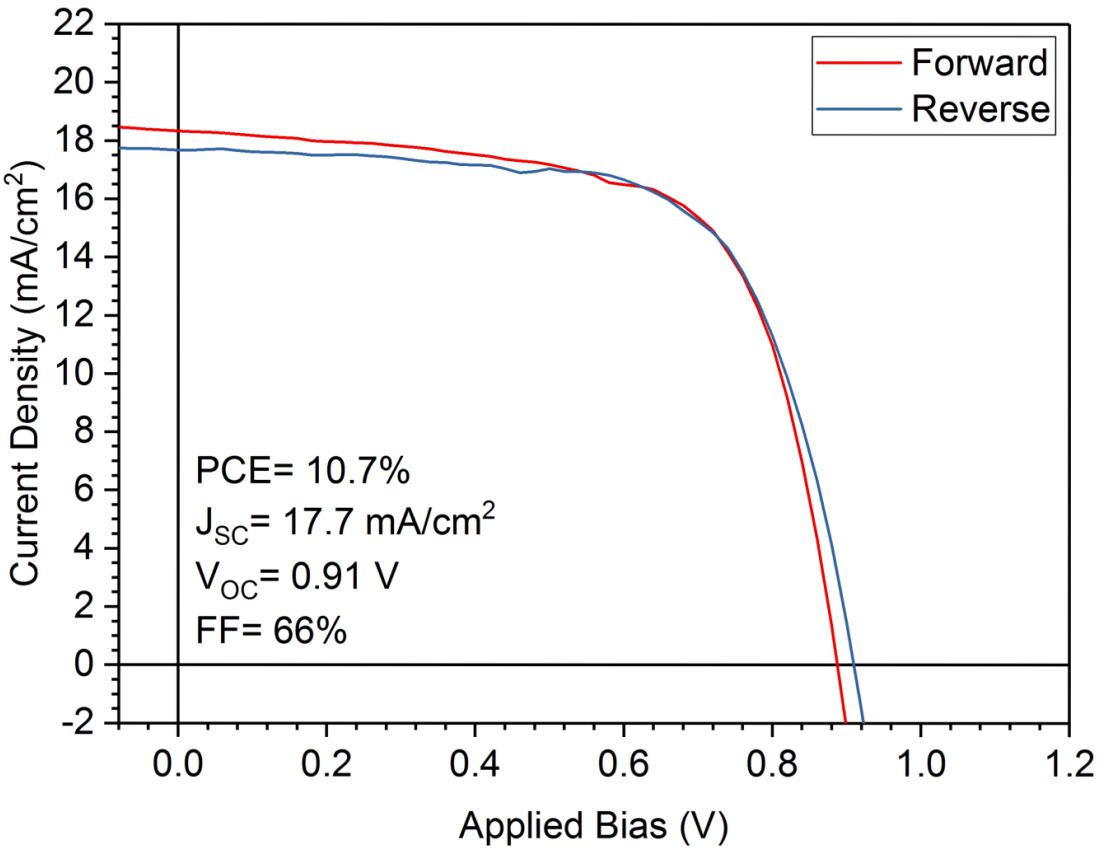

Figure S4: *JV measurement of a non-VASP treated spray-cast device using an np-SnO_2 ETL.*

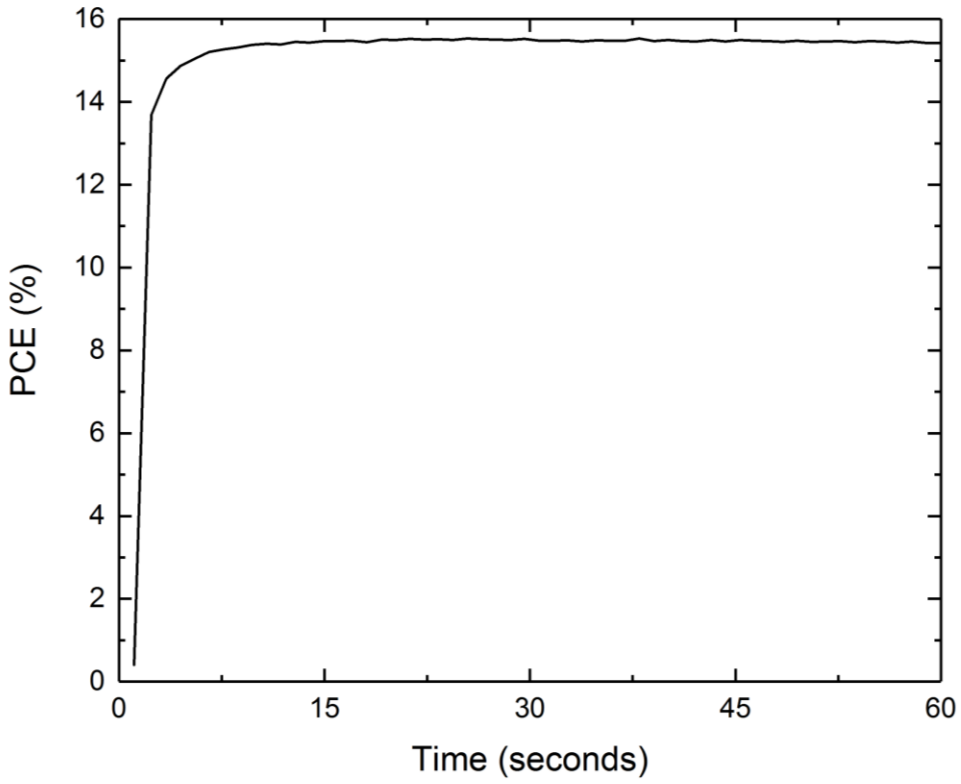

Figure S5: *Stabilised power output of a device with a larger active area (16 mm²) held at 0.82 V for 60 seconds.*

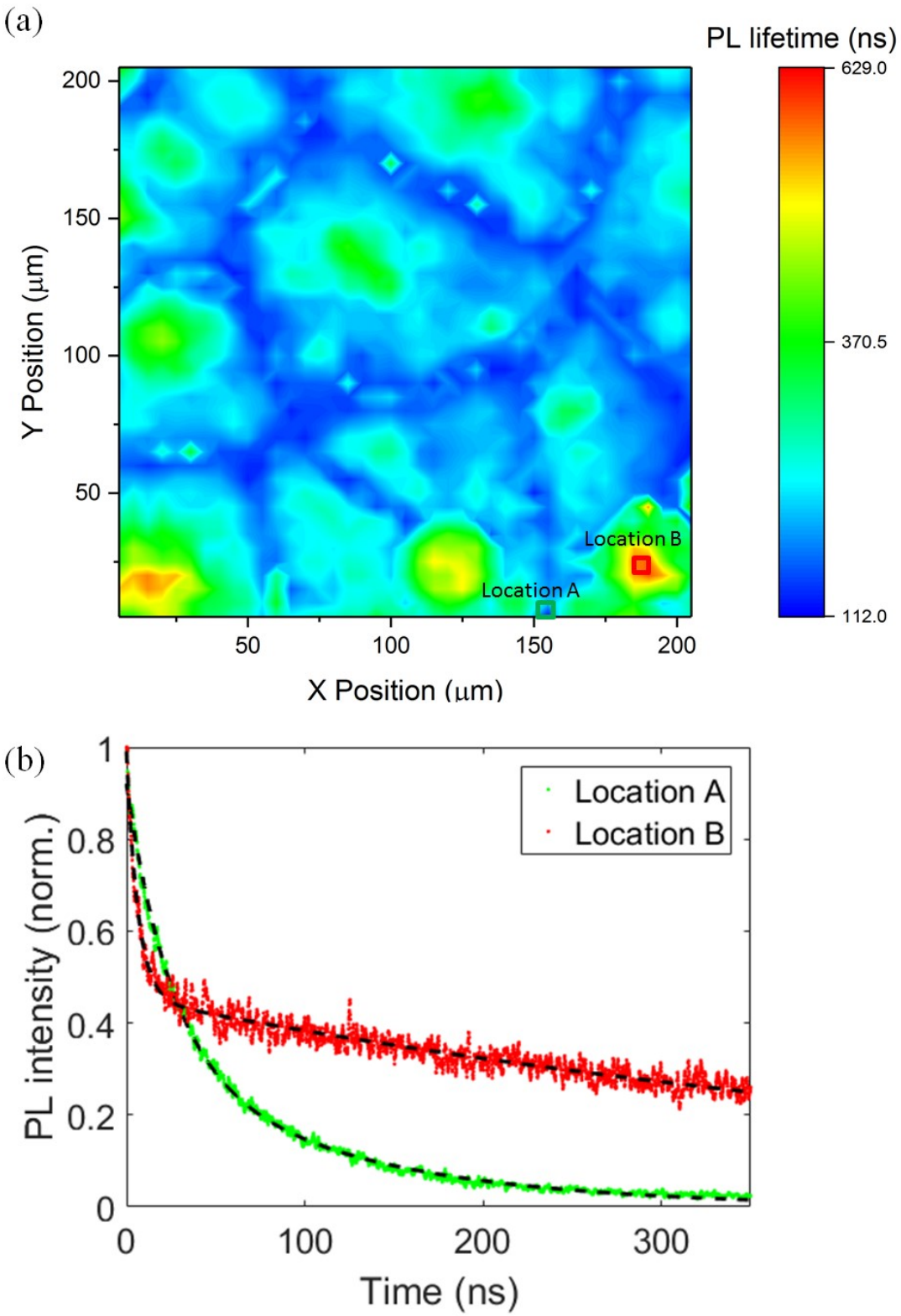

Figure S6: *Part (a) shows a TRPL map of film that has not undergone VASP treatment with two regions highlighted. Part (b) shows the TRPL decay transients recorded at those points (green is location A, red is location B) with the bi-exponential fits used to calculate the lifetime in black.*

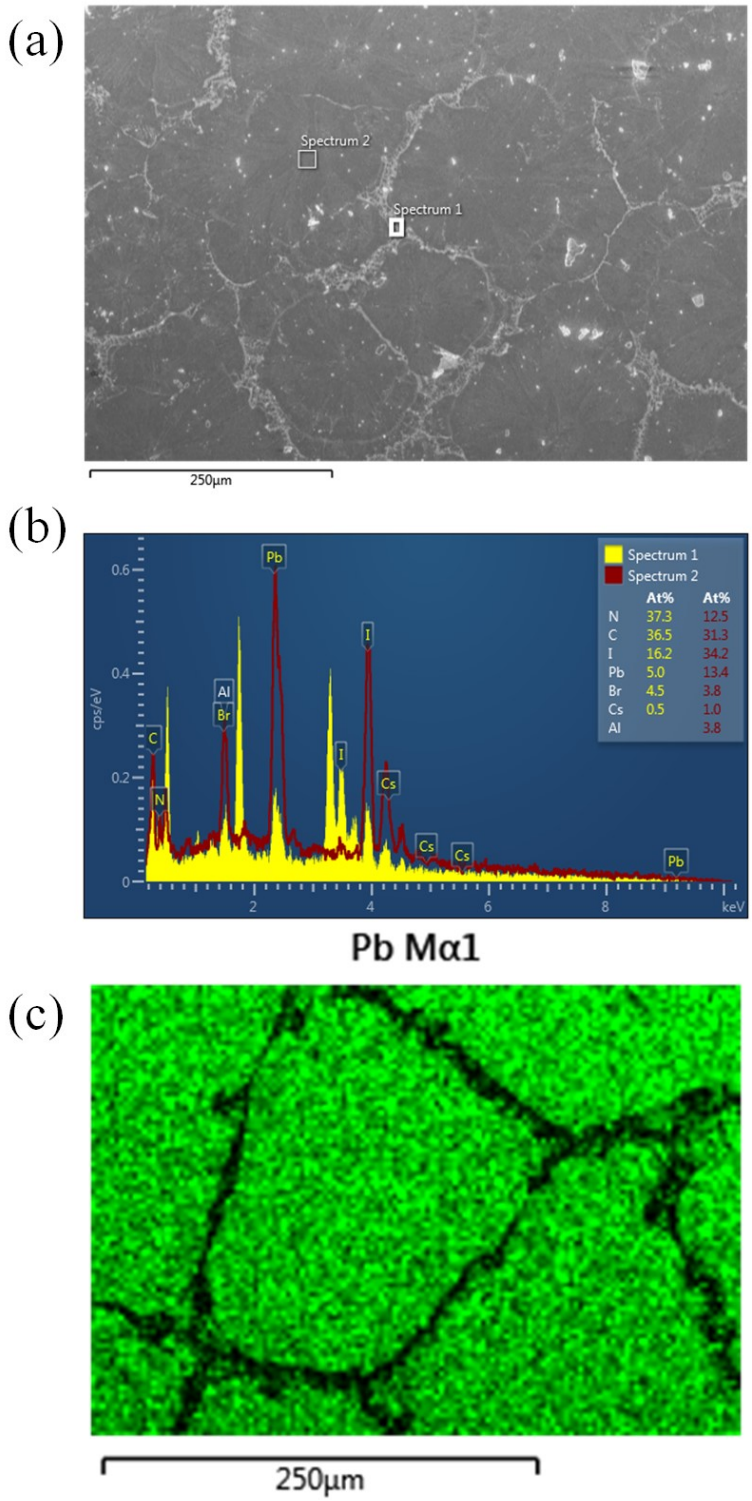

Figure S7: *Part (a) Surface SEM of a non-VASP film with two regions identified for analysis. Part (b) EDX spectrums for the two regions. Part (c) EDX map showing the abundance of lead across a crystallite in a non-VASP film.*

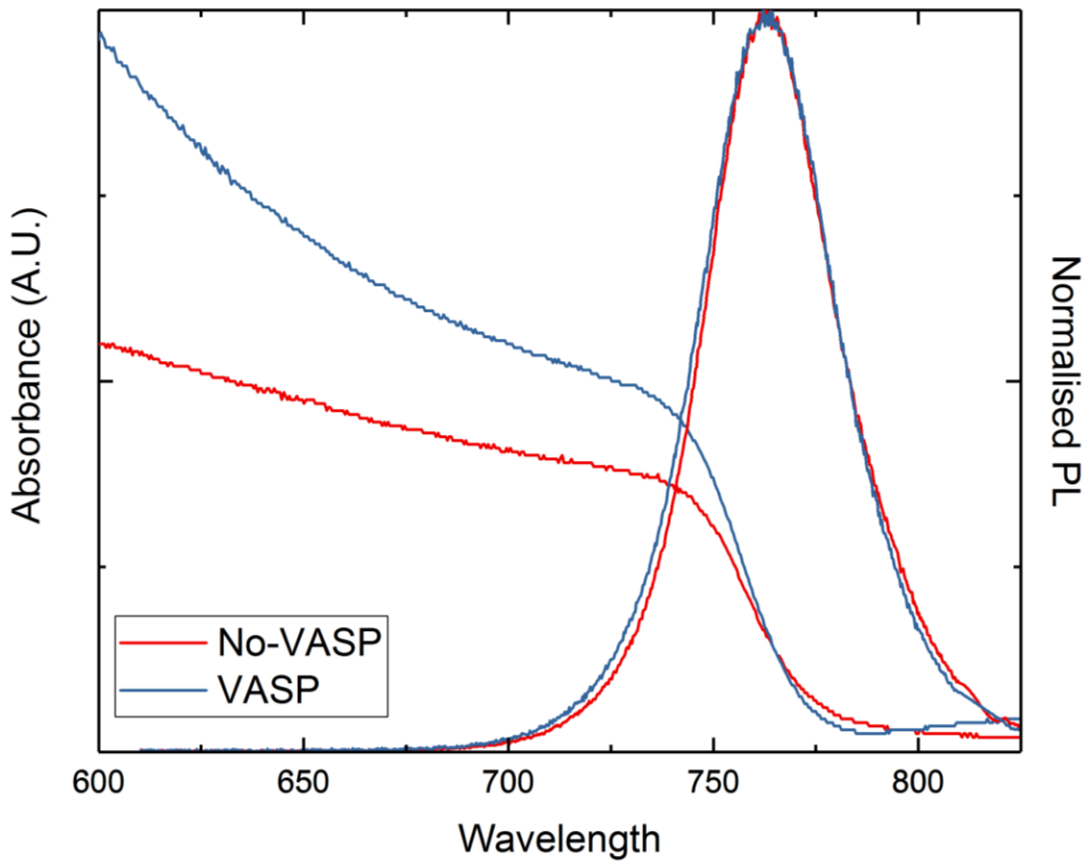

Figure S8: *Absorbance and steady state PL data recorded from non-VASP (red line) and VASP treated films.*

6.4: Further Context

The morphology of non-VASP films presented in this paper is very similar to the perovskite films spray-cast in Chapter 5. The development of the VASP method allowed a dramatic improvement in the uniformity of spray-coated films which in turn increased PCE. However only relatively small areas had been coated and thus the natural next step was to scale the process up to larger areas whilst maintaining high performance. In addition this presented an opportunity to build upon Chapter 5, enhancing the efficiency of our multilayer sprayed devices.

6.5: References

[1] A. Kojima, K. Teshima, Y. Shirai, T. Miyasaka, *J. Am. Chem. Soc.* 2009, *131*, 6050.

[2] NREL. Best Research-Cell Efficiencies. https://www.nrel.gov/pv/assets/images/efficiency-chart-20180716.jpg (accessed August 15 2018)

[3] S. D. Stranks, G. E. Eperon, G. Grancini, C. Menelaou, M. J. P. Alcocer, T. Leijtens, L. M. Herz, A. Petrozza, H. J. Snaith, *Science.* 2013, *342*, 341.

[4] M. A. Green, A. Ho-baillie, H. J. Snaith, *Nat. Photonics* 2014, *8*, 506.

[5] T. M. Schmidt, T. T. Larsen-Olsen, J. E. Carlé, D. Angmo, F. C. Krebs, *Adv. Energy Mater.* 2015, *5*, 1500569.

[6] S. G. Li, K. J. Jiang, M. J. Su, X. P. Cui, J. H. Huang, Q. Q. Zhang, X. Q. Zhou, L. M. Yang, Y. L. Song, *J. Mater. Chem. A* 2015, *3*, 9092.

[7] Y. Deng, E. Peng, Y. Shao, Z. Xiao, Q. Dong, J. Huang, *Energy Environ. Sci.* 2015, *8*, 1544.

[8] A. Barrows, A. Pearson, C. Kwak, A. Dunbar, A. Buckley, D. Lidzey, *Energy Environ. Sci.* 2014, *7*, 1.

[9] S. Das, B. Yang, G. Gu, P. C. Joshi, I. N. Ivanov, C. M. Rouleau, T. Aytug, D. B. Geohegan, K. Xiao, *ACS Photonics* 2015, *2*, 680.

[10] J. G. Tait, S. Manghooli, W. Qiu, L. Rakocevic, L. Kootstra, M. Jaysankar, C. A. Masse de la Huerta, U. W. Paetzold, R. Gehlhaar, D. Cheyns, P. Heremans, J. Poortmans, *J. Mater. Chem. A* 2016, *4*, 3792.

[11] H. Huang, J. Shi, L. Zhu, D. Li, Y. Luo, Q. Meng, *Nano Energy* 2016, *27*, 352.

[12] J. H. Heo, M. Lee, M. H. Jang, S. H. Im, *J. Mater. Chem. A* 2016, *4*, 17636.

[13] B. Conings, J. Drijkoningen, N. Gauquelin, A. Babayigit, J. D'Haen, L. D'Olieslaeger, A. Ethirajan, J. Verbeeck, J. Manca, E. Mosconi, F. De Angelis, H. G. Boyen, *Adv. Energy Mater.* 2015, *5*, 1500477.

[14] E. J. Juarez-Perez, L. K. Ono, M. Maeda, Y. Jiang, Z. Hawash, Y. Qi, *J. Mater. Chem. A* 2018, *6*, 9604.

[15] N. Pellet, P. Gao, G. Gregori, T. Y. Yang, M. K. Nazeeruddin, J. Maier, M. Grätzel, *Angew. Chemie - Int. Ed.* 2014, *53*, 3151.

[16] N. J. Jeon, J. H. Noh, W. S. Yang, Y. C. Kim, S. Ryu, J. Seo, S. Il Seok, *Nature* 2015, *517*, 476.

[17] M. Saliba, T. Matsui, J.-Y. Seo, K. Domanski, J.-P. Correa-Baena, N. Mohammad K., S. M. Zakeeruddin, W. Tress, A. Abate, A. Hagfeldt, M. Gratzel, *Energy Environ. Sci.* 2016, *9*, 1989.

[18] X. Li, D. Bi, C. Yi, J.-D. Décoppet, J. Luo, S. M. Zakeeruddin, A. Hagfeldt, M. Grätzel, *Science.* 2016, *353*, 58.

[19] M. Majumder, C. Rendall, M. Li, N. Behabtu, J. A. Eukel, R. H. Hauge, H. K. Schmidt, M. Pasquali, *Chem. Eng. Sci.* 2009, *65*, 2000.

[20] J. E. Bishop, T. J. Routledge, D. G. Lidzey, *J. Phys. Chem. Lett* 2018, *9*, 1977.

[21] Q. Jiang, L. Zhang, H. Wang, X. Yang, J. Meng, H. Liu, Z. Yin, J. Wu, X. Zhang, J. You, *Nat. Energy* 2016, *2*, 16177.

[22] S. Paek, P. Schouwink, E. N. Athanasopoulou, K. T. Cho, G. Grancini, Y. Lee, Y. Zhang, F. Stellacci, M. K. Nazeeruddin, P. Gao, *Chem. Mater.* 2017, *29*, 3490.

[23] N. J. Jeon, J. H. Noh, Y. C. Kim, W. S. Yang, S. Ryu, S. Il Seok, *Nat. Mater.* 2014, *13*, 897.

[24] W. S. Yang, J. H. Noh, N. J. Jeon, Y. C. Kim, S. Ryu, J. Seo, S. I. Seok, *Science.* 2015, *348*, 1234.

[25] Y. Zhou, O. S. Game, S. Pang, N. P. Padture, *J. Phys. Chem. Lett.* 2015, *6*, 4827.

[26] J. E. Bishop, D. K. Mohamad, M. Wong-Stringer, A. Smith, D. G. Lidzey, *Sci. Rep.* 2017, *7*, 7962.

[27] S. Uličná, B. Dou, D. H. Kim, K. Zhu, J. M. Walls, J. W. Bowers, M. F. A. M. van Hest, *ACS Appl. Energy Mater.* 2018, *1*, 1853.

[28] T. Jesper Jacobsson, J. P. Correa-Baena, M. Pazoki, M. Saliba, K. Schenk, M. Grätzel, A. Hagfeldt, *Energy Environ. Sci.* 2016, *9*, 1706.

[29] J. P. Correa Baena, L. Steier, W. Tress, M. Saliba, S. Neutzner, T. Matsui, F. Giordano, T. J. Jacobsson, A. R. Srimath Kandada, S. M. Zakeeruddin, A. Petrozza, A. Abate, M. K. Nazeeruddin, M. Grätzel, A. Hagfeldt, *Energy Environ. Sci.* 2015, *8*, 2928.

[30] S. Sanchez, X. Hua, N. Phung, U. Steiner, A. Abate, *Adv. Energy Mater.* 2018, *8*, 1702915.

[31] G. Abbas, H. Assender, M. Ibrahim, D. Martin Taylor, *J. Vac. Sci. Technol. B, Nanotechnol. Microelectron. Mater. Process. Meas. Phenom.* 2011, *29*, 052401.

Chapter 7

Fully Spray-Coated Triple-Cation Perovskite Solar Cells

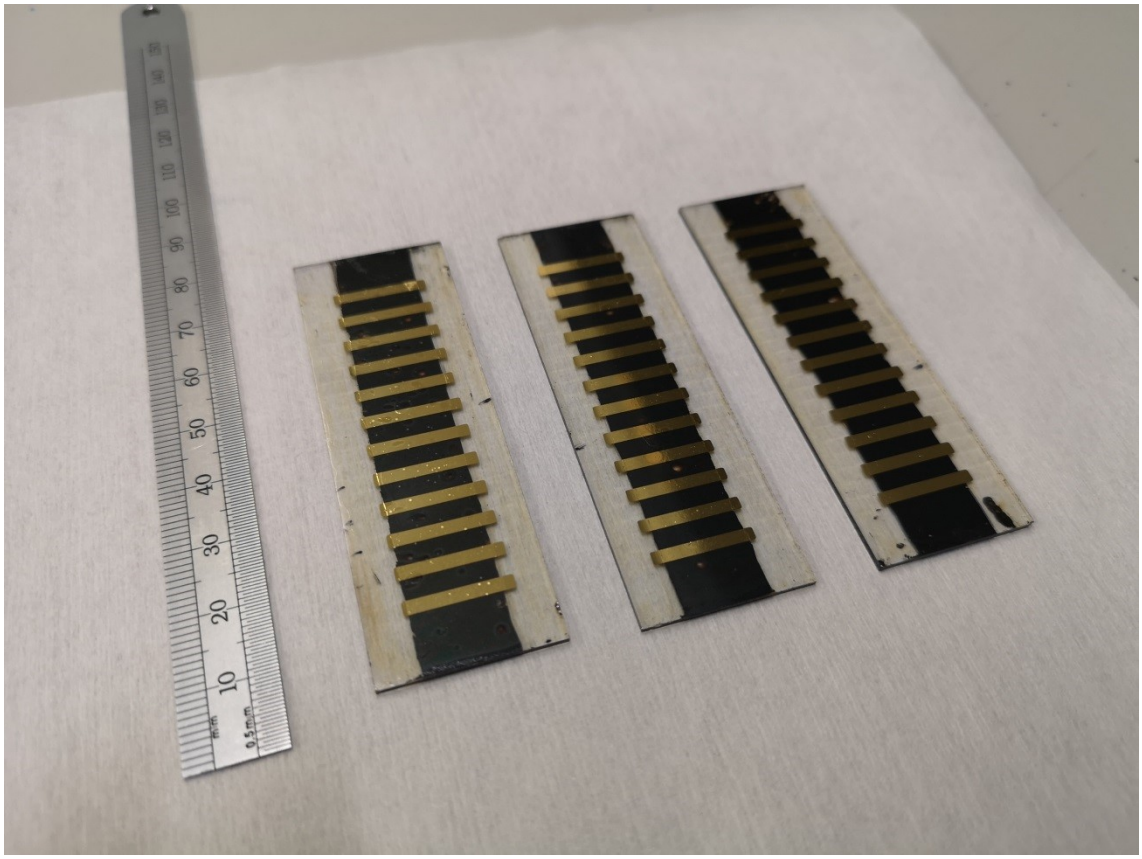

7.1: Publication Forward

The development of the vacuum assisted spray-deposition method allowed an improvement in the performance of sprayed perovskite devices to an average of 15% PCE. In this paper the work performed in Chapter 5 is revisited, where all solution processed layers were deposited by spray-coating, with the aim to increase the efficiency of the devices. Furthermore the process is scaled up from small-area substrates (15 mm x 20 mm) to larger-sized substrates (25 mm x 75 mm), whilst maintaining performance.

7.2: Publication Main Body

Fully Spray-Coated Triple-Cation Perovskite Solar Cells

James E. Bishop, Joel A. Smith, Thomas J. Routledge, David G. Lidzey*

Department of Physics & Astronomy, University of Sheffield, Hicks Building, Hounsfield Road, Sheffield, S3 7RH, U.K.

*Corresponding author, email d.g.lidzey@sheffield.ac.uk

Abstract

We employ ultrasonic spray-coating to sequentially deposit thin films of tin oxide, a triple-cation perovskite, and spiro-OMeTAD to fabricate efficient perovskite solar cells (PSCs). The use of spray-deposition allows us to rapidly coat 25 mm x 75 mm substrates which were each patterned into twelve devices with an active area of 15.4 mm^2. These devices had an average power conversion efficiency (PCE) of 12.2%, and a peak PCE of 15.1%. This compares favourably to the highest reported "fully-sprayed" devices which had a peak PCE of 10.2%. Furthermore by measuring ten 15.4 mm^2 devices on one substrate in parallel, we are able to achieve 11.9% PCE with an effective active area of 1.5 cm^2.

Introduction

Since the initial reports of perovskite solar cells (PSCs) in 2009 the power conversion efficiencies (PCEs) of such devices have risen from 3.8%[1] to 25.2%[2]. Perovskites have many properties which make them an attractive material for solar cell applications including efficient light absorption, tuneable band gap, high charge-carrier mobility, and high defect tolerance.[3–7] However it is the relative ease with which perovskite films can be formed from solution that has generated the greatest interest, as this potentially allows high volume manufacture of photovoltaic modules at low cost and low temperature. This could allow a dramatic reduction in the energy payback time of a commercial module to less than half a year.[8] In order for this to become a reality it is necessary demonstrate that perovskite solar cells can be fully fabricated using an industrially compatible coating technique.

Currently most perovskite device optimisation is performed using spin coating; a simple and reliable technique capable of producing highly uniform thin films. However spin coating is only suitable for coating small substrates on the order of square centimetres, not square meters.[9] Spin coating is also wasteful with the vast majority fluid thrown from the substrate during deposition. As a result several groups have turned their attention towards exploring scalable deposition techniques such as blade coating[10], slot-die coating[11], inkjet printing,[12] and spray-coating.[13]

The first spray-coated perovskite solar cells were fabricated in 2014 by Barrows *et al.* who employed an ultrasonic spray-coater to deposit a 3:1 mixture of methylammonium iodide and lead chloride.[13] Ultrasonic spray-coaters utilise piezoelectric transducers to shear the solution in question into a mist of micron sized droplets characterised by a smaller average size than those produced by a conventional air-brush device.[14] This, in principle, allows the deposition of more uniform coatings. Barrows *et al.* performed a simple single-pass deposition where the spray-head moves across the substrate at a defined speed coating it in solution. Subsequent heating of the film removed the solvent and formed the $CH_3NH_3PbI_{3-x}Cl_x$ perovskite capable of reaching 11% PCE when integrated into a device.[13]

Over the past few years a range of other papers have been published on spray-coated PSCs with a variety of new approaches used to improve film uniformity and device performance. These include: two-step deposition,[15] continuous soaking of the substrate,[16] anti-solvent bath treatment,[17] multiple spray-passes,[18] low vacuum treatment,[19] megasonic spray-coating,[20] and hot-air treatment.[21] As a result of this research effort many groups can reliably produce spray-coated PSCs with an average efficiency in the mid-teens with the best devices reaching a reverse scan PCE of 18.3%[16] and a stabilised PCE of 17%[19] according to a recent review.[9]

It is important to note that the vast majority of papers on spray-coated PSCs rely on spin-coating to deposit the electron and hole transport layers used within the device architecture.[13,15–23] Ideally one would like to utilise spray-coating to deposit all the solution processed layers with a PSC whilst maintaining good performance. Our group has published two examples of this. In 2016 Mohamad *et al.* published a method to fabricate inverted PSCs with an average PCE of 7.1% where the PEDOT:PSS, $CH_3NH_3PbI_{3-x}Cl_x$ perovskite, and PCBM had been deposited by spray-coating.[24] The following year Bishop *et al.* improved the average PCE to 9.2% by switching to normal architecture and spraying compact titania, mesoporous titania, $CH_3NH_3PbI_{3-x}Cl_x$ perovskite and spiro-OMeTAD.[25]

One recent study of note has reported on perovskite solar cells having an efficiency of 20% in which all solution processed layers (namely tin oxide, perovskite, and

Spiro-OMeTAD) were deposited via air-blading.[26] This arguably represents the state-of-the-art for scalable perovskite deposition methods. In this article we perform a similar study, building upon our previous work to spray-coat all solution processable layers within a device, with a low vacuum treatment step used to crystallise a "triple-cation" perovskite film which improves PV performance. Furthermore we scale up our fabrication process to larger area substrates, and demonstrate minimal loss in performance. This represents an important proof-of-concept that we believe could be transferable to an industrial manufacturing environment.

Results

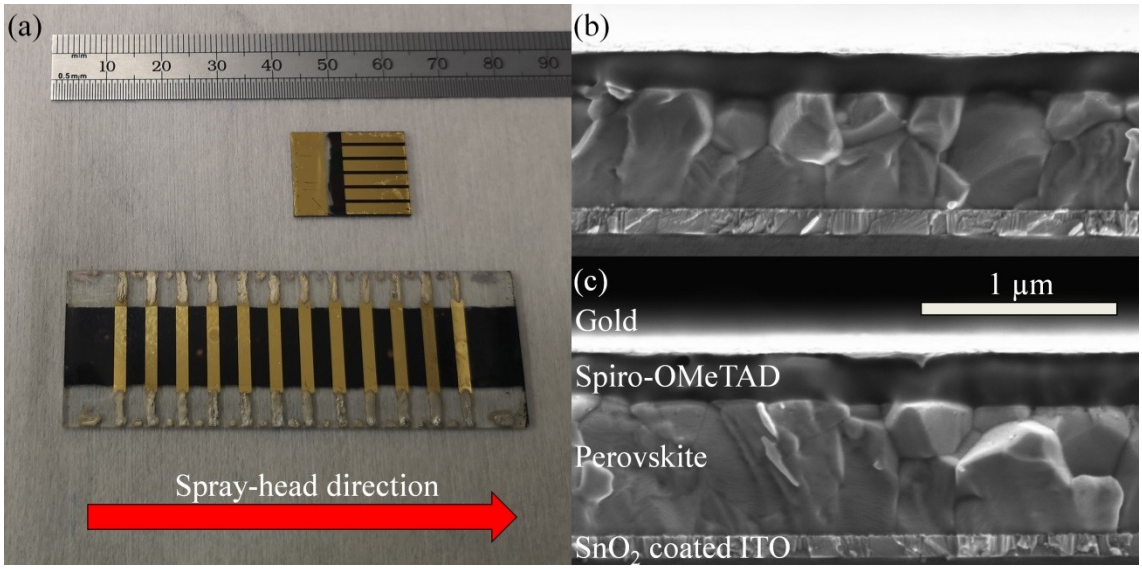

Figure 1: *Part (a) shows a photograph of small and large-area fully spray-coated perovskite solar cells. Parts (b) and (c) show a cross-sectional SEM image of complete devices incorporating a spray-cast perovskite layer. The device in part (b) utilises spin cast SnO_2 and Spiro-OMeTAD layers whereas the device in part (c) is fully spray-coated.*

Here, we report the use of a series of ultrasonic spray-coating processes to fabricate perovskite solar cells. The ultrasonic spray-coating technique utilises a tip vibrating at 10s of kHz to shear a fluid into a mist of micron sized droplets. To deposit the nanoparticle tin oxide (np-SnO_2) and Spiro-OMeTAD layers, we use a Prism Ultra-coat 300 system (Ultrasonic Systems Inc.) housed in low humidity air. To deposit the perovskite layer we utilise a Sonotek Exactacoat system fitted with

an “Impact” spray-head located in a nitrogen glovebox. Both spray-coaters are mounted on a motorised gantry that allows the spray-head to be scanned across a substrate in a controlled manner. All spray-coating described in this article are based on a simple “single pass” deposition process where the spray-head moves over the substrate in a straight line. This allows us to simulate a roll to roll industrial coating process in which a sheet is continuously fed through the system. By controlling head height, velocity and fluid flow rate, the thickness of the resultant layer can be controlled. By holding the substrate at an elevated temperature during deposition, we also control the wetting and drying of the solution.[14,27]

Figure 1a shows images of small and large-area spray-coated devices. Here the red arrow indicates the direction that the spray-head moved across the substrate. Small-area devices were fabricated on 15 x 20 mm ITO substrates (Ossila) which were patterned into six 2 x 2 mm pixels. These pixels were characterised though an illumination mask having a 2.6 mm^2 aperture. Large-area devices area fabricated on 25 x 75 mm ITO substrates (Ossila) which were patterned into twelve 10 x 2 mm pixels. These pixels were then characterised through an illumination mask having a 15.4 mm^2 aperture.

The devices fabricated were based on the following planar architecture, ITO/np-SnO_2/perovskite/spiro-OMeTAD/Au. Tin oxide layers were deposited from a commercially available nanoparticle dispersion[28] diluted in water, which we have both spin and spray-coated. After deposition the films were annealed for 30 minutes at 150 °C before exposure to a 15 minute UV ozone treatment. Films were then transferred to a nitrogen glovebox for deposition of the perovskite layer via VASP assisted spray-coating.[19] Here the perovskite precursor was a stoichiometric mixture with the composition $Cs_{0.05}FA_{0.81}MA_{0.14}PbI_{2.55}Br_{0.45}$, dissolved in a 4:1 mixture of DMF:DMSO. After the substrate was coated with the precursor ink it was loaded into a sealed box which was evacuated to a coarse vacuum (80 Pa) for 2.5 minutes. After this treatment, the substrate was removed from the vacuum and annealed at 120 °C for 20 minutes to fully crystallise the perovskite layer. Spiro-OMeTAD was either spin coated onto the substrate in a glovebox environment or spray-coated in air using a process similar to one we

have reported previously.[25] Here the spray-cast ink had a lower concentration and was dissolved in a 1:1 mixture of chloroform and chlorobenzene to enhance surface wetting and accelerate film drying. Finally thermal evaporation was used to deposit and pattern the gold top contact through a shadow mask. Further experimental details are given in the methods section.

We have fabricated a series of photovoltaic devices, in which the tin oxide and spiro-OMeTAD layers were either deposited via spin or spray coating in order to quantify the effect of the process route on device performance. Figure 1b shows an SEM cross-section of a spray-cast perovskite solar cell in which both transport layers were deposited via spin coating (device A). Figure 1c shows a similar cell in which all three layers were deposited via spray-coating (device D). Over these length scales it is apparent that there is no significant morphological difference between either of the devices, with the thickness of all of the layers being relatively uniform. A summary of the performance metrics of these devices are presented in Table 1, together with box plots in Figure 2.

Device	Device A	Device B	Device C	Device D	Device E
Area (mm^2)	2.6	2.6	2.6	2.6	15.4
np-SnO_2	Spin	Spray	Spin	Spray	Spray
Perovskite	Spray	Spray	Spray	Spray	Spray
Spiro-OMeTAD	Spin	Spin	Spray	Spray	Spray
PCE (%)	**17.4** (14.4±3.4)	**16.2** (13.4±2.5)	**15.8** (13.5±2.5)	**13.7** (12.0±1.6)	**15.1** (12.2±2.8)
J_{SC}(mA/cm^2)	**21.2** (20.4±0.7)	**21.8** (19.9±1.4)	**20.3** (18.4±2.6)	**20.0** (17.9±2.3)	**21.3** (19.9±1.5)
V_{oc} (V)	**1.08** (1.01±0.13)	**1.05** (1.01±0.04)	**1.08** (1.05±0.02)	**1.01** (1.01±0.01)	**1.09** (1.02±0.15)
FF (%)	**76** (68±11)	**71** (66±8)	**72** (69±4)	**68** (66±3)	**65** (59±8)
Failed Devices	0/16	3/16	0/16	1/16	6/48

***Table 1**: A summary of PSC performance metrics extracted from the reverse scan together with the deposition technique used to fabricate each layer. Data shown using a bold font are the values determined from the most efficient device with the average and standard deviation presented in parenthesis.*

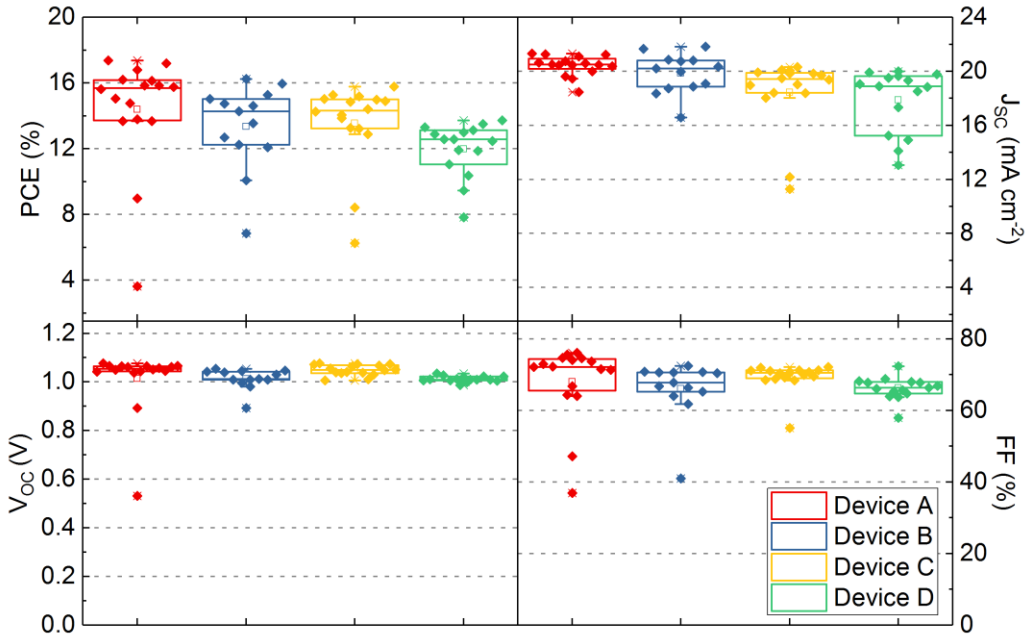

Figure 2: *Box plots showing reverse scan PSC performance recorded from small-area (2.6 mm²) devices A-D (see Table 1 for a description of device labels).*

We find that there is a reduction in efficiency as more layers within a device are deposited via spray-coating. Device A was spin coated with the exception of the VASP treated perovskite layer and had a peak PCE of 17.4% with an average of 14.4±3.4%. This is consistent with our previously reported findings and indicates that the process is repeatable.[19] Importantly we find that compared to our previous report[19]the vacuum exposure time can be shortened from 5 minutes to 2.5 minutes without any loss in PV performance.

We find that if the tin oxide nanoparticles are spray-cast (device B) a slight reduction in average PCE to 13.4±2.5% is observed caused as a result of cumulative losses in all other metrics. On spray-coating the spiro-OMeTAD (device C) we find a similar reduction in average PCE to 13.5±2.5% however this seems to originate from a reduction in device J_{SC}. We speculate that this may result from a slight increase in thickness of the spray-cast spiro-OMeTAD layer relative to that of the spin-cast layer. When all three layers were spray-cast (device D) we observe a reduction in average PCE to 12.0±1.6%.

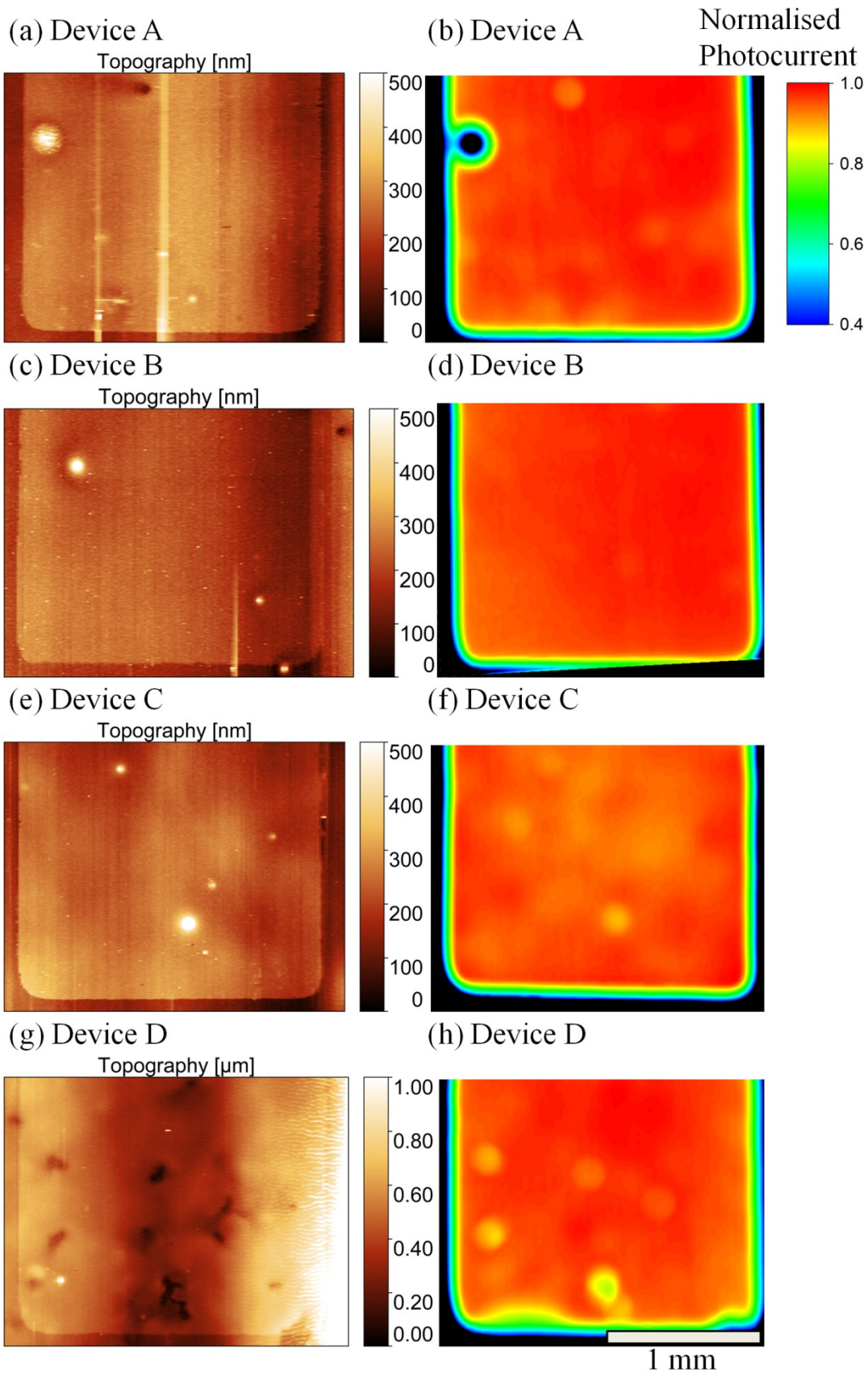

***Figure 3**: Topographical (left hand column) and laser-beam-induced current mapping images (right hand column) of spray-coated perovskite solar cells.*

In order to understand the origin of the reduction in efficiency associated with spray-coating, we have performed profilometry and laser-beam-induced-current mapping (LBIC) on a series of typical devices fabricated by spin and spray-coating. Here, a Dektak profilometer was used to create a topographical image of the device surface. The same device was then scanned by a 25 μm laser spot whilst recording the photocurrent, allowing the photovoltaic response of device to be mapped. The results of these measurements are shown in Figure 3.

It is immediately apparent that the photocurrent uniformity decreases as more layers are sprayed (see Figure S1); a finding that accounts for the observed reduction in PCE. LBIC maps of devices A and B appear very similar with little variation across the surface of the device. There is a 170 μm diameter region of reduced photocurrent in device A (a "cold spot") which is correlated with a defect in the topographical map. We have observed such defects before[19,25] and suspect that they result from an aggregates in the perovskite layer. Interestingly a similar but smaller defect is observed in the topographical image device B, however no such reduction in the photocurrent is detected. This may indicate that such devices can tolerate defects of a certain size, or any reduction in photocurrent may be beyond the resolution of our LBIC measurements.

On spray-coating the spiro-OMeTAD layer we observe a change in the film topography, with clear thickness fluctuations occurring over length-scales of hundreds of microns in both devices C and D. Many of these can be observed in the corresponding LBIC images and likely explain the observed reduction in PCE in devices incorporating spray-cast spiro-OMeTAD. Device D also seems to contain several defects in its centre which we suspect are small voids in the spiro-OMeTAD layer. Spiro-OMeTAD has a tendency to dewett although by controlling the substrate temperature this effect can be supressed. We also observe voids in the perovskite layer (see Figure S2) which can result in significant reduction in device performance. Indeed if such voids are large enough, they can cause in a large drop in both V_{OC} and FF (see Figure S3) and can result in a failed device. We have classified devices with less than 1% efficiency as "failed devices" and the number we observe is reported in Table 1. Note, the performance metrics of these devices have been omitted from our statistical analysis.

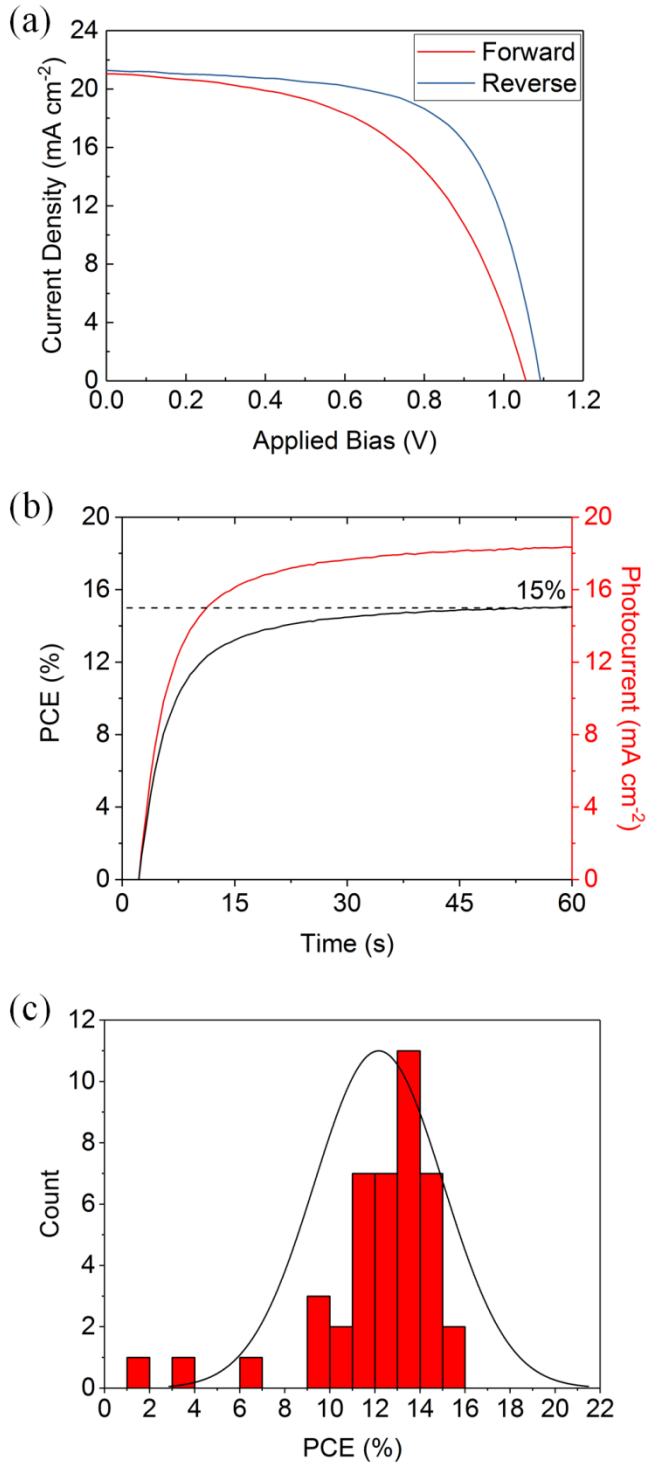

***Figure 4**: (a) Current-voltage characteristics for the champion fully spray-cast perovskite solar cell with an active area of 15.4 mm² and a reverse-scan efficiency of 15.1%. (b) Output power of the champion device held at a fixed voltage close to the maximum power point (0.82 V) over 60 s, indicating a stabilised PCE of 15%. (c) A histogram of reverse-scan PCE data from 42 fully spray-cast devices having an active area of 15.4 mm².*

We have used our spray-coating process to perform a limited scaling up of device area. Here, four large-area substrates were coated that comprised a total of 48 15.4 mm^2 devices. Upon testing we observe no reduction in PCE between small and large-area fully sprayed PSCs (devices D and E respectively). Furthermore we obtained a champion device having a reverse scan PCE of 15.1% (see Figure 4a). Figure 4b shows a stabilised power measurement from this champion cell of 15%. We find that 6 of the 48 devices were classed as failed devices; however the remaining functioning devices achieved an average reverse scan PCE of 12.2±2.8%. A histogram of the PCE of these devices is shown in Figure 4c, with the other three average performance metrics shown in Table 1 along with those of the champion device. By connecting 10 of the 12 devices on one substrate in parallel, we were able to reach a reverse scan PCE of 11.9% over an effective active area of 1.54 cm^2 (see Figure S4). This is a significantly greater efficiency than our previous work in which we reported a 6.6% efficient fully spray-cast device having an active area of 1.008 cm^2.[25] This result suggests a good degree of uniformity over all three spray-cast layers across the coating area (18.8 cm^2).

Discussion

To conclude we have developed a process to fabricate perovskite solar cells in which all three solution processed layers are deposited via spray-coating. This allows us to coat relatively large areas (25 mm x 75 mm) at speed forming twelve 15.4 mm^2 devices per substrate. These devices had a champion PCE of 15.1% and an average of 12.2±2.8%. By simultaneously connecting 10 of such devices in parallel, we create a device having a PCE of 11.9% with an active-area of 1.54 cm^2. We have characterised the quality of spray-cast devices using a combination of surface profilometry and laser-beam-induced current mapping, and finding that device performance is reduced by the presence of aggregates and voids within the perovskite, as well as thickness fluctuations in the spiro-OMeTAD. In order to improve device reproducibility and performance, the origin of these defects will need to be determined. Nonetheless, this work demonstrates a fast scalable way to fabricate efficient perovskite solar cells.

Methods

Device Fabrication. FaI (Ossila), MaBr (Dyesol), $PbBr_2$ (TCI), PbI_2 (TCI), and CsI (Sigma) were weighed out into a vial to form the triple cation perovskite $Cs_{0.05}FA_{0.81}MA_{0.14}PbI_{2.55}Br_{0.45}$. For each 1 mL of precursor solution, the following quantities of powder were used: FaI (167 mg), PbI_2 (467 mg), MaBr (19 mg), $PbBr_2$ (68 mg) and CsI (16 mg). The powders were then dissolved in a mixture of DMF and DMSO at a ratio of 4:1 (800 µL and 200 µL) to form the perovskite precursor solution.

Small-area devices were fabricated on 15 x 20 mm unpatterned ITO substrates (20 Ω/sq, Ossila S111) which were etched with 4M HCL and zinc powder. Large-area devices were fabricated on pre-patterned 25 x 75 mm ITO substrates (Ossila S241). Prior to deposition, substrates were cleaned via sonication in Hellmanex, deionised water and IPA. The substrates were then treated with a UV ozone plasma cleaner for 15 minutes.

For spin coating, tin oxide nanoparticle solution (SnO_2 colloidal solution 15% wt water) was diluted at 1:5.5 in DI water and spin coated under ambient conditions onto the ITO at 3000 rpm. The tin oxide was then heated for 30 minutes at 150 °C and UV ozone treated for a further 15 minutes.

For spray-coating tin oxide nanoparticle solution was diluted 1:70 in DI water and spray-cast in air using a Prism Ultra-coat 300 system. The spray-head was programmed to move across the substrate at a speed of 100 mms^{-1} at a height of 30 mm coating a substrate held at 20 °C in a single pass. The flow rate was determined via the nitrogen feed into the fluid reservoir which was set to a pressure of 20 mbar. After 30 s the film had dried and the tin oxide was heated for 30 minutes at 150 °C and then UV ozone treated for a further 15 minutes.

The SnO_2 coated substrates were transferred to a glovebox for spray deposition using a Sonotek Exactacoat system mounted with an “Impact” spray-head. The perovskite precursor was delivered at 1 $mLmin^{-1}$ to the surface through a tip driven at 2 W using a N_2 shaping gas at 3 Psi. The head was held 10 cm above the substrate which was mounted on a hotplate held at 40°C. During deposition, the head moved in a line scan over the substrate at 80 mms^{-1}. The width of the spray

pattern is 3 cm allowing the coating of both the small and large-area substrates in a single pass.

After deposition, the substrate was left for 30 s to allow an even wet film to form. The substrate was then transferred to the glovebox antechamber for vacuum exposure. The film was left for 2.5 minutes in the vacuum chamber whilst it pumped down to approximately 80 Pa. After 2.5 minutes, the vacuum chamber was rapidly re-filled with nitrogen. The film was then returned to the glovebox and placed on a hotplate at 120 °C for 20 minutes.

Perovskite films were transferred to a second glovebox for spin coating spiro-OMeTAD. 2,2',7,7'-Tetrakis[N,N-di(4-methoxyphenyl)amino]-9,9'-spirobifluorene (Spiro-OMeTAD) powder was dissolved in CB at a concentration of 86.6 $mgmL^{-1}$. This was then doped with lithium bis(trifluoromethanesulfonyl)imide (LITFSI Sigma), 4-tert-butyl-pyridine (TBP Sigma), and tris(2-(1H-pyrazol-1-yl)-4-tert-butylpyridine)cobalt(II) di[hexafluorophosphate] (FK209 Co(II) PF6 Dyesol). The quantity of dopants used in 1 mL of spiro-OMeTAD solution was as follows: 20 µL of LiTFSI (500 mgmL-1 in acetonitrile), 36 µL TBP, and 11 µL of FK209 (300 $mgmL^{-1}$ in acetonitrile). The solution was finally filtered before being spin coated at 4000 rpm.

For spray-coating the doped and filtered spiro-OMeTAD solution was diluted to 43.3 $mgmL^{-1}$ by adding equal volume of chloroform to the solutions initial volume (thus creating a 1:1 mixture of CB and CF). This solution was then spray-coated in air using the Prism Ultra-coat 300 system. The spray-head was programmed to move across the substrate at a speed of 150 mms^{-1} and at a height of 60 mm in a single pass over the substrate, which was held at 30 °C. The flow rate was set by the nitrogen pressure which was 20 mbar.

After spiro-OMeTAD deposition, films were left overnight in dry air to oxidise. The substrates were then patterned using a 100 nm of gold film that was deposited at a pressure of $\approx 10^{-6}$ Pa in an Edwards bell jar evaporator. Small-area devices were mounted in a mask that defined six 2 x 2 mm cells per substrate. Large-area devices were patterned through a mask defining twelve 10 x 2 mm cells per substrate.

Spray Parameter	np-SnO_2	Perovskite	Spiro-OMeTAD
Spray-coater	Prism Ultracoat 300 Ambient Lab Conditions	Sonotek Exactacoat, Impact Spray-Head, Glovebox	Prism Ultracoat 300 Ambient Lab Conditions
Substrate Temp (°C)	20	40	30
Head Height (mm)	30	100	60
Head Velocity (mm s^{-1})	100	80	150
Flow Rate (mL min^{-1})	N/A	1	N/A
Fluid Pressure (mbar)	20	N/A	20

***Table 2**: Summary of spray parameters used to fabricate perovskite solar cells.*

Current-Voltage Measurements. Devices were tested under AM 1.5 illumination using a Newport Solar Simulator. The light intensity was calibrated to 1000 Wm^{-2} using a silicon reference cell (Newport). Devices were swept from -0.2 V to 1.2 V and back to -0.2 V at a scan rate of 0.4 Vs^{-1} using a Keithley 237 source measure unit. Small-area and large-area devices were tested through illumination masks having an area of 2.6 mm^2 and 15.4 mm^2 respectively. By measuring several devices over the large-area substrates the performance of larger active areas could be established. For such measurements a slower scan rate of 0.1 Vs^{-1} was employed. Stabilised measurements were taken by holding the device at a point close to the maximum power point for 60 s whilst reading the current.

External Quantum Efficiency. EQE measurements were performed using a custom setup. Light from a 100 W tungsten halogen lamp was passed through a monochromator (Spectral Products DK240 1/4m) and then focussed onto the device. Photocurrent was measured using an Xtralien X100 source measure unit (Ossila) and compared to that produced by a silicon reference photodiode (Newport) with a known spectral response to calculate the EQE.

Surface Profilometry and Laser-Beam-Induced Current Mapping. A Bruker Dektak:XT was utilised to generate surface topography maps of perovskite solar cells (12.5 μm tip radius, 3 mg stylus force) over an area of 2 x 3 mm. Each image was generated from a series of 200 line scans separated by 15 μm, where each line scan covered a lateral distance of 2000 μm with a resolution of 0.333 μm per point.

The laser-beam-induced-current (LBIC) mapping system comprised of a mechanically chopped laser that was passed through a spatial filter before being focused to a spot size of about 25 μm onto a device via a 10x objective. The sample

was mounted on a computer controlled XY-stage, and moved in a sawtooth pattern in steps of 25 μm. A 1.2 mW, 632 nm laser (Thor labs, HRS015B) was used to generate a photocurrent that was measured using a lock-in amplifier (Stanford Research Systems, SR830) and referenced to the chopped laser.

Scanning Electron Microscopy. Cross-sectional scanning electron microscopy (SEM) images were collected using a Carl Zeiss modified Raith Nanofabrication SEM at 1.5 kV accelerating voltage at ~2 mm working distance. Signal was gathered using an "InLens" detector with rapid acquisition on image areas to minimise sample beam damage.

Acknowledgements

This work was funded by the UK Engineering and Physical Sciences Research Council (EPSRC) via grants EP/M025020/1 "High resolution mapping of performance and degradation mechanisms in printable photovoltaic devices", and EP/M014797/1 "Improved Understanding, Development and Optimization of Perovskite-based Solar Cells". We also thank the EPSRC for PhD studentships via the University of Sheffield DTG account (J.E.B.) and from the Centre for Doctoral Training in New and Sustainable PV, EP/L01551X/1 (J.A.S.)

Author Contributions

J.E.B. fabricated and tested the devices in addition to performing LBIC and EQE measurements. J.A.S. assisted in the spray deposition of SnO_2 nanoparticles and performed SEM. J.E.B. and T.J.R. performed Dektak surface profilometry and analysis. D.G.L. contributed to the design of experiments and analysis of the data. All authors contributed to the writing of the manuscript.

Conflict of Interest

D.G.L. is co-director of the company Ossila Ltd that retail materials and equipment for perovskite photovoltaic device research and development.

7.3: Supplementary Information

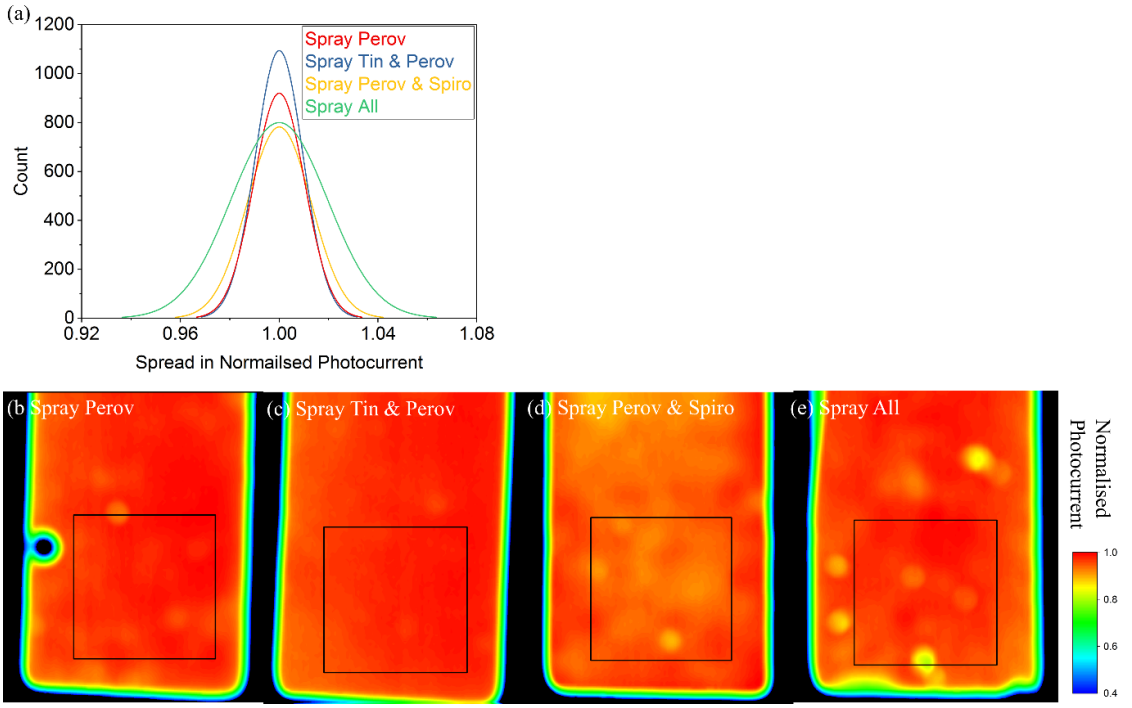

***Figure S1**: (a) Histograms showing the spread in normalised photocurrent around the mean value for various sprayed PSCs taken from LBIC measurements. (b) through (e) show the LBIC images where the black boxes denote the areas sampled to create the histograms shown in (a). Here it is clear that as more layers are sprayed the spread in photocurrent values also increases due to loss in uniformity from spray-coating.*

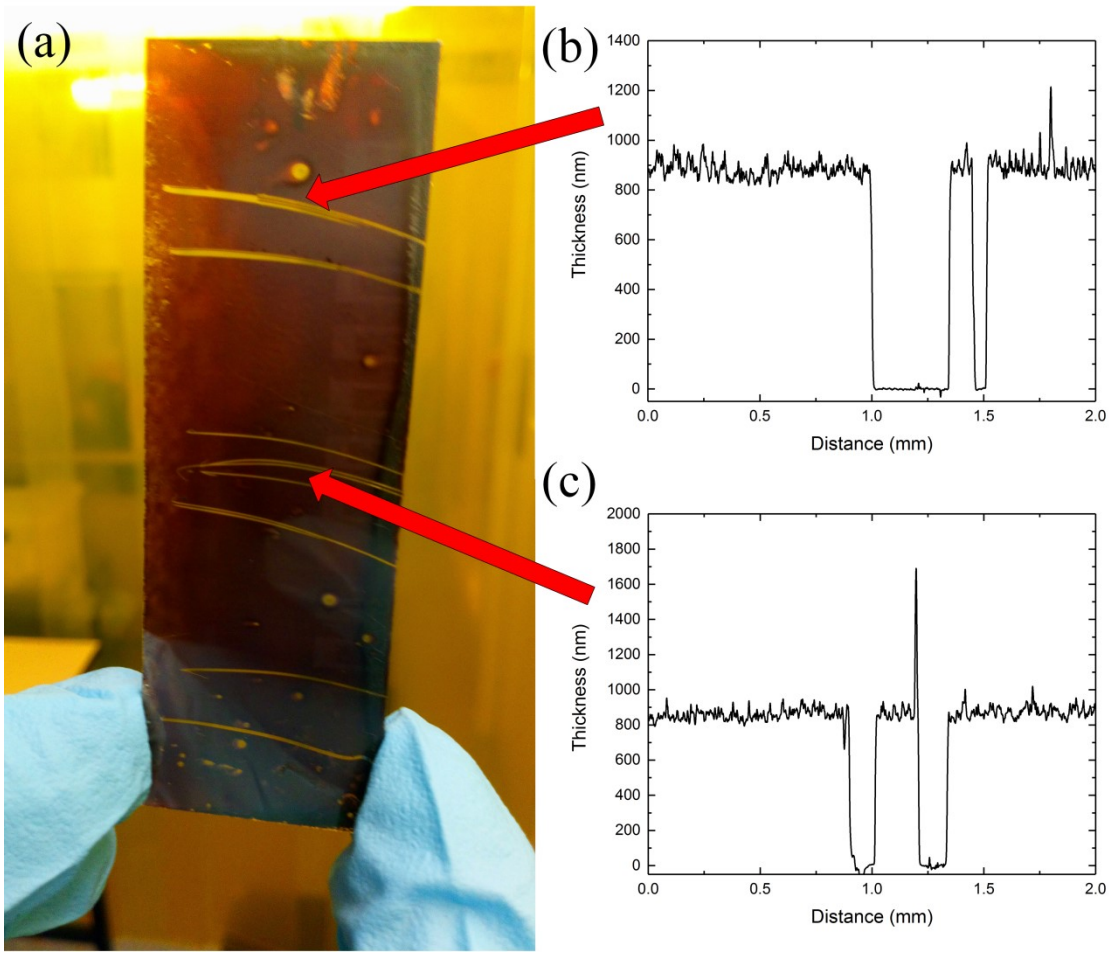

***Figure S2**: (a) Photograph of a spray-coated perovskite film. Here the presence of several circular voids in the film is apparent as well as scratches made in the film for thickness measurements. (b) and (c) show Dektak line scans used to estimate the thickness of the layer (850±100 nm).*

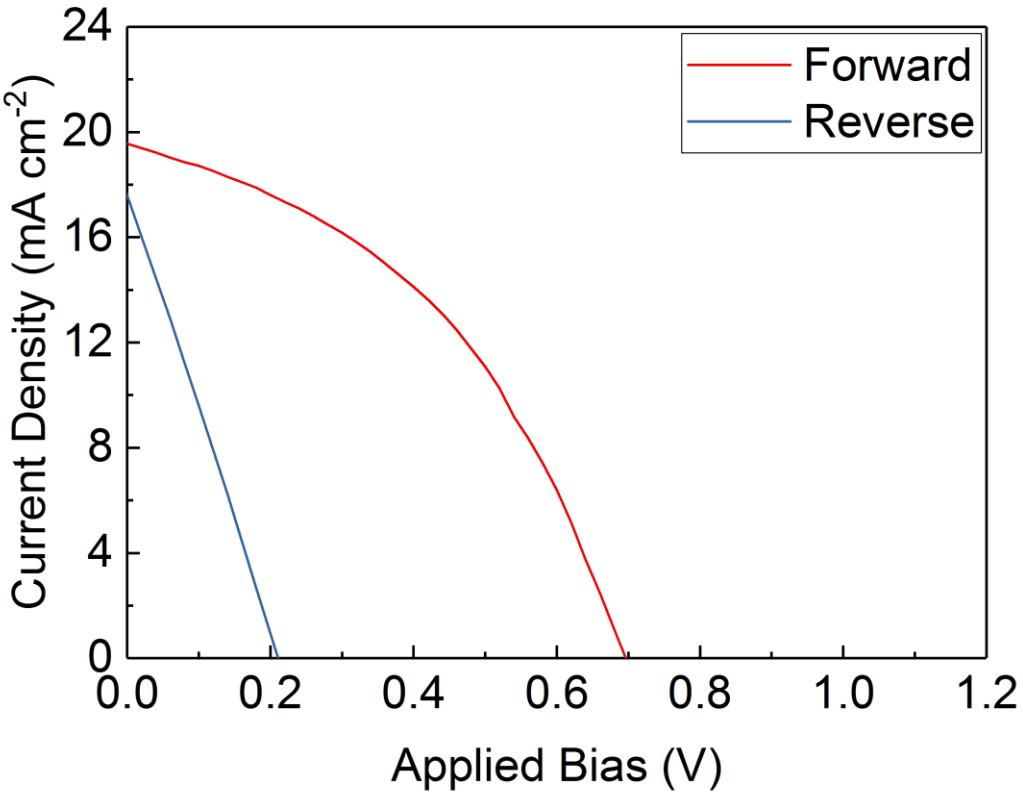

***Figure S3**: Example of a "failed" device where the reverse scan PCE is less than 1%.*

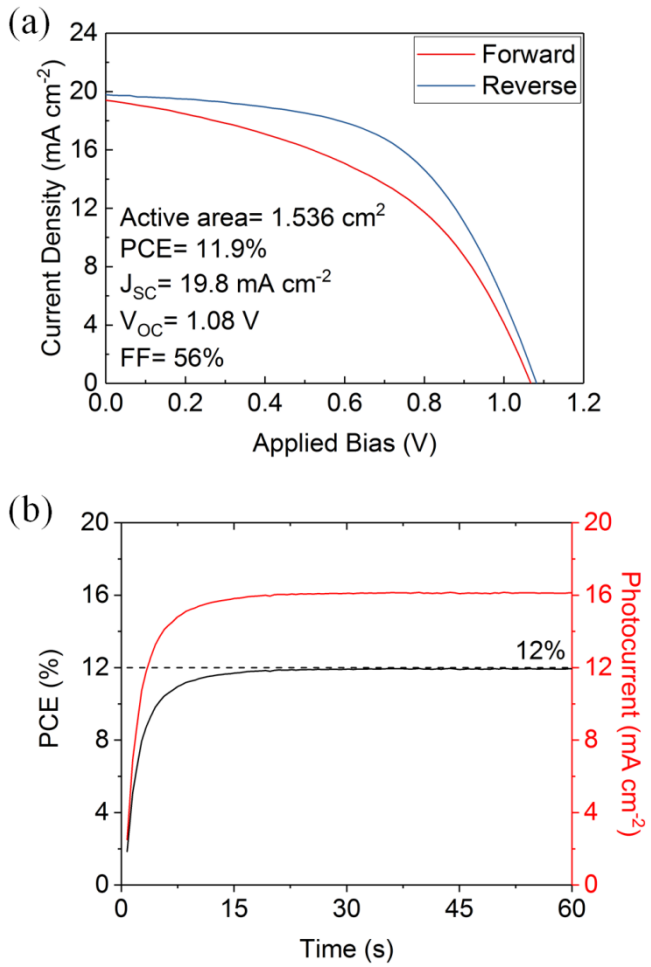

***Figure S4**: (a) Current-voltage characteristics for ten 15.4 mm² devices on one large-area substrate connected in parallel, creating a device with an effective active-area of 1.54 cm². (b) Stabilised power output for the same ten parallel connected devices held at 0.74 V for 60 s. The effective power output for this device is 18.3 mW.*

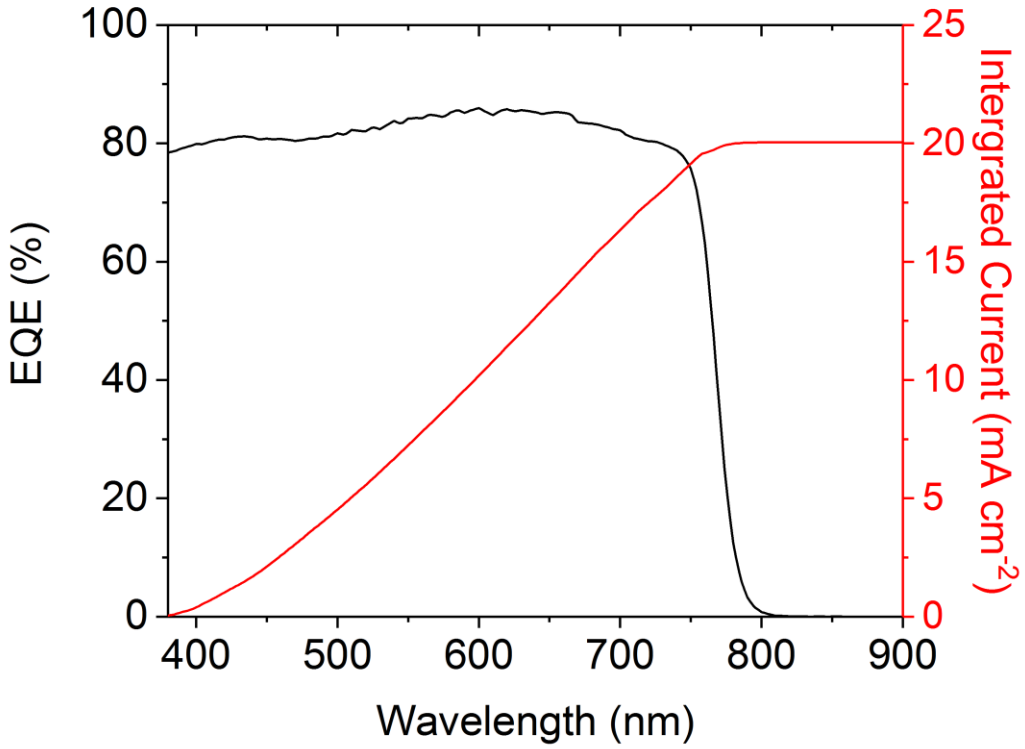

***Figure S5**: EQE spectrum for a fully spray-coated perovskite solar cell showing an integrated J_{SC} of 20 mAcm^{-2}. Note due to technical limitations with our EQE setup we are unable to measure spectral response below 380 nm thus the integrated J_{SC} is likely to be a slight underestimate for this particular device.*

7.4: Further Context

The fabrication of large-area devices in this Chapter represents the culmination of work in this thesis. However the process is not without its flaws. The voids in the perovskite layer are of particular concern as they can cause devices to fail completely. Future work will include understanding why such defects occur and preventing them from forming.

7.5: References

[1] A. Kojima, K. Teshima, Y. Shirai, T. Miyasaka, *J. Am. Chem. Soc.* **2009**, *131*, 6050.

[2] NREL. Best Research-Cell Efficiencies. https://www.nrel.gov/pv/assets/pdfs/best-research-cell-efficiencies.20190923.pdf (accessed October 2019)

[3] N. G. Park, *Mater. Today* **2015**, *18*, 65.

[4] V. D'Innocenzo, G. Grancini, M. J. P. Alcocer, A. R. S. Kandada, S. D. Stranks, M. M. Lee, G. Lanzani, H. J. Snaith, A. Petrozza, *Nat. Commun.* **2014**, *5*, 3586.

[5] G. E. Eperon, S. D. Stranks, C. Menelaou, M. B. Johnston, L. M. Herz, H. J. Snaith, *Energy Environ. Sci.* **2014**, *7*, 982.

[6] S. D. Stranks, G. E. Eperon, G. Grancini, C. Menelaou, M. J. P. Alcocer, T. Leijtens, L. M. Herz, A. Petrozza, H. J. Snaith, *Science.* **2013**, *342*, 341.

[7] K. X. Steirer, P. Schulz, G. Teeter, V. Stevanovic, M. Yang, K. Zhu, J. J. Berry, *ACS Energy Lett.* **2016**, *1*, 360.

[8] J. Gong, S. B. Darling, F. You, *Energy Environ. Sci.* **2015**, *8*, 1953.

[9] I. A. Howard, T. Abzieher, I. M. Hossain, H. Eggers, F. Schackmar, S. Ternes, B. S. Richards, U. Lemmer, U. W. Paetzold, *Adv. Mater.* **2019**, *1806702*, 1806702.

[10] W.-Q. Wu, Q. Wang, Y. Fang, Y. Shao, S. Tang, Y. Deng, H. Lu, Y. Liu, T. Li, Z. Yang, A. Gruverman, J. Huang, *Nat. Commun.* **2018**, *9*, 1625.

[11] J. B. Whitaker, D. H. Kim, B. W. Larson, F. Zhang, J. J. Berry, M. F. A. M. Van Hest, K. Zhu, *Sustain. Energy Fuels* **2018**, *2*, 2442.

[12] P. Li, C. Liang, B. Bao, Y. Li, X. Hu, Y. Wang, Y. Zhang, F. Li, G. Shao, Y. Song, *Nano Energy* **2018**, *46*, 203.

[13] A. Barrows, A. Pearson, C. Kwak, A. Dunbar, A. Buckley, D. Lidzey, *Energy Environ. Sci.* **2014**, *7*, 2945.

[14] J. E. Bishop, T. J. Routledge, D. G. Lidzey, *J. Phys. Chem. Lett* **2018**, *9*, 1977.

[15] H. Huang, J. Shi, L. Zhu, D. Li, Y. Luo, Q. Meng, *Nano Energy* **2016**, *27*, 352.

[16] J. H. Heo, M. Lee, M. H. Jang, S. H. Im, *J. Mater. Chem. A* **2016**, *4*, 17636.

[17] S. Uličná, B. Dou, D. H. Kim, K. Zhu, J. M. Walls, J. W. Bowers, M. F. A. M. van Hest, *ACS Appl. Energy Mater.* **2018**, *1*, 1853.

[18] L.-H. Chou, X.-F. Wang, I. Osaka, C.-G. Wu, C.-L. Liu, *ACS Appl. Mater. Interfaces* **2018**, *10*, 38042.

[19] J. E. Bishop, J. A. Smith, C. Greenland, V. Kumar, N. Vaenas, O. S. Game, T. J. Routledge, M. Wong-Stringer, C. Rodenburg, D. G. Lidzey, *ACS Appl. Mater. Interfaces* **2018**, *10*, 39428.

[20] M. Park, W. Cho, G. Lee, S. C. Hong, M. cheol Kim, J. Yoon, N. Ahn, M. Choi, *Small* **2019**, *15*, 1804005.

[21] J. Su, H. Cai, X. Ye, X. Zhou, J. Yang, D. Wang, J. Ni, J. Li, J. Zhang, *ACS Appl. Mater. Interfaces* **2019**, *11*, 10689.

[22] S. Das, B. Yang, G. Gu, P. C. Joshi, I. N. Ivanov, C. M. Rouleau, T. Aytug, D. B. Geohegan, K. Xiao, *ACS Photonics* **2015**, *2*, 680.

[23] J. G. Tait, S. Manghooli, W. Qiu, L. Rakocevic, L. Kootstra, M. Jaysankar, C. A. Masse de la Huerta, U. W. Paetzold, R. Gehlhaar, D. Cheyns, P. Heremans, J. Poortmans, *J. Mater. Chem. A* **2016**, *4*, 3792.

[24] D. K. Mohamad, J. Griffin, C. Bracher, A. T. Barrows, D. G. Lidzey, *Adv. Energy Mater.* **2016**, *6*, 1600994.

[25] J. E. Bishop, D. K. Mohamad, M. Wong-Stringer, A. Smith, D. G. Lidzey, *Sci. Rep.* **2017**, *7*, 7962.

[26] J. Ding, Q. Han, Q.-Q. Ge, D.-J. Xue, J.-Y. Ma, B.-Y. Zhao, Y.-X. Chen, J. Liu, D. B. Mitzi, J.-S. Hu, *Joule* **2019**, *3*, 402.

[27] G. J. Gittens, *J. Colloid Interface Sci.* **1969**, *30*, 406.

[28] Q. Jiang, L. Zhang, H. Wang, X. Yang, J. Meng, H. Liu, Z. Yin, J. Wu, X. Zhang, J. You, *Nat. Energy* **2016**, *2*, 16177.

Chapter 8

Conclusions

In Chapter 5 a method to spray-coat all four solution processed layers within a normal architecture PSC was developed. Spray-pyrolysis of TiO_2 to form hole blocking layers is a common technique and this was combined with ultrasonic spray deposition of mesoporous-TiO_2, $CH_3NH_3PbI_{(3-x)}Cl_x$ perovskite, and spiro-OMeTAD. Notably this was the first report on spray-coated spiro-OMeTAD in the literature, although this layer proved challenging to deposit due to its tendency to dewett. This was attributed to the ionic dopants required to enhance spiro-OMeTAD conductivity. The performance of the sprayed devices compared well to spin-cast references, although over time it became apparent that the quality of the perovskite layer was lacking when compared to the high-performance devices in the literature.

In Chapter 6 a new method to spray-coat the perovskite layer was developed allowed the formation of smoother and more uniform films. A switch was made to caesium containing "triple-cation" perovskite which was capable of higher performance and greater operational stability. A method to coat uniform precursor films using a new glovebox mounted spray-coater was developed, although creating smooth perovskite films comparable to those produced by spin coating proved difficult. The breakthrough came with use of a vacuum post treatment step which replicated the effect of an antisolvent quench used when spin coating the same material. This allowed for more controlled nucleation of the perovskite resulting in a smoother and more uniform thin film. Using these films led to a dramatic increase in performance allowing devices to match the best reports on spray-coated devices in the literature.

In Chapter 7 the learning from Chapters 5 and 6 was combined to enhance the efficiency of our "fully-sprayed" devices. Here, the TiO_2 was substituted for nanoparticle SnO_2 which simplified the deposition process as well as reducing the maximum annealing temperature. By spraying all three layers devices were scaled

up to larger substrates and active-areas without any loss in performance. The best PCE for a fully-sprayed device was increased from 10.2% to 15.1%.

Whilst this thesis represents a clear improvement on the efficiency of spray-coated PSCs many challenges remain. Although the VASP technique has led to a significant improvement in perovskite uniformity defects are still present. Most problematically, voids that seem to occur during film formation have yet to be eliminated and can in some cases cause devices to fail. These defects must be eliminated to enable large area devices to be fabricated reliably. In addition, the process used is still reliant on thermal evaporation of a gold top contact. Finally, whilst the PCE of spray-cast devices has increased significantly, they still lag behind the record for a spin coated PSC of 25.2%. This is problem faced by all scalable printing methods but it is a problem that must be overcome in order for industry to seriously consider PSCs as a viable technology.

One avenue that has not been properly explored is spray-coating PSCs onto non-planar or curved surfaces. This is a challenge spray-coating is uniquely qualified for as unlike many other scalable techniques (e.g. slot-die coating), the spray-head does not need to be close to the surface being coated. This could allow integration of PV onto surfaces where conventional panels cannot be mounted allowing more of the built environment to be utilised for energy harvesting. For example a PSC could be deposited onto a strong, lightweight material such as carbon fibre to power a lightweight autonomous drone.